

**Jet-medium interactions via direct photon-hadron correlation measurements
in Au+Au collisions at $\sqrt{s_{NN}} = 200$ GeV**

A Dissertation presented

by

Huijun Ge

to

The Graduate School

in Partial Fulfillment of the

Requirements

for the Degree of

Doctor of Philosophy

in

Physics

Stony Brook University

August 2017

ProQuest Number: 10622398

All rights reserved

INFORMATION TO ALL USERS

The quality of this reproduction is dependent upon the quality of the copy submitted.

In the unlikely event that the author did not send a complete manuscript and there are missing pages, these will be noted. Also, if material had to be removed, a note will indicate the deletion.



ProQuest 10622398

Published by ProQuest LLC (2017). Copyright of the Dissertation is held by the Author.

All rights reserved.

This work is protected against unauthorized copying under Title 17, United States Code
Microform Edition © ProQuest LLC.

ProQuest LLC.
789 East Eisenhower Parkway
P.O. Box 1346
Ann Arbor, MI 48106 – 1346

Copyright by
Huijun Ge
2017

Stony Brook University

The Graduate School

Huijun Ge

We, the dissertation committee for the above candidate for the
Doctor of Philosophy degree, hereby recommend
acceptance of this dissertation

Barbara Jacak - Dissertation Advisor

Professor, Department of Physics, University of California, Berkeley

Axel Drees - Dissertation Advisor

Professor, Department of Physics and Astronomy

John Hobbs - Chairperson of Defense

Professor, Department of Physics and Astronomy

Dmitri Kharzeev

Professor, Department of Physics and Astronomy

Stefan Bathe

Professor, Department of Natural Sciences, Baruch College, City University of New York

This dissertation is accepted by the Graduate School

Charles Taber

Dean of the Graduate School

Abstract of the Dissertation

**Jet-medium interactions via direct photon-hadron correlation measurements
in Au+Au collisions at $\sqrt{s_{NN}} = 200$ GeV**

by

Huijun Ge

Doctor of Philosophy

in

Physics

Stony Brook University

2017

Hot and dense matter called quark-gluon plasma (QGP) has been created in high energy heavy ion collisions in the relativistic heavy ion collider (RHIC). Jets are observed to be suppressed in heavy ion collisions compared to those in p+p baseline - a phenomenon known as "jet quenching". This arises from the fact that partons from initial hard scatterings lose energy when traversing through and interacting with the medium. Extensive effort has been made in understanding the energy loss mechanism.

Direct photon-hadron correlations are a golden channel to study parton energy loss in QGP. Photons do not interact strongly with the medium and exit unperturbed. High momentum photons are produced back-to-back with partons at leading order in the initial hard scatterings via predominantly QCD Compton scatterings. Their measured momentum will approximately balance those of the opposing partons before any medium modification. Consequently, using high-momentum direct photons as triggers is a most direct measure of the initial parton energy. Compared to di-hadron correlations or reconstructed jets, this measurement has no bias toward the medium surface.

The modification of the fragmentation function for the away-side jet can be measured by comparing the integrated $\gamma_{dir} - h$ yields in heavy ion collisions

to those in p+p. We analyzed Au+Au data taken by PHENIX in 2011 and combined with the results from 2007 and 2010. The per-trigger-yield of associated hadrons in Au+Au collisions is measured and we observe a suppression compared to p+p for higher momentum fraction (z_T) hadrons. A yield enhancement is found at low z_T (high ξ). Comparison with theory shows that jet induced medium response is likely to be responsible for the enhanced production of these lower momentum particles.

To Mom and Dad

Contents

1	Introduction	1
1.1	The Standard Model	3
1.2	Quantum chromodynamics	3
1.3	QCD calculations	5
1.4	Quark Gluon Plasma: A New State of Matter	7
1.4.1	Collision geometry and the Glauber Model	11
1.4.2	Collectivity and Elliptic Flow	12
1.5	Direct photons	14
1.6	Jet Quenching and Parton Energy Loss	16
1.6.1	Two particle correlations	19
1.6.2	Probing Jet Substructure	22
1.6.3	Recent Theory Work on Energy Loss	28
1.7	γ_{dir} -h correlations	35
1.8	Statement of Purpose	36
2	Experimental Setup	40
2.1	RHIC	41
2.2	PHENIX	42
2.2.1	Triggering, data acquisition and event reconstruction .	45
2.2.2	Event characterization	45
2.2.3	Tracking Detectors	49
2.2.4	Particle Identification Detectors	55
2.2.5	Silicon Vertex Tracker	65
3	Analysis Details	67
3.1	Data and event selection	69
3.2	Run quality assurance	69
3.3	Two particle correlations	71

3.3.1	Two-Source Model	71
3.4	Particle Selection	81
3.4.1	EMCal Cluster Selection	81
3.4.2	π^0 identification	87
3.4.3	Track selection	89
3.5	Charged hadron efficiency correction	95
3.6	π^0 efficiency correction	97
3.7	Statistical Subtraction Method	97
3.7.1	R_γ	99
3.7.2	Decay Mapping	100
3.7.3	π^0 cutoff correction	103
3.8	Fill-time method for ξ binned results	105
3.9	Effect of increased conversions in Run-11 on results or R_γ . . .	106
4	Uncertainties	111
4.1	Uncertainty Propagation	113
4.2	R_γ and Statistical Subtraction	114
4.3	Decay Mapping	115
4.4	Uncertainties on Jet Function Extraction	117
4.5	Propagation of uncertainties	119
4.5.1	Combining Trigger p_T bins	119
4.5.2	Combine Datasets and Centralities	119
5	Results and Discussion	121
5.1	The p+p baseline	123
5.2	Previous Au+Au $\gamma_{dir} - h$ results	126
5.3	Run11 Au+Au $\gamma_{dir} - h$ results	130
5.4	Combined Au+Au $\gamma_{dir} - h$ results	134
5.4.1	$\Delta\phi$ distributions	134
5.4.2	Integrated away-side yields	136
5.4.3	Away-side I_{AA}	137
5.4.4	A Note on the d+Au Result	146
6	Conclusions and Outlook	152
6.1	Summary of the Au+Au Result	152
6.2	Relation to Other Experimental Results	153
6.3	Future Prospects	154

List of Figures

1.1	Feynman diagrams of vertices in QCD [82]	4
1.2	Measurements of α_s as a function of the energy scale Q from PDG2016 [1]	5
1.3	Examples of parton distribution functions [1]	8
1.4	Fragmentation functions in terms of ξ distributions measured in $e^+ + e^-$ and DIS processes [1].	8
1.5	A simple schematic of the QCD phase diagram: a phase transition happens at the crossover region near which normal nuclear matter changes to quark-gluon plasma, a dense and hot medium in which partons are deconfined.	9
1.6	Pressure, energy density and entropy density normalized by $1/T^4$, $1/T^4$ and $1/T^3$. This is the Lattice QCD calculations from Hot QCD collaboration [36]. Solid lines represent the predictions from the hadron resonance gas (HRG) model. T_c is marked as the vertical yellow band. The horizontal line denotes the ideal gas limit with the value of $95\pi^2/60$	10
1.7	A schematic of the QGP evolution with time.[82]	11
1.8	Collision geometry	12
1.9	Multiplicity distribution demonstrating the relationship between impact parameter, N_{part} , collision centrality [59].	13
1.10	Cartoons illustrating elliptic flow, event plane and momentum anisotropy.	15
1.11	v_2 as a function of transverse momentum and energy, scaled by the number of constituent quarks, for various particle species.	15
1.12	Direct photon production at leading order (LO).	16
1.13	Direct photon production at next-leading-order (NLO).	17

1.14	Direct photon spectra in 0-20%, 20-40% and 40-80% Pb+Pb collisions measured by ALICE. The yields are compared to NLO pQCD predictions for direct photon yield in pp collisions scaled by N_{coll}	17
1.15	(a): R_{AA} measured in PHENIX for direct photons, identified hadrons and non-photonic electrons in 0-10% most central Au+Au collisions at $\sqrt{s} = 200$ GeV. (b): R_{AA} for identified π^\pm, K^\pm , (anti)protons and D mesons from ALICE and charged hadrons, direct photons, W and Z bosons from CMS.	19
1.16	Upper panel: Dijet asymmetry A_J distributions in various centrality bins in Pb+Pb collisions at $\sqrt{s_{NN}} = 2.76$ TeV (solid dots). For comparison, p+p points from collisions at $\sqrt{s} = 7$ TeV are shown in open circles. Lower panel: Dijet azimuthal angle $\Delta\phi$ distributions for data and simulation, as a function of centrality.	20
1.17	A cartoon illustrating two-particle correlations.	21
1.18	Dihadron measurement in p+p, d+Au and Au+Au collisions.	21
1.19	A schematic of the evolution of a full jet in a QGP [6].	22
1.20	Ratio of fragmentation functions for central to peripheral Pb+Pb events, as a function of z, measured using anti- k_T jets of cone size of R = 0.4.	24
1.21	Fragmentation functions measured by CMS, for Pb+Pb compared to p+p collisions at $\sqrt{s} = 2.76$ TeV, with the Pb+Pb/p+p ratio in the lower panels, as a function of ξ , for various centrality selections.	25
1.22	Differential jet shapes in Pb+Pb and p+p collisions in various centrality selections. The ratios have been normalized to unity.	25
1.23	Jet mass distributions for anti- k_T jets with R = 0.4 for 0-10% most central Pb+Pb collisions, compared to JEWEL, PYTHIA and Q-PYTHIA calculations.	26
1.24	Ratios of splitting function in Pb+Pb and p+p collisions for jets with $160 < p_{T,jet} < 180$ GeV/c in different centrality bins.	27
1.25	Left: Energy loss for a light quark produced in 0-5% most central collisions at RHIC. Right: Energy loss for a bottom quark in 0-7.5% most central collisions at LHC.	29
1.26	Energy distributions for leading partons and medium partons at different times for a gluon with initial energy E = 100 GeV propagating in the medium with temperature T = 0.4 GeV.	31

1.27	Energy density distribution showing for simulated medium response from a gluon of initial energy $E_0 = 100$ GeV and propagate along z and r directions after 4 and 8 fm/c, inside a quark-gluon plasma with temperature of $T = 0.4$ GeV.	33
1.28	Angular distributions of medium partons with different energies, induced by a gluon with an initial energy $E = 100$ GeV, propagating at different times of propagation, inside a QGP with temperature of $T = 0.4$ GeV.	38
1.29	Ratios of jet fragmentation function in Pb+Pb to p+p collisions for anti- k_T jets with cone size $R = 0.3$, measured by CMS as a function of ξ , shown on the left and the ATLAS data as a function of p_T^{track} , shown on the right. Comparisons with JEWEL simulations are shown in green lines representing no recoils included and blue lines denoting with recoils.	39
2.1	A schematic drawing of RHIC facility, demonstrating the process of colliding Au ion beams. The Au ions are accelerated and stripped step by step from Tandem Van de Graaff, Booster and then AGS before injection into the RHIC ring in counter-rotating directions and collide head-on at different crossings.	42
2.2	PHENIX coordinate system [45]. z axis is the beam direction along which reside the muon arms as well as event characterization detectors. The x-y plane is the azimuthal plane where the central spectrometers sit.	43
2.3	PHENIX detectors layout and positioning in 2011. A beam view showing mostly the central arm detectors is presented in (a). The forward detectors including the muon arms are displayed in the side view (b).	44
2.4	A picture showing (a) dimensions of a single BBC Cherenkov counter composed of a quartz radiator and PMT readout. (b) one BBC module: made of 64 BBC elements integrated in a honeycomb fashion.	47
2.5	Position of the zero degree counters [55].	48
2.6	Centrality determination by correlating the neutron energy detected in the ZDC as a function of number of charged hits measured in the BBC. Slicing collected events into centrality bins using the clock method (left) and the BBC-only method (right) [62].	49

2.7	The drift chamber design: (a) A schematic display of one DC frame and its geometric characteristics and corresponding size measurement. (b) Left: a side view showing the stacked wire planes inside one drift chamber cell and inside the anode plane. Right: A top view demonstrating the orientation of X U V wire planes. [63]	51
2.8	An example timing distribution of the drift chamber hits in the west arm. Calibration parameters t_0 and t_f are determined by fitting the edges of the distribution [80].	51
2.9	PC1, PC2 and PC3 positioning in PHENIX with a few sectors of PC2 and PC3 removed for viewing clarity [85].	52
2.10	Left: a 9×9 pixel pattern that connects to one readout channel. Right: A demonstration of pad and pixel layout. Blue, red and green represent for 3 different 9×9 pixel arrangement. A cell is defined as the shaded box with dashed lines, which contains three pixels that are connected to different but neighboring readout pads [79].	53
2.11	An illustration of the DC track reconstruction, including the combinatorial Hough Transform parameters ϕ and α [66]. The method is discussed in the text.	54
2.12	Illustration of the initial set of track parameters (p_T , ϕ , θ , z_v) and the measured set of parameters (α , β , ϕ_{DC} , z_{pad}). $\phi_{DC} = \phi_v + \Phi$, which is measured at the DC reference radius R_{DC} . z_{pad} is the z position measured in PC1.	56
2.13	An electromagnetic shower induced inside a block of absorber material.	57
2.14	A cutaway view of one PbSc module.	58
2.15	A cutaway view of one PbGl supermodule.	59
2.16	χ^2 distributions for electromagnetic showers produced by electrons (solid line) and pions (dashed line) of 2 GeV/c in the PbSc calorimeter.	60
2.17	2γ invariant mass distributions showing sample fits for π^0 peaks in one EMCal PbGl sector (left) and in one tower of a PbSc sector (right).	62

2.18	Generated EMCAL maps for Run-12 U+U and Cu+Au datasets: (a) a warnmap for each sector. The red areas represent hot/dead towers while the green represents neighboring and edge towers. (b) final uncalibrated tower map. (c) 2-D tower-by-tower coefficients map, in which the blank spots represent the uncalibrated towers. For each map, 4 sectors on the left represent PbSc sectors in the west arm; 4 sectors on the right are in the east arm (with sector 4,5 being PbGl and 6,7 being PbSc). x and y axes label the tower positions along the z and y directions according to the PHENIX coordinates.	63
2.19	Before (black) and after (red) calibration: (a) π^0 peak position tower-by-tower distributions; (b) mean vs p_T	63
2.20	An interior view of one of the RICH detector [56]	65
2.21	A schematic view of the VTX detector layout in PHENIX. Surrounding the beam pipe at radial distances of 2.6 cm and 5.1 cm are the two inner layers B0 and B1, each consisting of 10 and 20 pixel ladders, respectively. Further away from the center at about 11.8 cm and 16.7 cm are the two outer layers B2 and B3, each includes 16 and 24 stripixel ladders.	66
3.1	Examples of run-by-run $\Delta\phi$ distribution ratios and fits for foreground inclusive cluster and reconstructed track pairs.	70
3.2	χ^2 of a flat line fit to the ratios of the foreground pair distributions to the combined distributions, as a function of run number	70
3.3	A cartoon illustrating event mixing in a simplified way [82]. The solid line denotes a pair from the same event which is not allowed, while the dashed line connects a mixed event pair. Events are characterized according to the collision centralities and z-vertex positions. Particles of type B from each event is stored in the corresponding designation in the mixing pool. Pairing is carried out by associate trigger particles of type A with particle B that shares the same global event characteristics.	73
3.4	A typical $\Delta\phi$ distribution of uncorrelated pairs measured using event mixing.	74

3.5	An illustration of two-source model: how background shapes and separation from signals in two-particle angular correlation measurements. Red peaks stand for jet signals and the yellow regions are background. (a) represents a typical p+p collision that background is flat and the level is relatively low. (b) is for Au+Au collisions, in which the background is much higher and has harmonic shape known as flow. Both ZYAM and ABS method can be applied for background subtraction in these two cases. For the Au+Au analysis discussed in this dissertation, ABS method is used to determine background level.	77
3.6	ξ calculation [69]	79
3.7	N_{part} (a) and N_{coll} (b) distributions from the Glauber calculations.	80
3.8	Top: number of inclusive photon as a function of N_{coll} and N_{part} ; Bottom: number of hadrons as a function of N_{coll} and N_{part} ; All distributions are fitted with an arctangent (black) and a saturated exponential (red) functional forms.	81
3.9	ξ as a function of centrality.	82
3.10	Tower hit distributions for cluster energy less than 5 GeV (left) and greater than 5 GeV (right). Red dashed lines represent the 5σ cut that assigned the towers that lie beyond as hot towers.	84
3.11	Hits in each EMCAL sector for cluster energy less than 5 GeV, before the hot tower map is applied. Four sectors on the left represent EMCAL sectors in west arm (PbSc); Four sectors on the right are in the east arm (with sector 4,5 being PbGl and 6,7 being PbSc). x and y axes label the tower positions along the z and y directions according to the PHENIX coordinates. .	85
3.12	Hits in each EMCAL sector for cluster energy greater than 5 GeV, before the hot tower map is applied.	85
3.13	Hits in each EMCAL sector for cluster energy less than 5 GeV, after the hot tower map is applied.	86
3.14	Hits in each EMCAL sector for cluster energy greater than 5 GeV, after the hot tower map is applied.	86
3.15	Reconstructed π^0 mass peak positions (left) and widths as a function of run number.	87

3.16	Distance between cluster position and track projection in the EMCAL in the same event, for 4 centralities. The dotted dashed line specifies the cut value 8 cm.	88
3.17	2γ invariant mass distribution showing reconstructed π^0 peaks, for different trigger p_T ranges.	89
3.18	An example of $emcd\phi$ distribution for east arm for $0.25 < p_T < 4.25$ GeV/c positively charged tracks within $-75 < zed < -60$ cm. A double Gaussian fit of the distribution (black) in each bin decomposes into signal (blue) and background (red).	92
3.19	Mean (top) and sigma (bottom) of $emcd\phi$ as a function of p_T in different zed bin for positively charged tracks. Column (a) - PbGl sectors; Column (b) - PbSc.	93
3.20	Mean (top) and sigma (bottom) of $emcsd\phi$ as a function of p_T in different zed bin for positively charged tracks. Column (a) - PbGl sectors; Column (b) - PbSc.	94
3.21	Ratios of hadron yields with different PC3/EMCal matching cut, as a function of hadron p_T . A 2σ cut is used in this analysis.	94
3.22	Single hadron acceptance \times efficiency determined for p/γ , π^\pm , K^\pm (a) and particle type averaged (b) from simulation.	97
3.23	π^0 efficiency for 0-20% (black), 20-40% (red) and 40-60% (blue) centrality classes.	98
3.24	R_γ input used in this analysis. These are determined from a separate analysis and rebinned for the current analysis. The error bars showing here include both statistical and systematic uncertainties.	99
3.25	A "shark fin": probability function for a π^0 to decay into a photon of $5 < p_T < 7$ GeV/c, as a function of the parent π^0 p_T . The black solid line represents the analytical calculation, as compared to the red curve demonstrating the simulation result.	101
3.26	Probability for a π^0 to decay into a $7 < p_T^\gamma < 9$ GeV/c photon for a few different z_{EMC} bins.	102
3.27	Distortions observed in foreground (black) and background (red) $\Delta\phi$ distributions for lower associate hadron p_T bins, before modifying fill-time weights, compared to the left (no weighting case).	107

3.28	Left: inclusive photon-hadron foreground (black) and background (red) in no weighting case; Right: weighting case. This is an example for trigger 5-7 GeV/c and associate partner in 0.5-1 GeV/c.	107
3.29	An example demonstrating background subtracted inclusive photon-hadron yields using weighting method (red) and no weighting (black) and their ratio.	108
3.30	A demonstration of v_2 implementation in fill-time weighting procedure. The red points stand for the measured 0-20% hadron v_2 in each p_T bin, the weights are taken from the interpolation between these points.	108
3.31	The upper two panels show ratios of inclusive photon-hadron to π^0 -hadron jet functions in Run-11 (Red) and Run-10 (Black) and the double ratio (Run-10/Run-11). The jet functions presented here are the per-trigger yield (PTY). The lower two panels show ratios of inclusive photon-hadron to decay photon-hadron jet functions in Run-11 (Red) and Run-10 (Black) and the double ratio (Run-10/Run-11). The double ratios on the right are compared to 1 and a χ^2 test is done. This example is for 5-7 GeV triggers correlated with charged hadrons within 0.5-1 GeV/c bin in 0-20% centrality bin.	109
3.32	χ^2 test results on conversion effect: ratios of inclusive γ -h over π^0 -h or decay γ -h between run11 and run10 are consistent with 1.	110
4.1	π^0 invariant mass peaks and signal-to-background ratios for 0-20% centrality class. The four panels corresponds to four π^0 p_T trigger bins.	116
4.2	π^0 invariant mass peaks and signal-to-background ratios for 20-40% centrality class	117
4.3	$\pi^0 - h$ per trigger yield on the away-side as a function of π^0 p_T for hadron p_T within 1-2, 2-3 and 3-5 GeV/c. A linear fit is used in the method to determine the π^0 combinatorial background [80].	118

5.1	Azimuthal angular distributions of $\pi^0 - h$, direct $\gamma - h$ and isolated $\gamma - h$ in p+p collisions for different trigger and associated hadron p_T bins with momentum ranges of $5 < p_T^{trig} < 15 \text{ GeV/c}$ and $1 < p_T^h < 7 \text{ GeV/c}$ [76].	126
5.2	x_E distributions of the integrated full away-side yields triggered by π^0 's and isolated direct photons in transverse momentum ranges of 5-7, 7-9, 9-12 and 12-15 GeV/c. Fits to the data using an exponential functional form and a modified Hagedorn function are shown in the dashed line and the solid line, respectively [76].	127
5.3	ξ distributions for the integrated full away-side yields triggered by isolated direct photons in transverse momentum ranges of 5-7, 7-9, 9-12 and 12-15 GeV/c. TASSO data in e^+e^- collisions at $\sqrt{s} = 14$ and 44 GeV are included for comparison [76].	127
5.4	Per-trigger hadron yield with transverse momentum of $3 < p_T^h < 5 \text{ GeV/c}$ triggered by inclusive photons, decay photons and direct photons in $5 < p_T^\gamma < 7 \text{ GeV/c}$ bin in p+p (top panel) and central Au+Au collisions (bottom panel) [75].	128
5.5	z_T distributions of $\gamma_{dir} - h$ per-trigger yield measured in p+p (left) and central Au+Au (right) collisions for trigger p_T bins of 5-7, 7-9, 9-12 and 12-15 GeV/c [75].	129
5.6	Top panel: ξ distribution of $\gamma_{dir} - h$ per-trigger yield for 0-40% most central Au+Au (black circles) collisions and p+p (blue squares) collisions. Bottom panel: I_{AA} as a function of ξ , compared to theory predictions from BW-MLLA (red dashed line) for $E_{jet} = 7 \text{ GeV}$ in medium in 0-10% most central Au+Au collisions and YaJEM (blue dot-dashed line) calculated for 0-40% centrality bin and trigger p_T of 9-12 GeV/c.	131
5.7	γ_{inc} -h (green), γ_{dec} -h (red) and γ_{dir} -h (black) correlations for trigger photon 5-7 GeV/c, in Au+Au 0-40% most central collisions from Run-11. γ_{dir} -h in p+p collisions (blue) is included for comparison.	133
5.8	γ_{inc} -h (green), γ_{dec} -h (red) and γ_{dir} -h (black) correlations for trigger photon 7-9 GeV/c, in Au+Au 0-40% most central collisions from Run-11. γ_{dir} -h in p+p collisions (blue) is included for comparison.	134

5.9	γ_{dir} -h (black) correlations for trigger photon 5-9 GeV/c, in Au+Au 0-40% most central collisions from Run-11, compared to γ_{dir} -h in p+p collisions (blue). Panels (b), (d), and (f) are scaled up by a factor of 2.	135
5.10	γ_{inc} -h, γ_{dec} -h and γ_{dir} -h for trigger photon 5-7 GeV/c, using combined statistics from Run-7, Run-10 and Run-11.	136
5.11	γ_{inc} -h, γ_{dec} -h and γ_{dir} -h for trigger photon 7-9 GeV/c, using combined statistics from Run-7, Run-10 and Run-11.	137
5.12	γ_{inc} -h, γ_{dec} -h and γ_{dir} -h for combined trigger photon p_T 5-9 GeV/c, using combined statistics from Run-7, Run-10 and Run-11.	138
5.13	γ_{inc} -h, γ_{dec} -h and γ_{dir} -h for combined trigger photon p_T 5-7 GeV/c, using combined statistics from Run-7, Run-10 and Run-11.	139
5.14	γ_{inc} -h, γ_{dec} -h and γ_{dir} -h for combined trigger photon p_T 7-9 GeV/c, using combined statistics from Run-7, Run-10 and Run-11.	140
5.15	γ_{inc} -h, γ_{dec} -h and γ_{dir} -h for combined trigger photon p_T 5-9 GeV/c, using combined statistics from Run-7, Run-10 and Run-11.	141
5.16	Integrated away-side ($ \Delta\phi - \pi < \pi/2$) γ_{dir} -h per-trigger yields as a function of ξ for trigger photons of $5 < p_T^\gamma < 9$ GeV/c (black), as compared to p+p (blue). The shaded box on each Au+Au point is the systematic uncertainty of the measurement.	142
5.17	Integrated away-side ($ \Delta\phi - \pi < \pi/2$) γ_{dir} -h per-trigger yields vs ξ for trigger photon with p_T of 5-7 GeV/c (top panel), 7-9 GeV/c (middle panel) and 9-12 GeV/c (bottom panel). The p+p results are shown in blue circles and are shifted to the left with respect to the Au+Au data points (black) along the ξ axis for clear viewing.	143
5.18	I_{AA} as a function of ξ for trigger p_T^γ of 5-9 GeV/c.	144
5.19	I_{AA} vs ξ for trigger p_T^γ of 5-7 GeV/c (black), 7-9 GeV/c (red) and 9-12 GeV/c (Green).	144

5.20	Energy density distributions demonstrating a $\gamma - jet$ event in the medium. The directions are labeled for both the trigger photon and the propagating jet in the transverse plane at $\tau = 2$ fm/c (top) and 4.8 fm/c (bottom). The two panels on the right show the scenario when not including hydrodynamic background	145
5.21	Top: the jet fragmentation function in p+p and 0-12% central Au+Au collisions. Bottom: I_{AA} as a function of z for CoLBT-hydro calculations with and without including jet-induced medium excitations, compared to STAR $\gamma_{dir} - h$ measurement.	146
5.22	I_{AA} for trigger photon p_T of 5-7, 7-9 and 9-12 GeV/c, as a function of ξ , compared with theoretical model calculations.	147
5.23	I_{AA} as a function of ξ for trigger p_T^γ of 5-7 GeV/c (top panel), 7-9 GeV/c (middle panel) and 9-12 GeV/c (bottom panel). Three away-side integration ranges are chosen to calculate the per-trigger yield and the corresponding I_{AA} : $ \Delta\phi - \pi < \pi/2$ (black circles), $ \Delta\phi - \pi < \pi/3$ (blue squares) and $ \Delta\phi - \pi < \pi/6$ (red triangles). In each panel a flat line of I_{AA} is shown to guide the eye. The enhancement with respect to the p+p baseline measurement is most dominant in 5-7 GeV/c trigger bin and for the case of full away-side integration range.	148
5.24	Ratios of I_{AA} as a function of trigger p_T , for three different away-side integration ranges.	149
5.25	Top panel: Integrated away-side $\gamma_{dir} - h$ per-trigger yields of Au+Au (black dots), d+Au (purple crosses) and p+p (blue squares), as a function of ξ . p+p and d+Au points have been shifted to the left for clear viewing, as indicated in the legend. Bottom panel: I_{AA} (black dots) and I_{dA} (purple crosses).	150
5.26	Integrated away-side ($\Delta\phi > \pi/2$) $\gamma_{dir} - h$ per-trigger yields for triggers with p_T from 5 - 7 GeV/c (top left), 7 - 9 GeV/c (top middle), and 9 - 12 GeV/c (top right). In black are the yields for the d+Au analysis, in blue are the p+p reference. The full ZYAM + R_γ + method systematic uncertainties are shown as the shaded bands around each point. The I_{dA} resulting from the ratio of the d+Au yields to the p+p yields is shown in the bottom set of Figures for each trigger p_T range.	151

6.1 Gaussian widths and D_{AA} of the away-side peaks and momentum difference between Au+Au and p+p.	155
--	-----

List of Tables

1.1	A summary of the four fundamental forces in nature and each corresponding theory that governs with the listed interaction range, relative strength and force carriers.	3
3.1	Triggers and charged hadrons v_2 values for 0-20% centrality bin	82
3.2	Triggers and charged hadrons v_2 values for 20-40% centrality bin	83
3.3	Cutoff correction for π^0	104
4.1	R_γ values and statistical and systematic uncertainties	114
4.2	Direct photon-hadron per-trigger yield in ξ bins for 0-40% central Au+Au for trigger photon p_T within 5-9 GeV/c. In addition to the total statistical and systematic uncertainties, a breakdown into individual sources that contribute to the total systematic error and the corresponding values are listed.	120

Acknowledgement

The completion of this work would not have been possible without the help of many people. I would like to express my deepest gratitude to my advisor, Barbara Jacak, who has provided continuous support, expertise and wisdom when guiding me in research. Thanks to her advice and encouragement, I also gain more confidence in public speaking. I owe big thanks to my co-advisor, Axel Drees, who showed nothing but support for this project and my decision to carry on and finish the work in Berkeley. Thank you to Ali Hanks, who acted as a long-term sheppard, has shared the most first-hand experience and knowledge of the analysis methods and coding techniques. I learned from her to develop independent thinking and good coding habit.

I am truly grateful to the Stony Brook Relativistic Heavy Ion Group (RHIG). Tom Hemmick, from whom I greatly benefited in the early days when learning programming and detector technologies. I would like to thank my officemates and friends: Wenqing Fan, Serpil Yalcin, Chin-Hao Chen, Ciprian Gal, Andrew Manion, Benjamin Bannier for discussions and help. Encouragement and knowledge sharing from the senior will certainly not be forgotten: Deepali Sharma, Alan Dion, Yorito Yamaguchi, Klaus Dehmelt, Ermias Atomssa, Baldo Sahlmueller.

I would like to thank the experts from PHENIX HHJ working group and two-particle correlation topical group, especially Megan Connors, Justin Frantz and Nathan Grau for offering insights and promoting discussions.

I was fortunate to be able to work in the Relativistic Nuclear Collision (RNC) group at Lawrence Berkeley Lab, where I benefited from useful discussions with Xin-Nian Wang, Peter Jacobs, Yue-Shi Lai, Miguel Arratia, Jochen Thaeder etc. I greatly appreciate the help of Fernando Acosta for reading my thesis chapters and providing useful comments.

A few special thanks to the following folks:

Alex Schmah, who integrated me with the RNC group and selflessly shared expertise in jet physics while propelling me to "work faster".

Sanshiro Mizuno, with whom I was happy to share common passion for sports and good Chinese food, has also inspired me with his hard-working nature and helped me with the ex-PHENIXian intuition.

Jinlong Zhang, Xu Sun and Guannan Xie, my weekend work buddies, invited me to be a part of the Berkeley Lab Chinese community where I felt like home.

Jiayin Sun, a comrade who was always available when I needed a pair of

fresh eyes for debugging, understood and put up with my occasional whining and frustration with analysis work.

Wolfger Peelaers, who has supported and encouraged me during my PhD study since day one.

Last but not least, I am grateful to my family for the understanding and support all along for whatever I choose to pursue.

Chapter 1

Introduction

With the advances and rapid development of science and technology, we are in an era of exploring and conquering the outer space, reaching out to seek any possible extraterrestrial life and probing the possibility of creating artificial intelligence. Mankind has never stop to pursue an answer to the ultimate question: "where do we come from?"

Well before any human civilization, the universe was created after "the Big Bang" and has not stopped expanding since. For a very brief moment, free quarks and gluons existed - forming a state we now refer to as the quark-gluon plasma (QGP). As fleeting as it is, such matter encodes the information of how matter behaved at the very start of the universe. Recreating QGP in experimental settings and studying its properties are of great importance in taking us "back in time" and understanding the world we live in.

This dissertation presents a study of this hot, dense and strongly coupled QCD matter, using jets as a probe. The interactions between the propagating jet and the created medium are studied via two-particle correlations. Direct photons are chosen as triggers to serve as a caliber of the initial jet energy, allowing one to quantify the modification of the associated jets.

This chapter is dedicated to give a brief overview to our current understanding of QGP via relativistic heavy ion collisions. Section 1.1 and 1.2 introduce the Standard Model and Quantum Chromodynamics. Relativistic heavy ion collisions and properties of quark-gluon plasma are described in section 1.4. Jet quenching, one of the most celebrated revelation, is introduced in section 1.6, along with recent development for energy loss study, both experimentally and in theory ground. In particular, the Linear Boltzmann Transport (LBT) model and Monte Carlo event generator JEWEL are

discussed in section 1.6.3. Two particle framework and γ_{dir} -h correlations are described in section 1.6.1 and 1.7.

1.1 The Standard Model

Developed in the early 1970's, the standard model (SM) of particle physics, has been enjoying its triumph in describing various experimental observations as well as predicting interesting phenomena and discoveries. The SM is by far the most fruitful and well-tested theory for describing the basic building blocks of matter and how they interact with each other. Built on symmetries, it is able to unify electromagnetism, quantum mechanics and special relativity. It can successfully describe the three out of four fundamental forms of forces in nature: the electromagnetic, weak and strong forces. All the elementary particles including force-carriers can be classified according to the SM. Table 1.1 summarizes the four fundamental forces in the universe, with the corresponding theory for each type, together with the relative strength in the order of low to high (gravitation force being the weakest). The gravitational force is listed for completeness although it is not included in the SM.

In the language of group theory, the SM is represented by $SU(3) \times SU(2) \times U(1)$, with $SU(3)$, $SU(2)$ and $U(1)$ corresponding to the three kinds of interactions: strong, weak and electromagnetic, respectively.

Force	Theory	Relative strength	Range (m)	Force carriers
Gravity	General Relativity	1	∞	graviton
Weak	Electroweak	10^{25}	10^{-18}	Z^0, W^\pm
Electromagnetic	QED	10^{38}	∞	photon (γ)
Strong	QCD	10^{41}	10^{-15}	gluon (g)

Table 1.1: A summary of the four fundamental forces in nature and each corresponding theory that governs with the listed interaction range, relative strength and force carriers.

1.2 Quantum chromodynamics

Quantum chromodynamics (QCD), the special unitary group $SU(3)$ component of the Standard Model, is a gauge field theory that governs the strong interactions between quarks and gluons.

Extended from the same theoretical framework, QCD shares similar characteristics but also contains its own distinctive features, as compared to quan-

tum electrodynamics (QED). Analogous to the electric charge in QED, a special property referred to as the color charge is carried by quarks and gluons in QCD. There are six flavors of quarks: up, down, charm, strange, top and bottom. In nature, objects most elementary are observed to be color-neutral hadrons. They are made of either three quarks, forming baryons, or by a quark and anti-quark pair forming mesons. The binding force that holds the individual partons together are called the color force. Gluons are the force carriers in the QCD picture. There are three base colors that (anti)quarks carry: (anti)red, (anti)green and (anti)blue. Gluons therefore carry combinations of color and anticolors. There are in total eight types of gluons.

Unlike photons, the mediators in QED, gluons can interact among themselves because of the color charges they carry, giving complexities in calculations in QCD. The Feynman diagrams shown in Fig. 1.1 coincide with the quark-antiquark-gluon ($q\bar{q}g$), 3-gluon and 4-gluon vertices.

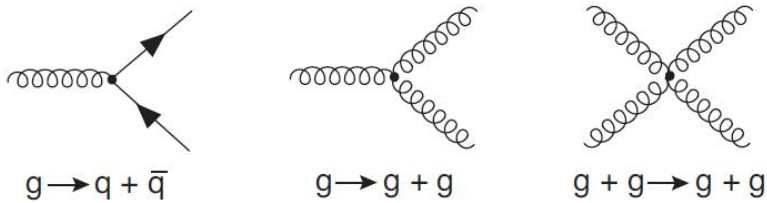


Figure 1.1: Feynman diagrams of vertices in QCD [82]

Two distinctive characteristics of QCD are known as confinement and asymptotic freedom. They are first proposed by Gross, Politzer and Wilczek [2]. Confinement describes the phenomenon that the binding energy between partons becomes larger as they are further separated. α_s , denoting the coupling constant that describes the interaction strength, has been measured in various experiments. Fig. 1.2 shows α_s from pQCD calculation, compared with results from experimental measurements, as a function of the energy scale Q . At small Q , the coupling drastically becomes strong. The large coupling forces the partons to be bound in color-neutral states. This is in contrary to the coupling α in QED, which increases as distance gets smaller.

One can also see in Fig. 1.2 that the observed α_s decreases as the momentum transfer Q becomes much larger. At sufficiently high energy scale, quarks and gluons are no longer bound and become "deconfined". This is known as asymptotic freedom, meaning that matter dissolves because the

color interactions among partons become weaker and disappear as the energy scale approaches infinity. In reality, such large Q is achievable through bombarding particles at very high energy using modern particle accelerators.

Only under extreme conditions, such as high temperature and density, unconfined quarks and gluons occurred in nature, a few μs after the Big Bang. This state of matter is called the quark gluon plasma (QGP). It is a surprisingly strongly coupled state of matter, in which the color charged quarks and gluons interact among themselves via strong force, even though they are no longer confined inside hadrons. Before discussing more on the formation and properties of QGP, we first present the QCD language that describes strong interactions.

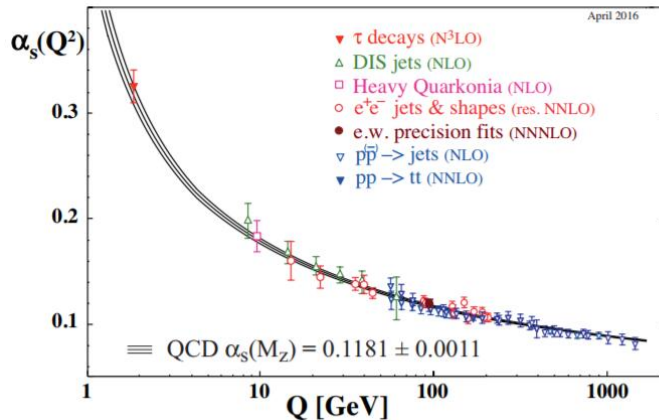


Figure 1.2: Measurements of α_s as a function of the energy scale Q from PDG2016 [1]

1.3 QCD calculations

The QCD Lagrangian is expressed as follows [1]:

$$L = \sum_q \bar{\phi}_{q,a} (i\gamma^\mu \partial_\mu \delta_{ab} - g_s \gamma^\mu t_{ab}^C A_\mu^C - m_q \delta_{ab}) \phi_{q,b} - \frac{1}{4} F_{\mu\nu}^A F^{A\mu\nu} \quad (1.1)$$

where the $\phi_{q,a}$ are the quark-field spinors for quark with flavor q and mass m_q . The index a stands for color and runs from 1 to 3 to include three color

flavors ($N_c = 3$). γ^μ are the Dirac γ -matrices. g_s is related to the coupling constant ($\alpha_s = \frac{g_s^2}{4\pi}$). A_μ^C represents the gluon fields and C goes from 1 to 8, corresponding to eight kinds of gluons. The generators of the SU(3) group are encoded in the 3×3 matrices t_{ab}^C . The field tensor $F_{\mu\nu}^A$ is given by:

$$F_{\mu\nu}^A = \partial_\mu A_\nu^A - \partial_\nu A_\mu^A - g_s f_{ABC} A_\mu^B A_\nu^C \quad (1.2)$$

with f_{ABC} being the structure constants of the SU(3) group.

The scale dependent coupling constant, α_s , depends on the momentum transfer Q. The beta function can be expressed in a perturbative series in α_s as below:

$$\beta(\alpha_s) = b_0 \alpha_s^2 + \mathcal{O}(\alpha_s^3) \quad (1.3)$$

where b_0 is determined by pQCD calculations at leading order to be:

$$b_0 = -\frac{33 - 2N_f}{12\pi} \quad (1.4)$$

with N_f being the number of quark flavors. The strong coupling constant α_s is determined to be:

$$\alpha_s(Q^2) = \frac{1}{b_0 \log(Q^2/\Lambda^2)} \quad (1.5)$$

where Λ is the scale at which the coupling defined by perturbation theory no longer holds.

Perturbative QCD runs into its limitations when the calculation involves long-range interactions and lower energy. In those cases, the coupling constant α_s becomes large and contributions from next-to-leading order (NLO) processes are no longer negligible, considering additional vertices in Feynmann diagrams. Lattice QCD, which does calculation through computations on a finite lattice, rather than in a continuous space and time, is successful in predicting the transition from a hadronic phase to a QGP phase at high temperature and small baryon density, as will be discussed more in section 1.4.

Experimentally, one can explore the interactions at the partonic level and study perturbative QCD by colliding particles at high energy. The most elementary example is the e^+e^- collisions. An electron and positron produce an outgoing quark and anti-quark $e^+ + e^- \rightarrow q + \bar{q}$. However due to confinement, no individual quarks and gluons can be observed in the detectors, only color-neutral hadrons. As will be discussed below, the collimated spray

of hadrons fragmented from the outgoing partons are known as jets. Hard-scattering processes involving hadrons in the final states are factorizable, so the cross section can be written as a convolution of the parton distribution functions (PDFs) of the incoming nucleons, the hard partonic process and the fragmentation function (FF). This QCD factorization theorem can be expressed as the following:

$$d\sigma_{AB \rightarrow h} = f_{a/A}(x_a, Q^2) \otimes f_{b/B}(x_b, Q^2) \otimes d\sigma_{ab \rightarrow c}(x_a, x_b, Q^2) \otimes D_{c \rightarrow h}(z, Q^2) \quad (1.6)$$

On the right side of the equation, the first two terms describe the PDFs for parton a and b, respectively. The PDF encodes the probability of finding a parton carrying a certain fraction of the proton momentum in a hard scattering with energy scale of Q . x_a and x_b then denote the initial momentum fraction the parton a and b carry. Typically the shapes of the PDFs are determined through fits to experimental data from deep inelastic scattering (DIS) processes. The fragmentation function $D_{c \rightarrow h}(z, Q^2)$ represents the probability of a parton to fragment into a hadron carrying a fraction of the parent parton momentum, where variable z is the momentum fraction: p^{hadron}/p^{parton} . An alternative variable ξ is often used as well: $\xi = \ln(1/z)$, as will be discussed more in the later sections. $d\sigma_{ab \rightarrow c}$ is the differential cross section of the parton scattering process. This equation can be viewed as two parts: the PDFs and hard-scattering process describe the perturbative component which is related to the initial state, together with a fragmentation component depicting the hadronization process which is related to the final state. The fragmentation process is independent of the initial state process itself, but only depends on the outgoing partons that are produced from there. Fig. 1.3 shows a few examples of the parton distribution functions. The shapes of PDFs are usually determined from fits to experimental data, i.e. Deep Inelastic Scattering (DIS) HERA and fixed target data. Fig. 1.4 shows some examples of fragmentation function measurements.

1.4 Quark Gluon Plasma: A New State of Matter

Early lattice QCD calculations predicted a deconfined state of matter at a temperature of about 150 MeV, with a phase transition requiring an energy

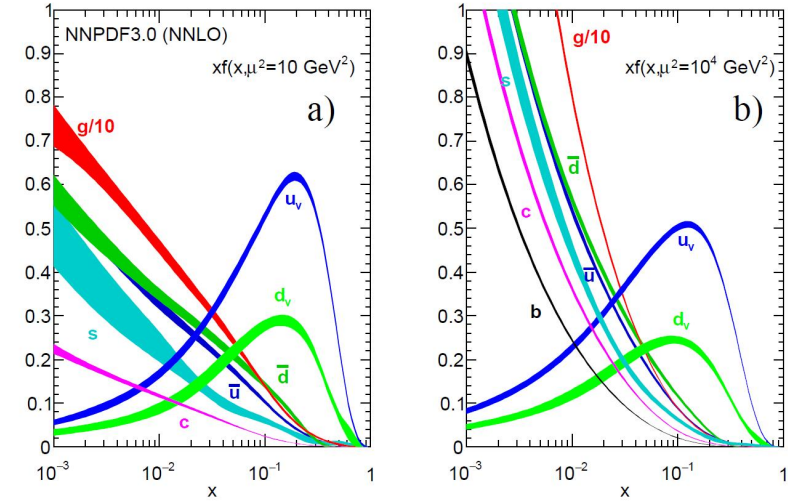


Figure 1.3: Examples of parton distribution functions [1]

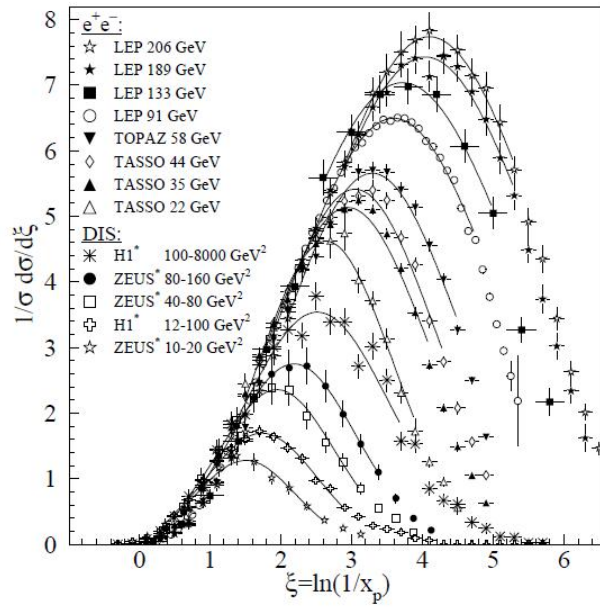


Figure 1.4: Fragmentation functions in terms of ξ distributions measured in $e^+ + e^-$ and DIS processes [1].

density about $\epsilon \sim 1 \text{ GeV}/fm^3$. Fig. 1.5 is a cartoon for the QCD phase diagram, illustrating the relation between temperature T and baryon chemical potential μ . As the temperature and baryon density increase, there should be a first order phase transition from normal nuclear matter to a deconfined matter: quark gluon plasma (QGP). A QGP is a state of QCD matter that consists of asymptotically free strong-interacting quarks and gluons. So far no well-defined critical point of the phase transition has been determined. Instead the transition is more like a rapid crossover region, where thermodynamic properties of matter such as energy and entropy density undergo a swift change. Fig. 1.6 shows a calculation of the pressure, energy density and entropy density normalized by $1/T^4$ and $1/T^3$ respectively, reported by the HotQCD Collaboration [36]. The critical temperature T_c is shown as the yellow band in the figure and the value is determined to be $154 \pm 9 \text{ MeV}$. This temperature corresponds to a chiral phase transition where the up, down and strange quarks gain physical masses [37].

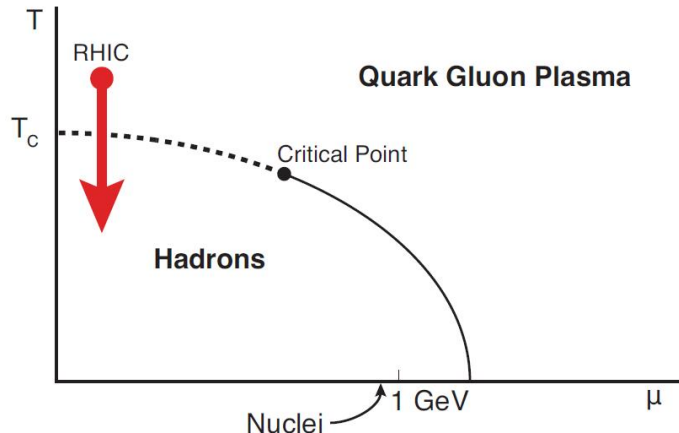


Figure 1.5: A simple schematic of the QCD phase diagram: a phase transition happens at the crossover region near which normal nuclear matter changes to quark-gluon plasma, a dense and hot medium in which partons are deconfined.

In order to recreate the state of matter that existed a μs after the big bang and study its properties, the relativistic heavy ion colliders have been built.

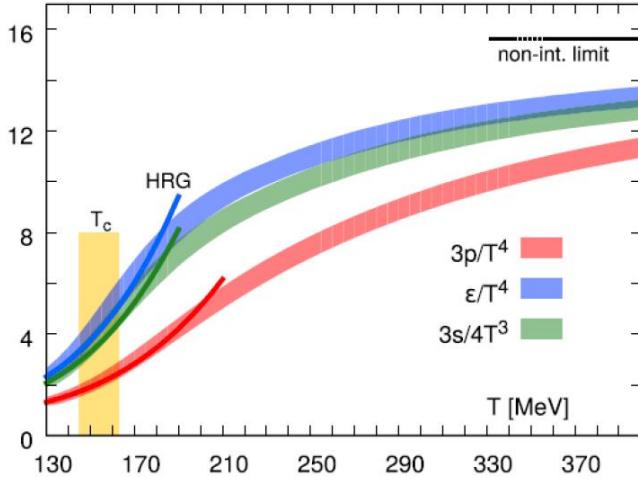


Figure 1.6: Pressure, energy density and entropy density normalized by $1/T^4$, $1/T^4$ and $1/T^3$. This is the Lattice QCD calculations from Hot QCD collaboration [36]. Solid lines represent the predictions from the hadron resonance gas (HRG) model. T_c is marked as the vertical yellow band. The horizontal line denotes the ideal gas limit with the value of $95\pi^2/60$.

Experimental apparatus at the Relativistic Heavy Ion Collider (RHIC) will be discussed in chapter 2. Critical evidence of the discovery of QGP formation at RHIC includes collectivity, temperature and jet quenching, discussed in section 1.4.2, 1.5 and 1.6. Overview papers discussing the evidence for QGP discoveries from PHENIX, STAR, PHOBOS and BRAHMS experiments at RHIC are reported in Ref. [38, 39, 40, 41].

At RHIC, heavy ion beams made of gold nuclei are accelerated and collide at different interaction points around the collider ring. Fig. 1.7 illustrates the evolution process of QGP from the beginning of a collision. The two gold ions are Lorentz contracted, as they are accelerated to relativistic velocities. When they collide, there is an overlap region where the nucleons from the two ions interact, from which high momentum particles are produced. There are also components in the overlapping region that thermalize and form a hot and dense strongly coupled medium. This state of matter is known as the quark-gluon plasma (QGP), in which color-charged quarks and gluons are no longer bound. The system then expands and cools, and partons combine

into color-neutral states and hadronize into final detectable particles. This corresponds to "fragmentation". The hadron gas further cools and expands to the freeze out stage, in which particles no longer interact with each other but free stream towards the detectors.

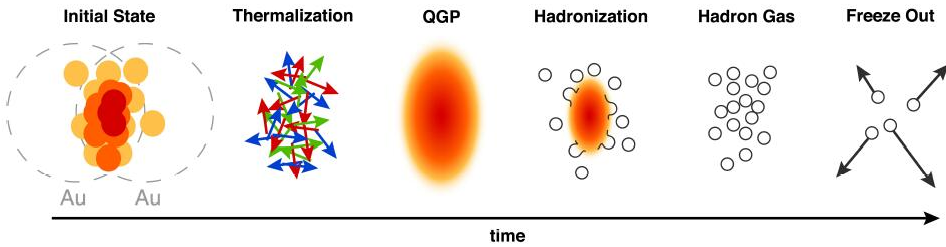


Figure 1.7: A schematic of the QGP evolution with time.[82]

1.4.1 Collision geometry and the Glauber Model

Relativistic heavy ion collisions produce high multiplicities of outgoing particles. Events are typically categorized in terms of centrality according to their initial collision geometry. Before defining the notion of centrality, a few quantities characterizing collision geometry are listed:

- impact parameter b - distance between the two colliding nucleon centers, as shown in Fig. 1.8.
- N_{part} - total number of nucleons engaged in a collision, that suffer at least one inelastic collision.
- N_{coll} - total number of binary collisions per event.

Centrality is a concept that depicts the overlap region of the two colliding nuclei, therefore is essential to characterize the initial collision geometry. It is defined in terms of a percentage of the total nucleus-nucleus interaction cross section. A small centrality refers to a central or "head-on" collision, and a large value corresponds to a peripheral or "grazing" collision. Centrality usually ranges from 0% to 100%, corresponding to impact parameter b being 0 and $R_A + R_B$, respectively. N_{part} , N_{coll} and centrality can be calculated using the Glauber Model [58, 59].

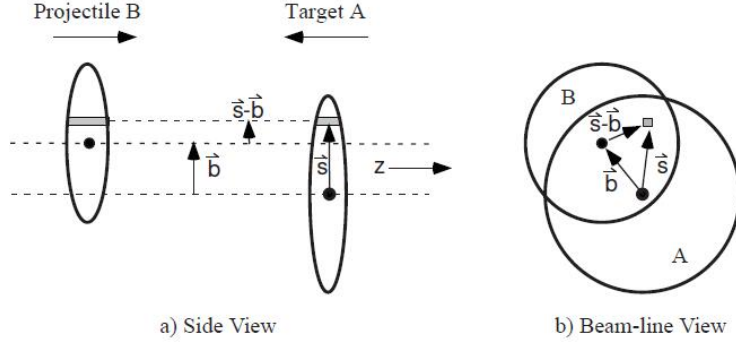


Figure 1.8: Collision geometry

The nucleon charge density is the key input to a Glauber model. It is typically described by a Fermi distribution:

$$\rho(r) = \rho_0 \frac{1 + \omega(r/R)^2}{1 + \exp(\frac{r-R_A}{a})} \quad (1.7)$$

where $\rho_0 = 0.16 \text{ fm}^{-3}$ is the normal density for nuclear matter, a is the "skin depth", the characteristic charge radius $R_A \approx 1.2A^{1/3}\text{fm}$ (A - atomic mass) [60], ω parametrizes deviations from a spherical shape.

For heavy spherical nuclei such as Gold and Lead, this can be simplified using the Wood-Saxon approximation:

$$\rho(r) = \frac{\rho_0}{1 + \exp(\frac{r-R_A}{a})} \quad (1.8)$$

$R = 6.38 \text{ fm}$, $a = 0.535 \text{ fm}$ for ^{197}Au nucleus,

Fig. 1.9 shows the multiplicity distribution from the Glauber calculation. Along the curve, the collision geometry and the corresponding centralities are indicated. The impact parameter b and N_{part} related to the specific geometry configuration are shown on top of the figure. One can see that small impact parameter corresponds to large N_{part} and more central collisions.

1.4.2 Collectivity and Elliptic Flow

As most heavy ion collisions involve finite impact parameters, the overlap region of the colliding two nuclei, shown in the left plot in Fig. 1.10, has

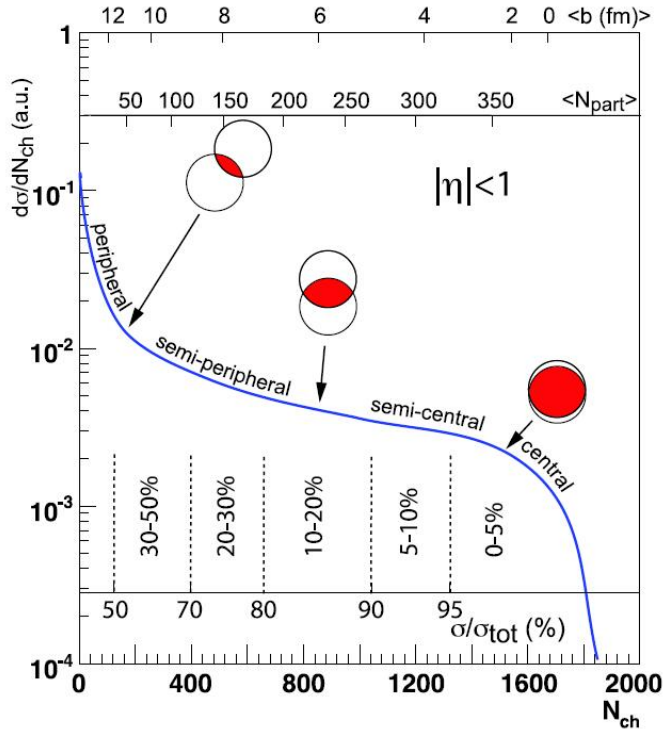


Figure 1.9: Multiplicity distribution demonstrating the relationship between impact parameter, N_{part} , collision centrality [59].

an "almond" shape. The asymmetry in the spatial distribution results in an anisotropy in the momentum space of the outgoing partons. As discussed before, a central collision corresponds to a small impact parameter while a peripheral event has a relatively large impact parameter; the former corresponds to a "fatter" almond shape. The density anisotropy in the overlapping region causes a pressure gradient, which results in more particles to flow in the direction in the collision reaction plane. This phenomenon is referred to as the elliptic flow.

The right-hand side cartoon in Fig. 1.10 is a typical image of a semi-central collision with the overlapping region being elliptical. The arrows illustrate the momentum direction of the particles coming from this interaction region. More particles will be emitted along the x-z plane because the pressure gradient is higher. We define the x-z plane as the event plane and it is shown as the grid in Fig. 1.10. Flow can be quantified in terms of

the coefficients of a Fourier decomposition of the azimuthal distributions of particles measured with respect to the event plane.

$$\frac{dN}{d(\phi - \Psi_k)} \propto 1 + \sum_n v_{kn} \cos n(\phi - \Psi_k) \quad (1.9)$$

where ϕ is the particle azimuthal angle, Ψ_k stands for the event plane orientation in one event labeled with k . v_{kn} corresponds to the n^{th} coefficients for the given k^{th} event plane.

The quadrupole term v_2 is the dominant source of the momentum anisotropy. The measured v_2 can be well described by hydrodynamical models, revealing the liquid characteristics of the created medium. QGP has extremely small dissipation, which can be described by its shear viscosity to entropy density ratio η/s . Therefore it is sometimes referred to as the "perfect fluid". One important finding with the elliptic flow measurement is its quark scaling nature, shown in Fig. 1.11. The kinetic energy dependence of the measured v_2 show distinction between mesons and baryons. However when we plot v_2/n_q as a function of kE_T/n_q , i.e. scale by the number of valence quarks n_q , all particle v_2 lie on top of each other. This corresponds to the picture that the quarks carry the momentum anisotropy rather than the collective flow developed in the later hadronic phase. This is a strong indicator of the formation of the QGP in which quarks and gluons are deconfined. Apart from hadrons, low momentum direct photons are also found to be carrying non-negligible v_2 . This is related to the production mechanism of direct photons. Information on the thermal contribution to the direct photon yield in the low momentum region can be useful to interpret the temperature of the medium. More is discussed in section 1.5

1.5 Direct photons

In the analysis which will be presented later in this dissertation, we use high momentum direct photons as triggers and measure the associated hadron yields. Fig. 1.12 shows the Feynmann diagrams for the leading order photon production. Panel (a) corresponds to the quark-gluon QCD Compton-like scattering $q + g \rightarrow q + \gamma$, which is the dominant channel for prompt photon production. Panel (b) represents the the quark-antiquark annihilation channel: $q + \bar{q} \rightarrow g + \gamma$. Additionally, photons can come from the fragmentation of quarks or gluons, as bremsstrahlung radiation or from the parton-medium

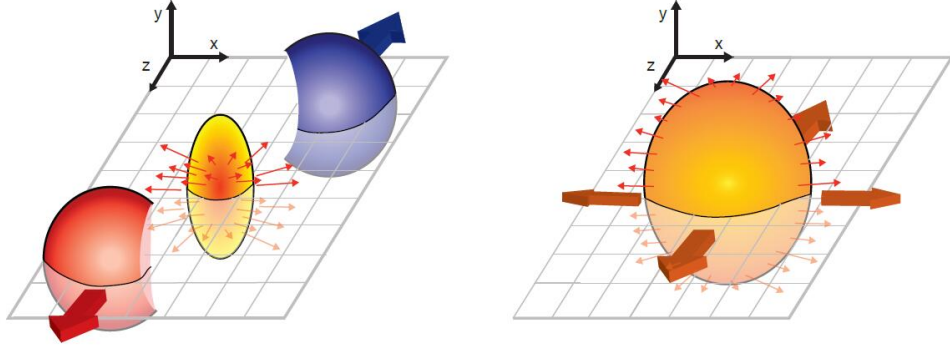


Figure 1.10: Cartoons illustrating elliptic flow, event plane and momentum anisotropy.

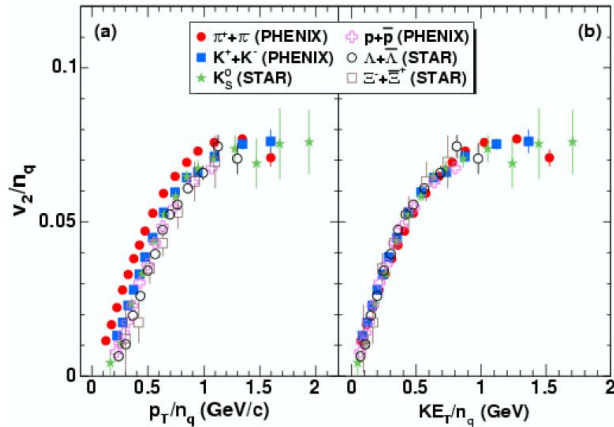


Figure 1.11: v_2 as a function of transverse momentum and energy, scaled by the number of constituent quarks, for various particle species.

interaction. At low transverse momentum, photons can also be produced from thermal radiation. Fig. 1.13 lists the next-to-leading order diagrams for the fragmentation photon production. Note that the direct photons we refer to are all photons that are not from a decay process. Therefore prompt photons from initial hard scattering and those fragmentation photons both contribute to the measured trigger sample.

Fig. 1.14 is a recent direct photon measurement from the ALICE experi-

ment for centrality ranges of 0-20%, 20-40% and 40-80%. For $p_T \geq 5$ GeV/c, the direct photon yield is consistent with expectation from pQCD calculations for p+p collisions that is scaled up by the number of binary collisions N_{coll} . For photons with $p_T < 2$ GeV/c in 0-20% and 20-40% centrality bins, an excess on top of the prompt photon yield is observed. The effective temperature T_{eff} of the medium is calculated to be about $297 \pm 12^{stat} \pm 41^{sys}$ MeV by fitting the spectrum with an exponential function [42].

Direct photons have also been measured in PHENIX. The R_γ - the ratio of number of inclusive photons to decay photons - used in this $\gamma_{dir}-h$ analysis are taken from a separate previous measurement in Ref. [77].

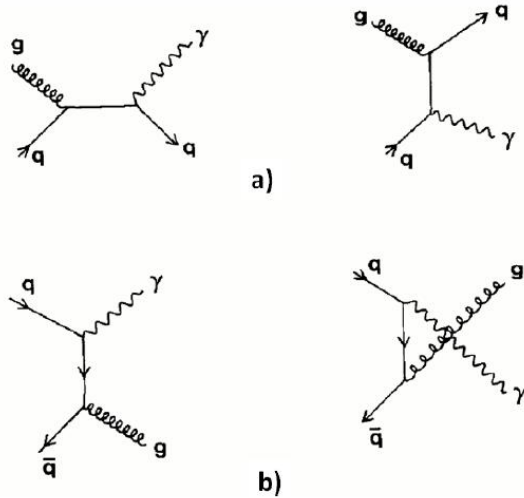


Figure 1.12: Direct photon production at leading order (LO).

1.6 Jet Quenching and Parton Energy Loss

Jets, which comprise a collimated spray of final state particles, are observed to be suppressed in heavy ion collisions compared to those in p+p. This is a phenomenon known as "jet quenching". It was discovered at RHIC and LHC that a surprisingly large suppression of inclusive hadrons was observed at high p_T . This phenomenon is a signature of the formation of the strongly coupled dense medium. The group of particles that forms a jet are usually fragmented from a high energy parton, which comes from an initial hard scattering. The

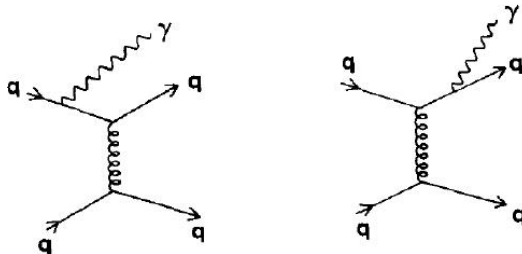


Figure 1.13: Direct photon production at next-leading-order (NLO).

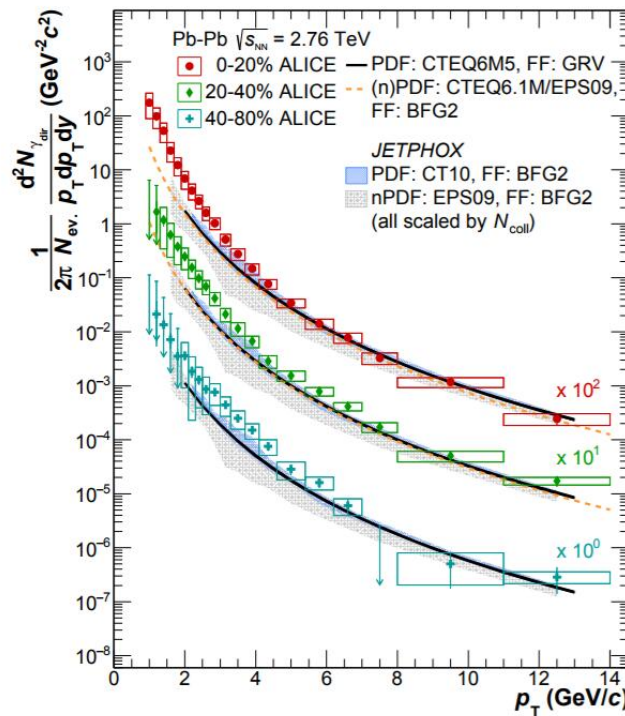


Figure 1.14: Direct photon spectra in 0-20%, 20-40% and 40-80% Pb+Pb collisions measured by ALICE. The yields are compared to NLO pQCD predictions for direct photon yield in pp collisions scaled by N_{coll} .

parton interacts with the created hot and dense medium and lose energy when traversing through. This is observed in the final observables of hadrons. A "nuclear modification factor" is defined to quantify the difference between

heavy-ion collisions and the p+p baseline measurement:

$$R_{AA} = \frac{d^2N_{AA}/d\eta dp_T}{\langle T_{AA} \rangle d^2\sigma_{pp}/d\eta dp_T} \quad (1.10)$$

where $dN_{AA}/dydp_T$ is the differential yield measured in AA collisions and $d\sigma_{pp}/dydp_T$ is the inelastic cross section in p+p collisions. $\langle T_{AA} \rangle$ is the nuclear thickness function, defined as $\langle N_{coll} \rangle / \sigma_{NN}$ with $\langle N_{coll} \rangle$ being the average number of binary collisions in one event and σ_{NN} being the nucleon-nucleon cross section.

Figure 1.15a is R_{AA} measured in PHENIX for direct photons, identified hadrons and non-photonic electrons in 0-10% most central Au+Au collisions at $\sqrt{s_{NN}} = 200$ GeV. The direct photons are color neutral objects and do not interact with the medium via the strong force. The mean free path of photons is larger than the created medium size, so they do not interact with the surroundings electromagnetically either, resulting in the measured R_{AA} being consistent with unity. Hadrons on the other hand, are observed to show a large suppression at high p_T in central heavy ion collisions. Similar results from ALICE and CMS experiments are obtained at the LHC, shown in Figure 1.15b, demonstrating that the jet quenching phenomenon exists in QGP created with much higher collision energy. This violation of the binary scaling indicates that nucleus-nucleus collisions are not simply a superposition of the elementary nucleon-nucleon collisions. The depletion in the yield can be viewed as a combination of a downward and leftward shifts of the spectra of hadrons in A+A collisions. This is caused by high momentum jets losing some fraction of their original energy from the partons, resulting in an overall change in the spectral shape. The suppression is found to be stronger in more central collisions.

Apart from the single particle observables, jet quenching manifests itself in reconstructed jet and correlation measurements. An important di-jet measurement from the ATLAS experiment presents the first evidence of jet quenching in reconstructed jets at the LHC. The dijet asymmetry, A_J is defined as follows:

$$A_J = \frac{E_{T,1} - E_{T,2}}{E_{T,1} + E_{T,2}} \quad (1.11)$$

where $E_{T,1}$ and $E_{T,2}$ represent the transverse energy of the leading and sub-leading jets, respectively. The top four panels in Fig. 1.16 are the measured

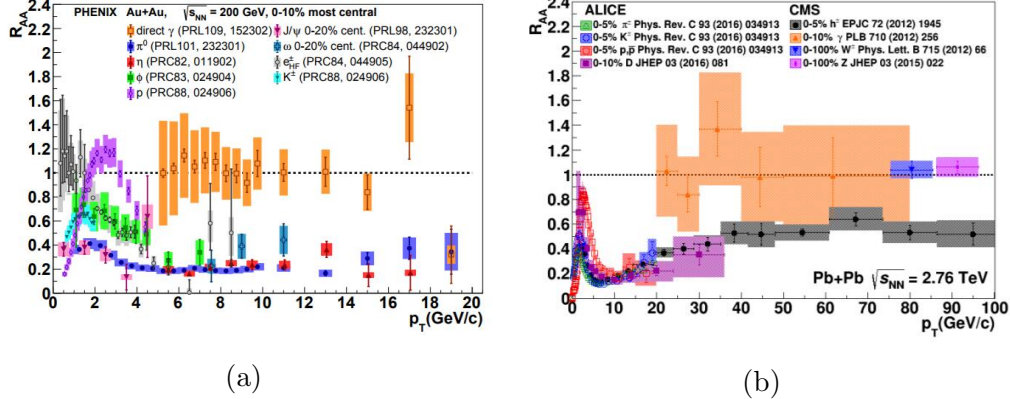


Figure 1.15: (a): R_{AA} measured in PHENIX for direct photons, identified hadrons and non-photonic electrons in 0-10% most central Au+Au collisions at $\sqrt{s} = 200$ GeV. (b): R_{AA} for identified π^\pm , K^\pm , (anti)protons and D mesons from ALICE and charged hadrons, direct photons, W and Z bosons from CMS.

A_J distributions for Pb+Pb and p+p collisions at $\sqrt{s_{NN}} = 2.76$ TeV in four centrality ranges, with requiring the leading jet energy $E_T > 100$ GeV. The dijet asymmetry in peripheral Pb-Pb collisions is comparable to what is measured in p+p as well as that from the PYTHIA simulation. For more central Pb+Pb events, however, the A_J distributions show distinctive shift from zero, suggesting more asymmetric dijets being detected. The four plots in the bottom panel is the distributions of $\Delta\phi$ between the leading and sub-leading jets. The distributions peak at $\Delta\phi = \pi$ rad, indicating that the leading and sub-leading jets are produced back-to-back and the secondary jets lose energy in the medium, giving a large imbalance observed in central Pb-Pb events.

1.6.1 Two particle correlations

Apart from single hadron and reconstructed jet measurement, one can study the jet energy loss through two particle correlations. Generally it is achieved by triggering on high p_T particles and use them as a proxy for the opposing jet. We then pair other particles with the trigger and refer to those as the partners. One can study jet energy loss by measuring the yield of the associated partners with azimuthal angle difference $\Delta\phi$ to the triggers. A

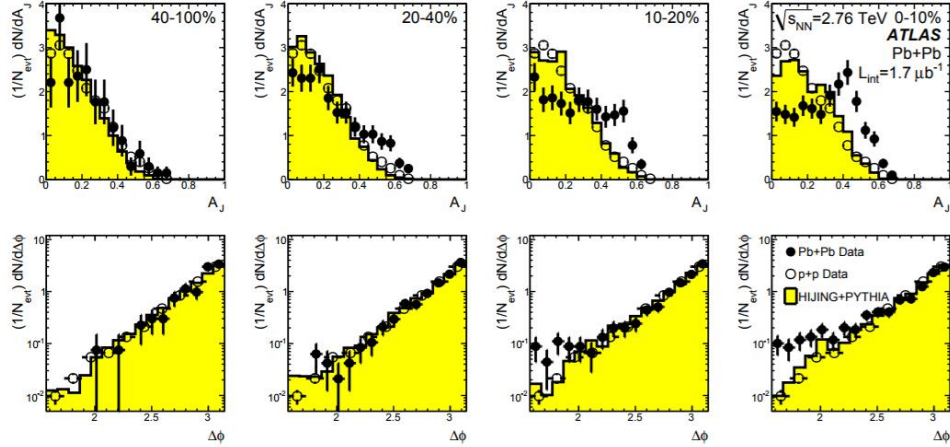


Figure 1.16: Upper panel: Dijet asymmetry A_J distributions in various centrality bins in Pb+Pb collisions at $\sqrt{s_{NN}} = 2.76$ TeV (solid dots). For comparison, p+p points from collisions at $\sqrt{s} = 7$ TeV are shown in open circles. Lower panel: Dijet azimuthal angle $\Delta\phi$ distributions for data and simulation, as a function of centrality.

typical correlation function is depicted by the cartoon in Fig. 1.17. The jet coming from the trigger particle appears as the peak near $\Delta\phi = 0$ while the opposing jet from the trigger particle creates the peak at around $\Delta\phi = \pi$. This cartoon is a typical illustration for correlations in p+p collisions in which the background from underlying event is relatively flat and produces a pedestal. Here we define the conditional yield, or per-trigger yield, as the following:

$$Y(\Delta\phi) = \frac{1}{N^{trig}} \frac{dN}{d\Delta\phi} \quad (1.12)$$

where N^{trig} denotes the number of triggers and $\Delta\phi$ is the azimuthal angle between the trigger and partner particle.

Fig. 1.18 shows a hadron-hadron correlation measurement from the STAR experiment for p+p, d+Au and Au+Au collisions. The p+p data shows a similar shape as the cartoon in Fig. 1.17. In Au+Au, however, the away-side peak is strongly suppressed. The agreement between the d+Au and p+p result confirms that the modification seen in Au+Au is in fact coming from a hot nuclear matter effect.

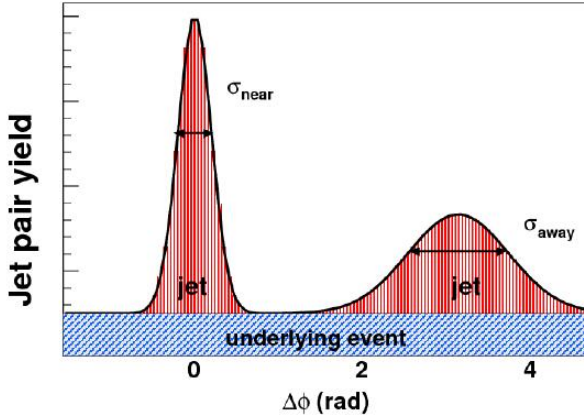


Figure 1.17: A cartoon illustrating two-particle correlations.

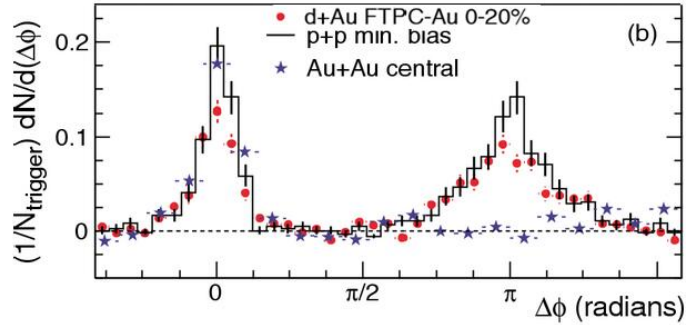


Figure 1.18: Dihadron measurement in p+p, d+Au and Au+Au collisions.

Observation of the suppression of measured reconstructed jet R_{AA} is also confirms that jets are quenched in QGP. However, several following questions remain:

- How are the jets affected by the medium?
- How is the medium affected by the propagating jets?
- Where does the lost energy go?
- How do jets fragment?

Measurements probing the inner structures of jets could be used as attempts to answer these questions.

1.6.2 Probing Jet Substructure

More differential measurement is needed for disentangling the medium effect on the propagating jets and to shed light on the parton in-medium energy loss mechanism. Fig. 1.19 is an illustration of the evolution process of a full jet inside a QGP. The thick solid arrow represents the transporting direction of the leading parton inside the jet with a cone size R , defining the propagation direction of the jet. The rest of the solid arrows are the less energetic partons. Dashed arrows stand for radiated gluons; some gluons are contained inside the jet cone and some with larger angles are scattered outside the reconstructed jet size. The total energy loss of the jet could be considered as a total sum of the energy loss of the leading parton and the accompanying gluons, as well as the loss of gluons which are deflected towards larger angles with respect to the jet axis and as a result not contained inside the reconstructed jet cone.

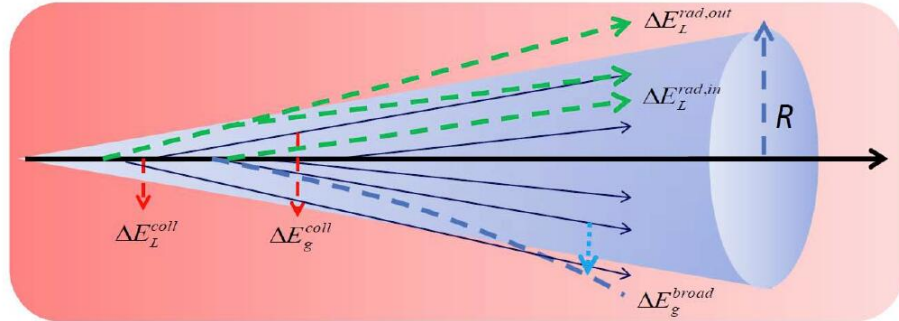


Figure 1.19: A schematic of the evolution of a full jet in a QGP [6].

Measuring The Fragmentation Function

The definition of the jet fragmentation function $D(z)$ can be written as below:

$$D(z) = \frac{1}{N_{jet}} \frac{dN_h}{dz} \quad (1.13)$$

where $z = p_T^h/p_T^{jet}$ is the momentum fraction carried by the hadron fragmented from the jet. The fragmentation function is sensitive to the modification of the spectrum of the jet fragments. As the highly energetic jet propagates through the medium, the leading parton loses energy while a significant amount of soft radiation from the jet-medium interaction occurs. The ATLAS experiment measured the modification of the jet fragmentation function via reconstructed charged jets with cone sizes of $R = 0.4$. Fig. 1.20 shows the ratios of fragmentation functions in more central collisions to those in the peripheral centrality 60-80% bin. The ratios show enhancement at the small z region and a depletion in intermediate z for all centrality bins. Using an alternative variable $\xi = \ln(1/z)$ to zoom in at the low z region, one sees a similar result from the CMS collaboration [101] shown in Fig. 1.21. The top panel is the measured Pb+Pb jet fragmentation functions in the form of track ξ distributions together with the p+p reference in the overlaid histograms. The bottom panel is the corresponding ratio of $Pb + Pb/p + p$. A significant enhancement at large ξ is visible for central collisions. The observed modification of the jet fragmentation function in central Pb+Pb collisions could possibly come from changes in the parton shower due to the presence of the medium: a redistribution of the energy and generation of extra soft particles from the medium response.

Medium effect on jets, jet shapes and broadening

The differential jet shape variable is defined as [26]:

$$\rho(r) = \frac{1}{\delta r} \frac{1}{N_{jet}} \sum_{jets} \frac{\sum_{tracks \in [r_a, r_b]} p_T^{track}}{p_T^{jet}} \quad (1.14)$$

This observable $\rho(r)$ is essentially measuring the transverse momentum distribution in the radial direction inside a jet. With the assumption that a jet is conical, the jet axis is determined using a jet finding algorithm. The sum of the track p_T around the jet axis can be calculated, as can the total p_T within certain concentric rings with radii of r_a and r_b . δr refers to the width of the selected ring.

The upper panels in Fig. 1.22 demonstrate the differential jet shapes as a function of r in Pb+Pb collisions for various centrality bins, compared to the baseline p+p measurement, reported by CMS. The lower panels show the ratios of Pb+Pb to p+p, and are normalized to unity. The ratios show

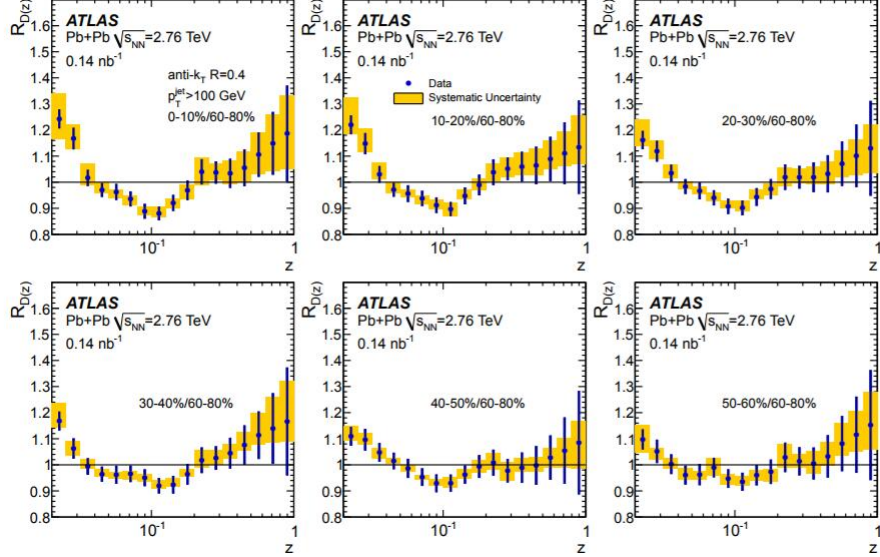


Figure 1.20: Ratio of fragmentation functions for central to peripheral Pb+Pb events, as a function of z , measured using anti- k_T jets of cone size of $R = 0.4$.

a centrality dependence, with more modification observed in more central Pb+Pb collisions. The result demonstrates that the extra energy is located at larger radii with respect to the jet axis in central Pb+Pb collisions.

In recent jet quenching studies, newer observables are constructed to serve as better measures of the jet substructure. This is a partial result of the progress in jet algorithm development and implementation in experimental studies. Interesting new observables such as the jet mass, the splitting function, the dispersion and girth could potentially be sensitive to how jets interact with the hot and dense medium.

Jet Mass

One of the newly proposed jet observable is the jet mass. It is an attempt to measure the jet substructure and explore jet broadening inside the medium. Partons produced from the initial hard scattering lose their "off-shellness" or virtuality as they propagate. By measuring the jet mass one can probe the initial virtuality of the parton at the beginning of the shower and quantify the broadening of the jet profile in heavy ion collisions compared to the p+p

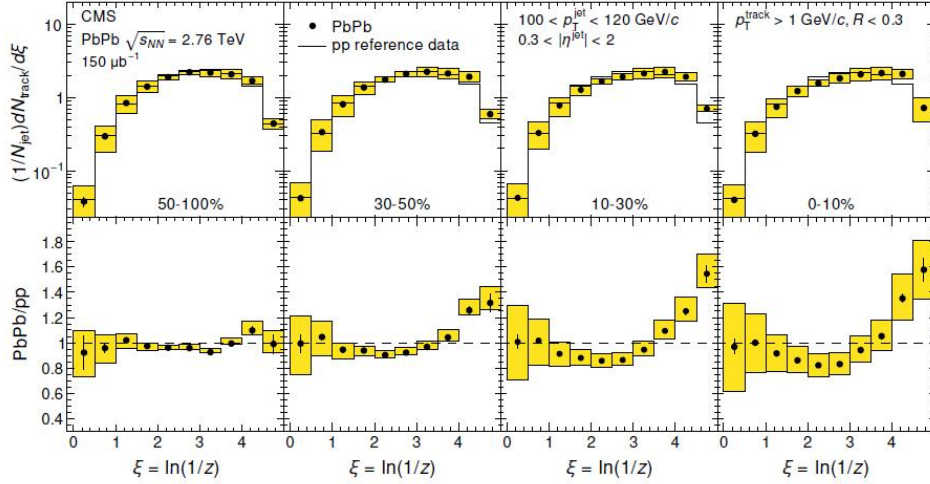


Figure 1.21: Fragmentation functions measured by CMS, for Pb+Pb compared to p+p collisions at $\sqrt{s} = 2.76$ TeV, with the Pb+Pb/p+p ratio in the lower panels, as a function of ξ , for various centrality selections.

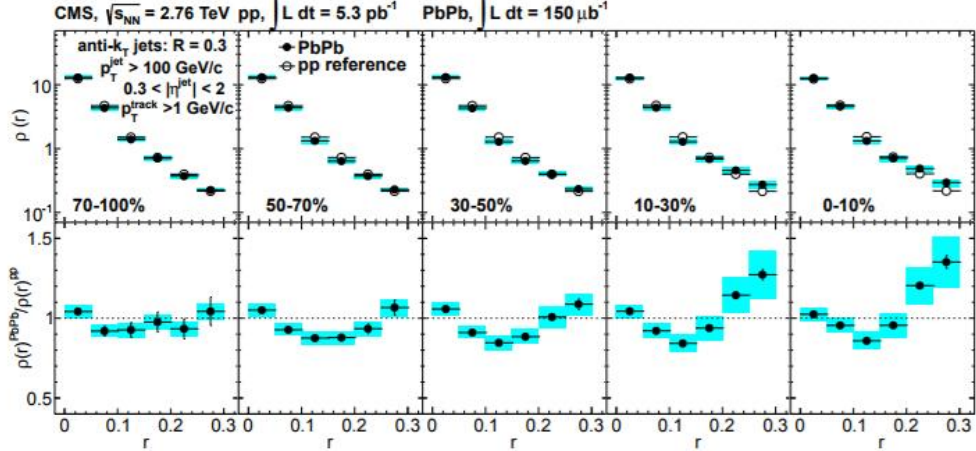


Figure 1.22: Differential jet shapes in Pb+Pb and p+p collisions in various centrality selections. The ratios have been normalized to unity.

case.

The ALICE experiment has recently reported a measurement of the mass of the reconstructed charged jets, with the jet mass definition given by the

following equation [27]:

$$M = \sqrt{E^2 - p_T^2 - p_z^2} \quad (1.15)$$

where E represents the jet energy, p_T is the jet transverse momentum and p_z the jet longitudinal momentum. They come from the four-momentum of the jet. The jet four-momentum is a sum of the four momenta of the jet constituents. Fig. 1.23 shows the resulting jet mass distributions for measured anti- k_T jets with size of $R = 0.4$ in 0-10% most central Pb-Pb collisions at $\sqrt{s_{NN}} = 2.76$ TeV. The calculations using JEWEL produce an underestimate of the jet mass when selecting "recoil off" and an overestimate with "recoil on". The mode with "recoil on" refers to the situation in which the scattering centers are registered and more soft particles produced. The good agreement between the data and PYTHIA simulation shows no modifications in Pb-Pb collisions given the current uncertainties, suggesting that the mass distribution for jets of $60 < p_T^{jet} < 120$ GeV/c is possibly insensitive to medium effects.

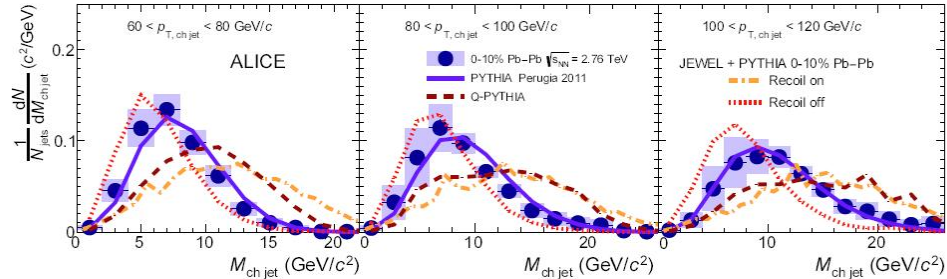


Figure 1.23: Jet mass distributions for anti- k_T jets with $R = 0.4$ for 0-10% most central Pb+Pb collisions, compared to JEWEL, PYTHIA and Q-PYTHIA calculations.

Splitting function

Advance in the recent jet algorithms attempts to remove soft radiation from the leading parton components of the jet. This is achieved by utilizing Jet Grooming algorithms [29, 30, 31, 32, 33].

The splitting function is constructed to measure the first/hardest splitting in a jet and is defined as the following:

$$z_g = \frac{p_{T2}}{p_{T1} + p_{T2}} \quad (1.16)$$

where p_{T2} denotes the transverse momentum of the least energetic subjet and p_{T1} the most.

Fig. 1.24 shows the ratios of z_g distributions in Pb+Pb and p+p collisions in different centrality bins for jets within 160 - 180 GeV. Modification for most central collisions is observed, indicating that the splitting into two branches is more unbalanced in Pb+Pb central collisions. However no modification is observed in the z_g measurement studied by the STAR experiment at $\sqrt{s_{NN}} = 200$ GeV [34]. Further investigation is needed for understanding and interpreting the current results and whether specific experimental requirements contribute to the difference we see between LHC and RHIC results.

Another new observable called the jet girth was also proposed and measured and the result indicates that the hard component of the jet gets narrower.

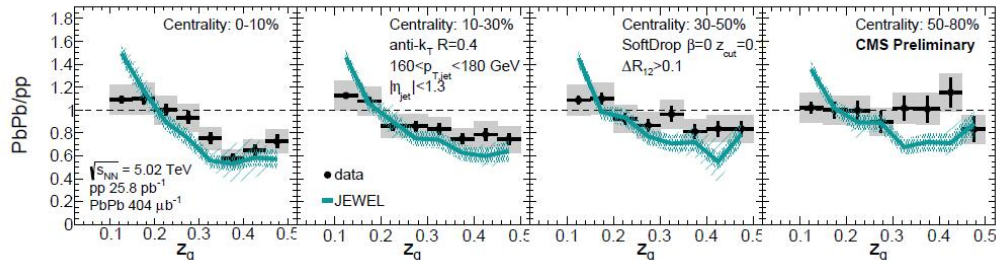


Figure 1.24: Ratios of splitting function in Pb+Pb and p+p collisions for jets with $160 < p_{T,jet} < 180$ GeV/c in different centrality bins.

The recent measurements using new jet observables suggest many interesting handles on the study of jet substructure tomography. They are powerful tools to investigate the medium effects on the propagating jet and sensitive to the structure and properties of jets. However these are still preliminary results and we need to understand their sensitivity to the effects of analysis cuts and background subtraction. Further understanding is required in model comparisons and so is more careful physics interpretation.

As one of the mature jet observables, jet fragmentation function has been measured and published before. It measures the distribution of the final state hadrons, that are fragmented from partons produced in the initial hard scattering. The analysis presented in this dissertation is an extended measurement to quantify the jet fragmentation function modification in Au+Au collisions, aiming to take a more clear picture of the jet-medium interactions and energy loss and redistribution.

1.6.3 Recent Theory Work on Energy Loss

For the past decades, there has considerable efforts in theory to understand the observed jet quenching and parton in-medium energy loss mechanism. The jet loses energy via elastic and inelastic collisions with the constituents of the medium. Generally there are two types of energy loss channels: collisional and radiative.

Fig. 1.25 shows the average energy loss calculated for partons produced at the center of the created nuclear medium in central heavy-ion collisions. The left plot is for a light quark passing through QGP at RHIC while the right plot illustrates the energy loss a bottom quark suffers inside the medium created at LHC collision energy. The energy loss of a light flavored parton with high enough initial energy is mostly dominated by radiative component. On the other hand, heavy quarks lose more energy through elastic or collisional interactions at low and intermediate energy ranges before the radiative contribution becomes more significant. The dead-cone effect [13] is the reduced gluon radiation phase space caused by large finite masses of heavy quarks, which explains the leading effect of collisional energy loss.

The Linear Boltzmann Transport Model

An important parameter characterizing how a jet propagates and interacts with the hot and dense medium is called the jet transport parameter \hat{q} . It is defined as the average transverse momentum broadening squared per unit length, along its propagation in the medium [15, 16]:

$$\hat{q} = \frac{\langle p_{\perp}^2 \rangle_L}{L} \quad (1.17)$$

where $\langle \cdots \rangle_L$ represents an event average over the propagation length L . \hat{q} is one of the parameters that describes the intrinsic properties of the medium,

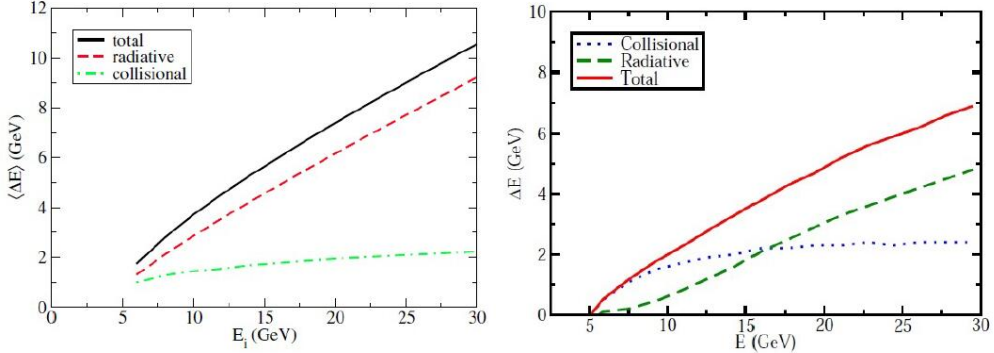


Figure 1.25: Left: Energy loss for a light quark produced in 0-5% most central collisions at RHIC. Right: Energy loss for a bottom quark in 0-7.5% most central collisions at LHC.

a measure of the p_T kick the medium gives to the traversing parton. Careful study and extraction of \hat{q} is essential in understanding how partons lose energy and experience transverse momentum broadening as they passing through while interacting with the medium.

The Linear Boltzmann Transport (LBT) model is a framework which includes a kinematic description of the parton propagation and the medium evolution via hydrodynamics. In this model, the complete set of $2 \rightarrow 2$ scattering processes are calculated by evaluating the local scattering rates between jet partons and thermal partons in a medium that evolves according to relativistic hydrodynamic equations. After each parton-medium scattering event, the model keeps track of the medium recoil parton as well as the jet shower parton, without taking into account further interactions among them.

According to the LBT model [19, 22], jet transport and propagation can be described by a linear Boltzmann equation:

$$p_a \cdot \partial f_a = \gamma_b \int \prod_{i=b,c,d} d[p_i] (f_c f_d - f_a f_b) |M_{ab \rightarrow cd}|^2 \times S_2(s, t, u) (2\pi)^4 \delta^4(p_a + p_b - p_c - p_d) + \text{inelastic} \quad (1.18)$$

where the first term is the explicit elastic scattering process. $d[p_i] = \frac{d^3 p_i}{2E_i(2\pi)^3}$. γ_b stands for the spin-color degeneracy of parton b. f_i are the parton phase-space distributions. For thermal partons inside the medium with local tem-

perature T and fluid velocity $u = (1, \vec{v})/\sqrt{1 - \vec{v}^2}$, the parton distributions are:

$$f_{i=b,d} = \frac{1}{e^{p_i \cdot u/T} \pm 1} \quad (1.19)$$

The "±" corresponds to the Fermi-Dirac distribution for quarks and anti-quarks and Bose-Einstein distribution for gluons, respectively. For jet shower partons before and after the scattering, their phase-space density are expressed as the following:

$$f_{i=a,c} = (2\pi)^3 \delta^3(\vec{p} - \vec{p}_i) \delta^3(\vec{x} - \vec{x}_i - \vec{v}_i t) \quad (1.20)$$

The matrix elements $|M_{ab \rightarrow cd}|^2$ represent the elastic scattering amplitude and the term $S_2(s, t, u)$ is introduced to regulate the collinear divergence in the leading-order by introducing a screening mass for light quarks and gluons in the matrix elements for two-parton scattering [19]:

$$S_2(s, t, u) = \theta(s \geq 2\mu_D^2) \theta(-s + \mu_D^2 \leq t \leq -\mu_D^2) \quad (1.21)$$

where μ_D is the Debye screening mass and the below relation holds with N_c being the number of color charges and N_f the number of quark flavors:

$$\mu_D^2 = \frac{g^2 T^2}{3} \left(N_c + \frac{N_f}{2} \right) \quad (1.22)$$

Considering for example one particular $2 \rightarrow 2$ elastic scattering process $a + b \rightarrow c + d$, we denote the more energetic out-going parton as the leading parton, and the other the thermal recoil parton. Both of them are recorded along with their information when undergoing further propagation through parton-medium scatterings. The participant parton b , which originates from the medium, is also registered in the scattering process. It is treated as a "negative" parton to account for the back-reaction in the Boltzmann transport equation. It is also allowed to transport and interact further and needs to be subtracted from the final parton spectra. Jet-induced medium partons are defined as contributions from the thermal recoil partons and "negative" partons [19].

Energy and momentum are conserved at each scattering, meaning that the energy loss of the propagating jet shower parton should be accounted for by the thermal recoil and the "negative" parton. Therefore this should reflect in the form of the jet-induced medium response in the final observables.

Fig. 1.26 illustrates the energy distributions of partons at different times for a propagating gluon with initial energy of $E_0 = 100$ GeV in a medium with temperature $T = 0.4$ GeV. Note that the simulated partons include leading jet shower partons as well as the jet-medium partons (thermal recoils with "negative" partons subtracted out). The black solid line represents the energy spectra at an early time $t = 2$ fm/c, the peak at around the gluon initial energy of 100 GeV comes from the leading parton, while the peak at small energy results from the jet-induced medium partons at the thermal energy. As the jet propagation continues, the leading shower parton loses more and more energy, softening the peak at larger energy value. Meanwhile, the abundance of thermal recoils (minus the "negative" partons) becomes more significant and shows up as the increasing peak magnitude at the small energy scale.

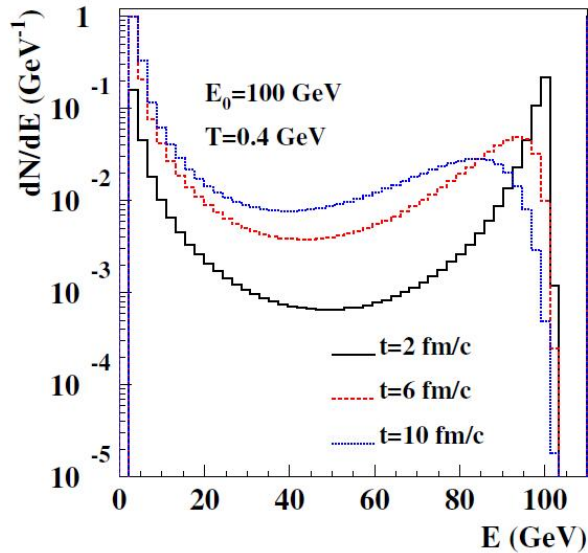


Figure 1.26: Energy distributions for leading partons and medium partons at different times for a gluon with initial energy $E = 100$ GeV propagating in the medium with temperature $T = 0.4$ GeV.

One interesting feature accompanying the jet-induced response manifests itself in a special form of parton energy distributions. Fig. 1.27 shows a 3D visualization of the energy density distribution of a propagating gluon with

initial energy $E_0 = 100$ GeV, traveling along the z direction in a uniform medium with temperature $T = 0.4$ GeV. The upper panel (a) and lower panel (b) are the distributions after 4 fm/c and 8 fm/c of propagation respectively. The leading jet shower parton starts to propagate and interact with the medium at the coordinate $z = 0$ and $r = 0$. It does not travel along a fixed direction. Instead, the momentum kicks and energy transfer from different directions develop a transverse momentum broadening for the leading parton along its propagation path. One sees in Fig. 1.27 that a Mach-cone like shock wave is formed and evolves as the leading parton propagates. A diffusion wake generated by the jet-medium interaction actually exhausts the parton energy density in the opposing direction with respect to the traveling leading parton.

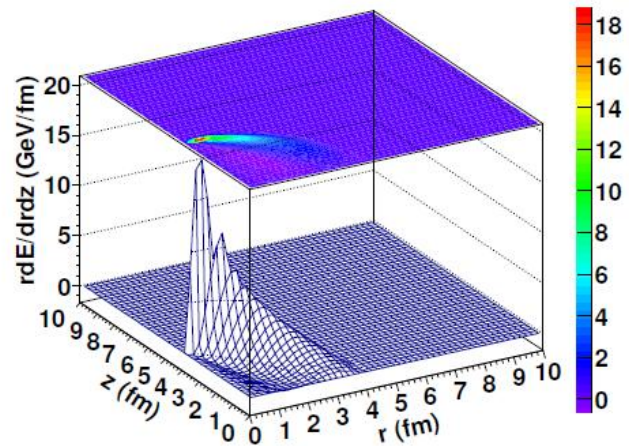
Fig. 1.28 shows the angular distributions of medium partons consist of thermal recoils and "negative" partons generated in the process of a 100 GeV gluon propagating in a medium of constant temperature of $T = 0.4$ GeV, at different times. For medium partons with low energy ($0 < E < 1$ GeV), they are mostly "negative" partons bounced back by the leading jet shower partons. For less soft medium partons, contribution from thermal recoils become more important and the dominance of "negative" partons diminishes with time, along the propagation direction. The double peaks seen in the parton energy ranges of 1-1.25 and 1.5-1.75 GeV are the effect of including contributions from soft medium recoil partons at large angle with respect to the propagation direction of the leading partons. This phenomenon goes away with time because of the diffusion of thermal recoils as well as the transverse momentum broadening of the leading partons, an outcome of multiple scatterings [19].

In a realistic pQCD picture of the parton evolution, the interactions between the jet showers parton and the thermal medium partons are mainly from the small angle scattering processes and gluon bremsstrahlung. The inelastic scattering term in Eq. 1.18 adds the contribution from the induced gluon radiation following each elastic scattering. Contribution from this induced gluon spectrum is produced in the simulation using the higher-twist approach [23, 24]:

$$\frac{dN_g^a}{dz dk_\perp^2 d\tau} = \frac{6\alpha_s P_a(z) k_\perp^4}{\pi(k_\perp^2 + z^2 m^2)^4} \frac{p \cdot u}{p_0} \hat{q}_a(x) \sin^2\left(\frac{\tau - \tau_i}{2\tau_f}\right) \quad (1.23)$$

where k_\perp is the transverse momentum of the induced gluon, which carries an energy fraction z of the parton it originates from. $P(z)$ is the splitting

(a) $t=4 \text{ fm}/c$



(b) $t=8 \text{ fm}/c$

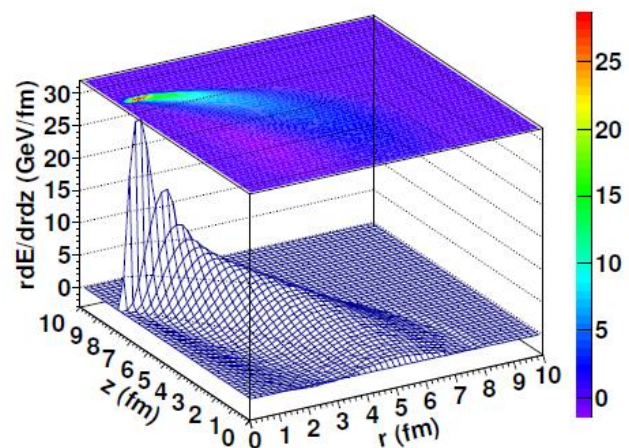


Figure 1.27: Energy density distribution showing for simulated medium response from a gluon of initial energy $E_0 = 100 \text{ GeV}$ and propagate along z and r directions after 4 and $8 \text{ fm}/c$, inside a quark-gluon plasma with temperature of $T = 0.4 \text{ GeV}$.

function that describes the probability of producing a gluon with such energy fraction z . m denotes the propagating parton mass. τ_f corresponds to the gluon formation time:

$$\tau_f = \frac{2p_0 z(1-z)}{k_\perp^2 + z^2 m^2} \quad (1.24)$$

Therefore the final partons after each scattering include jet shower partons, thermal recoils, induced gluons and the "negative" partons.

Recent progress couples the transport part of the simulation framework with a 3+1 dimension hydrodynamic model and is successful in predicting $\gamma - hadron$ correlations [22]. More discussion will follow in chapter 5.

JEWEL

JEWEL is a Monte Carlo event generator for simulating jet evolution in QGP in heavy-ion collisions in a perturbative approach with very few assumptions. In JEWEL, the medium that interacts with the jet is made of a set of partons. The scattering of hard partons inside the medium is described by $2 \rightarrow 2$ pQCD matrix elements with parton showers including effect from additional radiation [70]. Detailed introduction of JEWEL can be found in Ref. [70, 71, 72, 73].

Incorporating the most recent work on the JEWEL event generator, there are in total three switches for setting the medium response [73]:

- do not include the medium response
- extract a source term in order to apply a hydrodynamic approach
- register thermal recoils in the event and let them hadronize with the jet

The two options when generating JEWEL events are referred to as the "recoils on" and "recoils off", as we have seen in the labels in some figures in the previous text, when showing data comparisons to JEWEL calculations. These two modes are related to the treatment of the background partons when they interact and recoil against a scattering with the jet. The two modes correspond to the scenario of generating events with or without saving the recoil information. One could easily understand that the OFF mode is

related to the picture in which no medium response is involved. According to Ref. [71, 73], this is the recommended mode when simulating events to study inclusive jet observables such as dijet or γ -jet momentum imbalance. However for jet substructure observables, they are sensitive to jet-induced medium response and therefore it is necessary to include the effect of recoiling partons in the event.

There are two components for the four-momentum of the recoiling partons: the thermal momentum it carries before interacting with the jet, as well as the momentum the jet transferred to it after the scattering. The former corresponding to a source of the background, is stored and needs to be subtracted from the simulated jets. The medium response is included, on the other hand, by considering the second component. The subtraction of the thermal component is essential for producing comparable and reliable simulation JEWEL results to jet substructure observables measured in experiments. Details on the two methods, 4MomSub and GridSub, for such background subtraction can be found in Ref. [73].

Fig. 1.29 shows the ratio of the jet fragmentation function in Pb+Pb and p+p collision as a function of ξ measured in CMS (left) and as a function of p_T^{track} measured by ATLAS. The modification of the jet FF is observed to be the enhancement at high ξ and low p_T^{track} and a depletion in the intermediate regions. The JEWEL calculations in which includes the recoils and without are also shown as comparisons. Note that JEWEL is unable to do subtraction for individual tracks and all tracks are included in the fragmentation function, which inevitably manifests as an overshoot over the data at large ξ region, although the medium response has been taken into account. However the curve labeled without recoils is significantly suppressed as compared to data, suggesting that the observed enhancement of the soft particles are indeed due to jet-induced medium effect.

1.7 γ_{dir} -h correlations

Direct photon-hadron correlations is regarded as a golden channel to study parton in-medium energy loss in QGP. Firstly, as discussed in the previous text, photons, as color-neutral objects, do not interact via strong force with the created medium. Such measurement therefore does not carry a trigger surface bias compared to di-hadron correlations or reconstructed jet measurements, in which the hadrons or jets are biased to be coming from the

surface of the medium. Secondly, the yield of direct photons at high p_T is dominated by hard processes. High momentum direct photons are produced back-to-back with partons at leading order in the initial hard scatterings via predominantly QCD Compton scatterings. Their measured momentum will approximately balance those of the opposing partons before any medium modification. Consequently, using high-momentum direct photons as triggers is a most direct measure of the initial parton energy.

1.8 Statement of Purpose

As will be discussed in more details in chapter 5, the previous analysis, published in [74], showed that there is an enhancement in soft jet fragments at large angle. The statistical uncertainties were such that it was not possible to investigate how the fragmentation function depends on trigger p_T or associated particle p_T . In this analysis, we would like to add more statistics and split the 5-9 GeV/c trigger p_T bin in order to investigate the following questions.

- Does the enhanced production of soft fragments change with photon trigger p_T (i.e. does it depend on the parton p_T ?)
- Does the enhancement over the fragmentation function in p+p collisions depend on the fragment z or does it depend on the fragment p_T ? (i.e. does it depend on the jet structure or does it reflect the distribution of particles in the medium?)
- Does the angular distribution of the enhancement change for different p_T partons?

By including the statistics of $\gamma_{dir} - h$ correlations in Au+Au from analyzing the 2011 data, it is possible to answer the listed questions.

This analysis began by developing a completely new analysis code, rather than reusing the code which was used before. Previous analyses built on the code written initially for the $\gamma - h$ analysis in p+p collisions, which was Matt Nguyen's PhD work. The old code had contributions from multiple people over many years, becoming difficult to read. As this makes it tricky to debug any changes, the decision was made to write a new code which would be more streamlined and documented in a consistent fashion.

There has been extensive effort and time devoted to setting the analysis framework and ensuring it is robust to run. Everything related to this analysis was written from scratch including all base classes, EMCAL hot tower exclusions, event mixing set-up and so on. Most of the macros are also original and tested. The code package is then used for analyzing the d+Au $\gamma_{dir} - h$ correlations analysis which was conducted later and in parallel. Although not the subject of this dissertation, there will be a brief discussion on the d+Au result presented in 5.4.4. The investigation of possible cold nuclear matter effect in d+Au collisions are compared with the observed hot nuclear matter effect in Au+Au result.

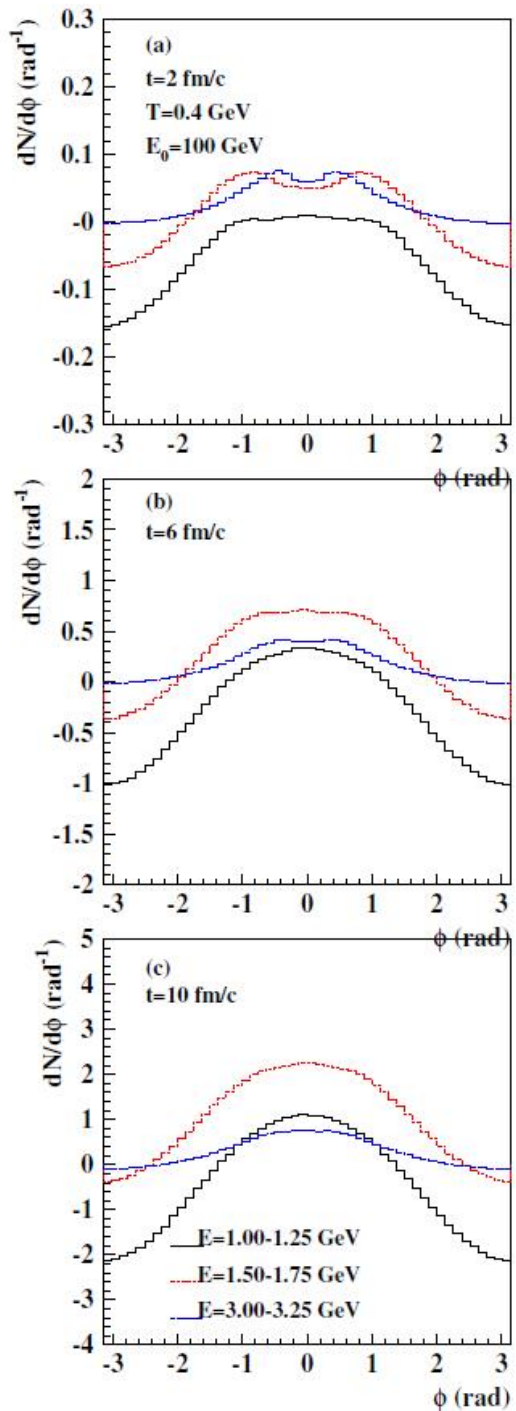


Figure 1.28: Angular distributions of medium partons with different energies, induced by a gluon with an initial energy $E = 100 \text{ GeV}$, propagating at different times of propagation, inside a QGP with temperature of $T = 0.4 \text{ GeV}$.

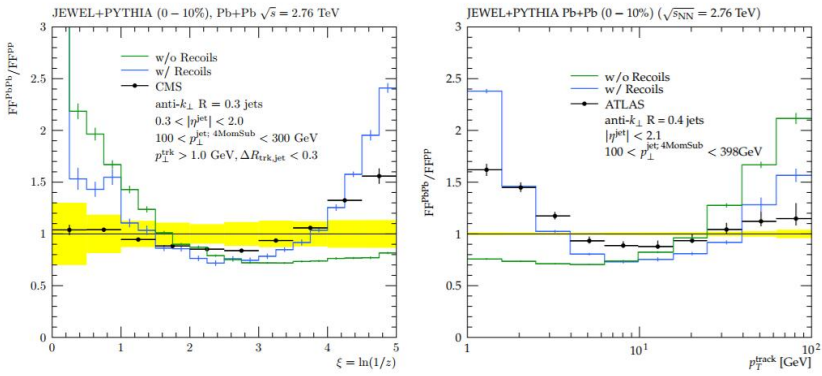


Figure 1.29: Ratios of jet fragmentation function in Pb+Pb to p+p collisions for anti- k_T jets with cone size $R = 0.3$, measured by CMS as a function of ξ , shown on the left and the ATLAS data as a function of p_T^{track} , shown on the right. Comparisons with JEWEL simulations are shown in green lines representing no recoils included and blue lines denoting with recoils.

Chapter 2

Experimental Setup

In this Chapter, we present a description of the experimental facilities and apparatus that are relevant for the analysis discussed in this dissertation.

A general overview of the RHIC program and the PHENIX experiment is described in section 2.1 and 2.2. Event triggering and data acquisition process is included in section 2.2.1.

The prime detectors that are used in this analysis are the following: The beam beam counter and zero degree calorimeter described in section 2.2.2 are for event characterization including collision vertex position and centrality determination. The drift chamber and pad chambers are used for particle tracking reconstruction. See section 2.2.3 for details. The ring imaging cherenkov detector is used for electron identification and for this analysis to remove electron contamination in the hadron sample. The electromagnetic calorimeter (section 2.2.4) is essential for this analysis in terms of photon identification and π^0 reconstruction. It is also used for track matching in order to reduce fake tracks. The vertex detector was newly installed for the run in 2011 but was not used as its performance and active areas were too low for this statistics-hungry analysis. Nevertheless a brief introduction is included in section 2.2.5.

2.1 RHIC

The Relativistic Heavy Ion Collider (RHIC) is a two-ring superconducting hadron collider, located at Brookhaven National Laboratory. It is one of the largest research facilities for nuclear physics program of US Department of Energy [44]. RHIC operates as an accelerator, a storage ring, and a collider for a variety of particle species, providing collisions for heavy ion and spin research [43]. The heavy ion program investigates the properties of QGP, while the spin program studies the origin of the proton spin. The design energy for heavy ion beams is 100 GeV per nucleon per beam and 250 GeV for proton beams.

Figure 2.1 shows the steps of heavy ion beams being accelerated in the RHIC. Negatively charged ions start their journey from the Tandem Van de Graaff accelerator. The ions are accelerated and stripped of some electrons upon exiting the Tandem. They are further stripped to a new charge state when exiting the Van de Graaff and travel to the Booster synchrotron through a heavy ion transfer line. A stripping foil at the Booster exit removes all atomic electrons except for two tightly bound K-shell electrons [43]. The gold ions are now at a much higher velocity and enter the Alternating Gradient Synchrotron (AGS), where they are accelerated to 99.7% speed of light and completely stripped before being injected into the RHIC rings, at a constant frequency of 78kHz, denoted as f_{rev} . Here we define luminosity as:

$$L = \frac{b}{4} \frac{N^2}{\sigma_x \sigma_y} f_{rev} \quad (2.1)$$

where b is the number of bunches per ring and can be as large as 128 by the RHIC design. N is the number of particles per bunch: 2×10^{11} for p+p collisions and 10^9 for Au+Au collisions. σ_x and σ_y are the cross sections of the bunches: 2×10^{32} and $2 \times 10^{26} \text{ cm}^{-2} \text{ s}^{-2}$, respectively.

The ions circle around the ring of about 3.8 km in circumference in counter directions. They are referred to as the "blue ring" which travels clockwise and the "yellow ring" that travels counter-clockwise. The two beams intersect at six positions spaced at equal distance around the ring. Four out of the six interaction points house four experiments: BRAHMS, PHOBOS, PHENIX and STAR. BRAHMS and PHOBOS completed their data taking tasks and physics goals in 2006. After taking a last year of data in 2016, PHENIX has ended data taking, with considerable amount of analyses effort still going on. The work presented in this dissertation is based on an analysis of Au+Au

collisions at a center-of-mass energy of 200 GeV, collected in 2011. This data set corresponds to an integrated luminosity of 4.97 nb^{-1} .

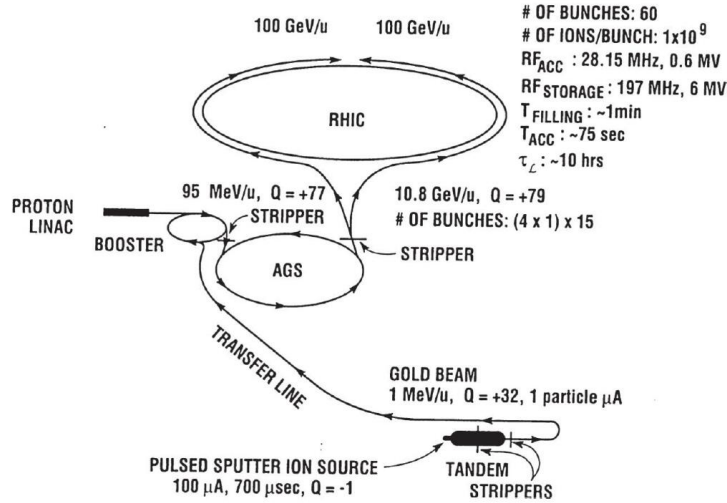


Figure 2.1: A schematic drawing of RHIC facility, demonstrating the process of colliding Au ion beams. The Au ions are accelerated and stripped step by step from Tandem Van de Graaff, Booster and then AGS before injection into the RHIC ring in counter-rotating directions and collide head-on at different crossings.

2.2 PHENIX

PHENIX, or the Pioneering High Energy Nuclear Interaction eXperiment, is located at the eight o'clock position with respect to the center of the RHIC ring. The conventional PHENIX coordinates are illustrated in Figure 2.2. z axis represents the clock-wise rotating beam direction, defining "north" pointing at the direction where polar angle $\theta = 0$ and "south" the opposite. y axis is pointing upwards and the direction of x axis is determined by $\vec{x} = \vec{y} \times \vec{z}$.

We can define pseudorapidity as:

$$\eta = -\ln \left(\tan \frac{\theta}{2} \right) \quad (2.2)$$

Forward/background directions have large $|\eta|$, while mid-rapidity refers to regions with small $|\eta|$. PHENIX consists of four spectrometer arms made of multiple detectors, excelling in measuring leptons and photons that serve as direct probes of the QGP. Figure 2.3a shows the beam view of the whole setup. Two spectrometers cover an azimuthal angle of 90° on each side and pseudo-rapidity range of $|\eta| < 0.35$, therefore are referred to as the "central arms" - west/east arm depending on their position relative to the collision point. They function for charged particle tracking, pattern recognition and reconstruction, charged particle identification, photon and neutral pion detection etc. Figure 2.3b shows a complementary side view in which the detectors for forward tracking and calorimetry for measuring muons can be seen. They are noted as "the muon arms", covering full azimuth and a pseudorapidity range of $-2.2 < \eta < -1.2$ and $1.2 < \eta < 2.4$.

The following sections will include description of the detectors specifically relevant for this analysis.

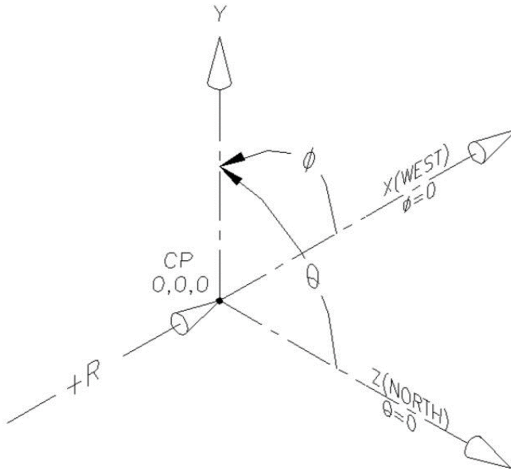
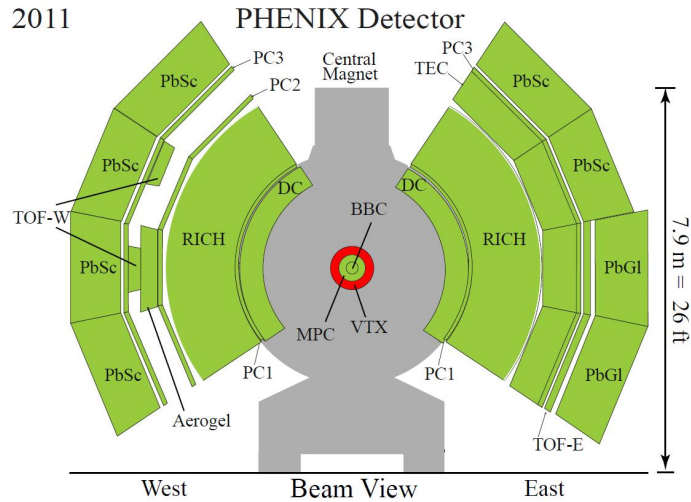
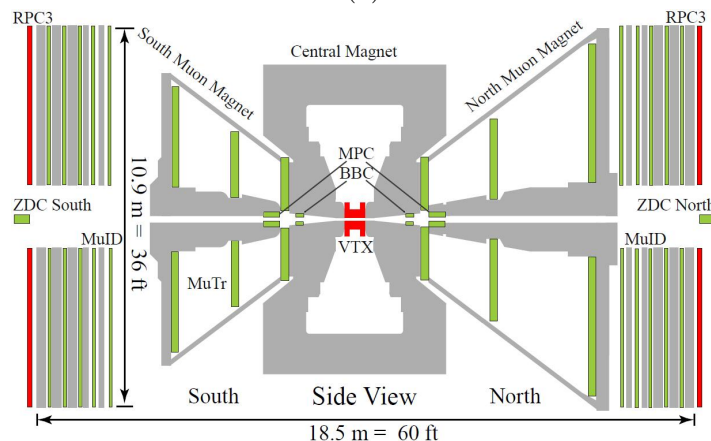


Figure 2.2: PHENIX coordinate system [45]. z axis is the beam direction along which reside the muon arms as well as event characterization detectors. The x-y plane is the azimuthal plane where the central spectrometers sit.



(a)



(b)

Figure 2.3: PHENIX detectors layout and positioning in 2011. A beam view showing mostly the central arm detectors is presented in (a). The forward detectors including the muon arms are displayed in the side view (b).

2.2.1 Triggering, data acquisition and event reconstruction

The PHENIX data acquisition system (DAQ) has a high rate capability. The data rate can reach as high as 1GB/sec by design. The PHENIX Front End Electronics modules (FEM) are synchronized to the 9.4 MHz RHIC clock, which corresponds to the time interval of 106 ns between beam crossings. Data are read out from each subsystems as analog signals to the FEMs. After being selected by the Level 1 trigger (LVL1) which filters out empty beam crossings and uninteresting events, they are digitized by the Front End Electronics (FEE) into event fragments and shipped from the interaction region to data collection modules (DCM) in the counting house via optical fiber links. There events are processed and undergo error checking, data compression and reformatting. The data streams are then reported to Sub-Event Buffers (SEB) in parallel and go through a set of Assembly and Trigger Processors (ATP). The event data is constantly under scrutiny through online monitoring system during the data taking period to guarantee quality. Performance plots for ensuring that each subsystem is functioning well update frequently. A physics run needs to be stopped if there are major issues such as large dead areas or electrical shorts to multiple wires, happening to particular detector(s). After passing the quality checks, the data are buffered in local disks and later transferred to storage tapes at the RHIC computing facility, before they are produced for physics analyses [46, 47].

The analysis presented in this dissertation uses minimum bias Au+Au data from 2011, selected by the minimum bias trigger which is defined as the coincidence of one or more phototubes being fired in the north and south beam-beam counters. Description of the detectors is in the next section 2.2.2.

2.2.2 Event characterization

To characterize the nature of an event from a PHENIX collision, "global" detectors are used to measure timing, location and particle multiplicity of a collision.

Beam Beam Counters

The Beam-Beam Counters (BBC) are two arrays of Cherenkov detectors, located at 1.44 meters from the center of the PHENIX interaction region

and surround the beam pipe, covering rapidity range of $3.0 < |\eta| < 3.9$ and full 2π azimuthal angle [54]. They are positioned on the north and south side of PHENIX, therefore are referred to as BBCN and BBCS, respectively. Each BBC is composed of 64 3 cm quartz Cherenkov radiators, each of which is attached to a mesh-dynode photomultiplier tube (PMT) to read out the Cherenkov light produced by particles when traversing the radiator. Figure 2.4 shows a photo of a single BBC element and combination of 64 elements into one BBC counter.

As it measures the count and arrival time of charged particles in heavy ion collisions where their density is high, the BBC is designed to be radiation hard and function in high multiplicity. It is also located in a high magnetic field environment. A high single-element timing resolution of 52 ± 4 ps empowers the BBC to trigger the data acquisition system, also to precisely measure the start time of the time-of-flight (TOF) system, allowing good charged hadron identification.

The BBC provides the time of interaction and the position of a collision, which is crucial to characterize an event. If we denote T_N and T_S as the time it takes before a hit signal is recorded, averaging over all elements for the north and south counters correspondingly, the collision time is defined as

$$T_0 = \frac{T_N + T_S - 2L/c}{2} \quad (2.3)$$

where L is the distance between each BBC and the center of the interaction region. The collision point along the z axis is determined using coincidences between BBCN and BBCS:

$$z_{vertex} = \frac{T_S - T_N}{2}c \quad (2.4)$$

The BBC delivers the vertex information to the level 1 trigger. An event is written if the collision takes place within $|z_{vertex}| < 30$ cm and at least one PMT is fired in each BBC.

The BBC can also be used to determine the event plane of a collision, which is critical for the elliptic flow measurement. Furthermore, the centrality determination can be achieved using the total charge deposition information in the BBC, as will be described in more details in the following sections.

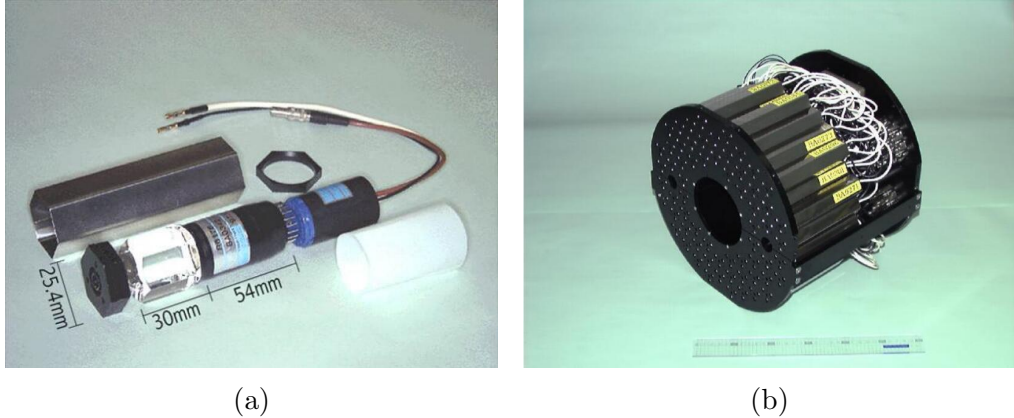


Figure 2.4: A picture showing (a) dimensions of a single BBC Cherenkov counter composed of a quartz radiator and PMT readout. (b) one BBC module: made of 64 BBC elements integrated in a honeycomb fashion.

Zero Degree Calorimeter

The Zero-Degree Calorimeters (ZDC) are a pair of hadron calorimeters installed along the beam line, at about 18 meters from the PHENIX interaction point, with an angular acceptance of $|\theta| < 2$ mrad. They stand behind the two dipole magnets on both north and south side of PHENIX, shown in Fig. 2.5. The detector is made of tungsten and the signals it collects are read out through PMTs. During heavy ion collisions, not all nucleons from the two colliding nuclei participate in the actual collision. Those that do not participate are referred to as the spectator nucleons. Most charged particles being deflected away by the magnets, the ZDC can measure at very forward rapidity with little background the energy deposited by the spectator neutrons from the collisions. The main purpose of building the ZDC is to determine collision centrality by detecting forward neutrons and their deposited energy. In PHENIX, the ZDC is often used to perform complimentary yet independent measurement to the BBC event characterization. The neutron signal coincidences in the north and south sides are used to determine the time and position of the collision, yielding a z vertex position resolution of 2.5 cm and a timing resolution of 100 ps. The ZDC can also be used as an event trigger and a luminosity monitor [55].

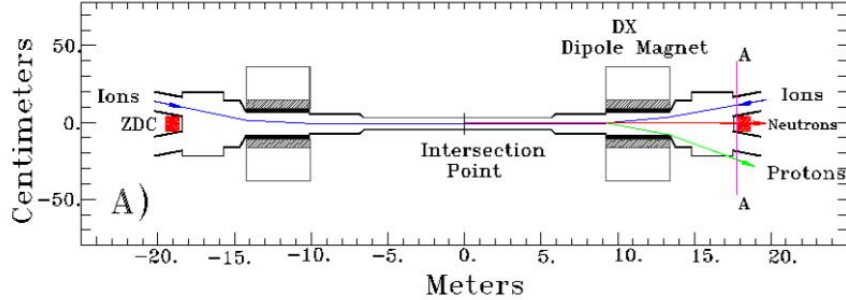


Figure 2.5: Position of the zero degree counters [55].

Centrality Determination

In chapter 1, we introduce the concepts of centrality and impact parameter. Experimentally, for a given collision, one can determine centrality by relating the impact parameter (b), number of participants (N_{part}) and number of binary collisions (N_{coll}) to the produced particle multiplicity. Small impact parameter b , corresponding to more particle yield at the mid-rapidity and fewer of spectator nucleons at the beam rapidity. Such events are referred to as central events. On the other hand, a less central (peripheral) event is defined as an event with large impact parameter and little multiplicity at mid-rapidity and more spectator nucleons in large rapidity region are expected.

There are two primary ways to determine centrality classes in PHENIX. "The clock method" correlates the total charge deposited in the BBC and the integrated energy in the ZDC [61]. As described above, the ZDC measures spectator neutrons that are no longer bound in deuteron or heavier nuclei, while the BBC measures the number of charged particles at forward rapidity. In mid-central collisions, many protons and neutrons are dissolved from their bound states, so the number of neutrons "freed" from the collisions is large, leaving a large response in the ZDC. For peripheral collisions, few spectator neutrons emerge in the forward direction due to a lack of breakup of the spectators. In the most central collisions, the ZDC also collects little signal. This is because very few neutrons are freed from the collisions, as most nucleons collide. Given that the charge collected in the BBC is monotonically related to the initial collision impact parameter, centrality classes are determined then by dividing the collected events normalizing the BBC and ZDC response [82]. The left plot in Fig. 2.6 demonstrates the correlation

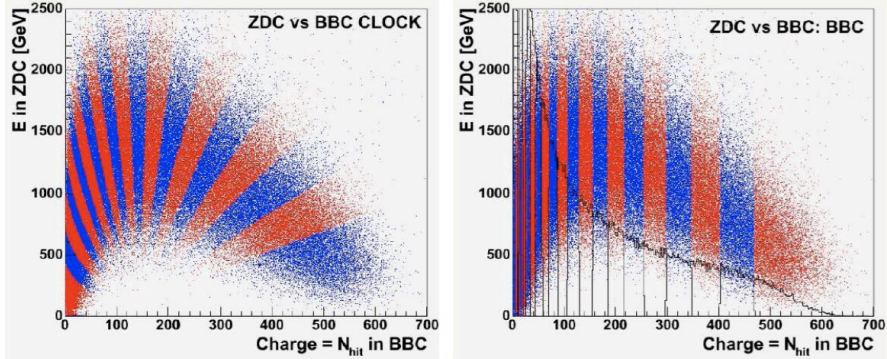


Figure 2.6: Centrality determination by correlating the neutron energy detected in the ZDC as a function of number of charged hits measured in the BBC. Slicing collected events into centrality bins using the clock method (left) and the BBC-only method (right) [62].

between the fractional charge collected by the BBC and the fractional energy measured in the ZDC. Centralities are divided in steps of 5%. "Clock" in the name of this method refers to the resemblance between this radial shaped division and an actual clock face.

The plot on the right in Fig. 2.6 shows how to use the BBC information exclusively to determine centrality classes, known as the "BBC only method". The BBC charge distribution is divided into percentiles. Similar to the left plot, alternating red and blue colors are used to distinguish different centrality classes into intervals of 5%. The most central collisions are defined using the band on the right side, corresponding to the largest N_{part} and N_{coll} and $b \rightarrow 0$. In practice, this "BBC only" method has replaced the "clock method" in PHENIX in recent years, as it has been studied and proven to be a more precise measurement to determine N_{coll} and N_{part} .

2.2.3 Tracking Detectors

Charged hadron reconstruction is performed using central arm tracking detectors: the drift chamber (DC) and the pad chambers (PC).

Drift Chambers

The Drift Chamber is a gas-filled chambers which has timing capability to measure the hit spatial position along readout wire. Generally such a detector

is filled with a gas mixture including noble gas; when a fast moving charged particle passes through, it ionizes the surrounding gas atoms. The induced electrons are separated from ions and accelerated by an electric field operated by the potential gradient between the anode and the cathode, causing a local cascade of ionization - or an "avalanche" - which amplifies the resulting signal that gets read out from the anode wires. The charges and their arrival time are collected at the nearest wire and the signals are proportional to the ionization magnitude. By analyzing signals from all wire charge collection can the particle trajectory can be determined. In PHENIX the carefully chosen gas mixture consists of 49% Ar, 49% C_2H_6 , and 1.5% ethanol.

The DC is located at 2 - 2.4 meters radially away from the beam axis on the west and east side of PHENIX coordinates, each arm covering 90° in azimuth. One can see from Fig. 2.3a that the two arms are placed not exactly back-to-back, making particle correlation measurement at angular difference $\Delta\phi \sim 180^\circ$ possible. In the beam direction, DC covers about 2 m along z axis. The DC is designed to measure charged particle trajectories in the $r - \phi$ plane to determine their transverse momentum and the invariant mass of particle pairs [63]. Another crucial role of the DC is in pattern recognition and associating tracks with other subsystems for particle identification. The track reconstruction algorithm will be explained in more detail in a later section.

Each DC is in a titanium frame that spans in azimuthal and beam directions. The gas volume is segmented into 20 sections with the same size, known as "keystones", each covering an azimuthal angle of 4.5°, shown in Fig. 2.7a. Inside one keystone module, there are six sets of wires that are placed along the radial direction: X1, U1, V1 and X2, U2, V2. The X1 and X2 wires are oriented in parallel to the z axis to perform measurement of track hit positions in (r, ϕ) coordinates. The U and V stereo wire planes are tilted slightly (6°) with respect to the X wire planes to pinpoint the track z position. A detailed demonstration of the design of the wire planes inside one DC cell is shown in Fig. 2.7b. The single wire resolution and efficiency are found to be 165 μm and 95%. To determine the track hit position, it is important to measure the drift velocity which can be calculated by finding the two calibration parameters: t_0 and t_f . t_0 is the ionization initial time. t_f is the time when the track gives a signal from distance d_{max} . d_{max} is the maximum distance a charge can travel from the wire. These two parameters can be determined from fitting the DC raw timing distributions, shown in Fig. 2.8 [80].

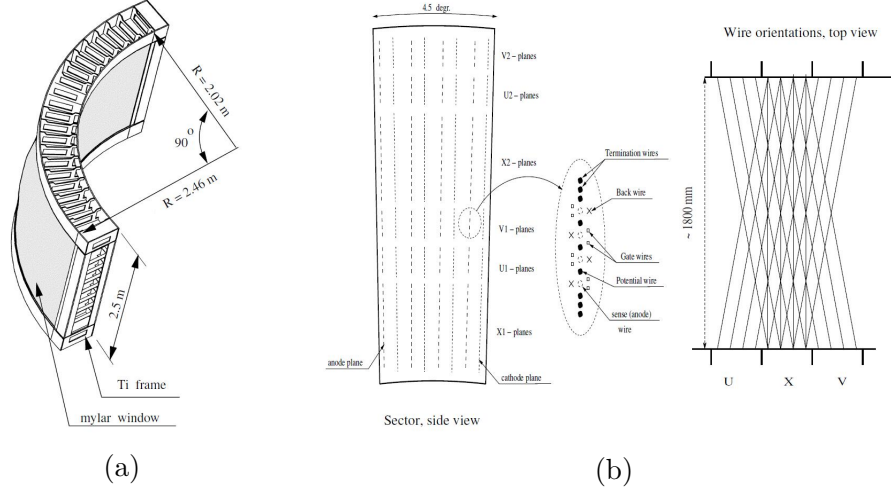


Figure 2.7: The drift chamber design: (a) A schematic display of one DC frame and its geometric characteristics and corresponding size measurement. (b) Left: a side view showing the stacked wire planes inside one drift chamber cell and inside the anode plane. Right: A top view demonstrating the orientation of X U V wire planes. [63]

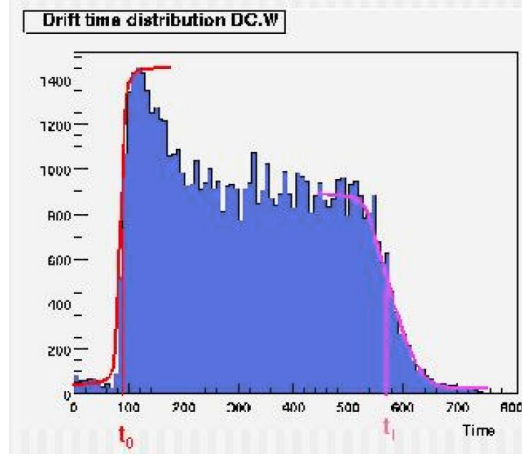


Figure 2.8: An example timing distribution of the drift chamber hits in the west arm. Calibration parameters t_0 and t_f are determined by fitting the edges of the distribution [80].

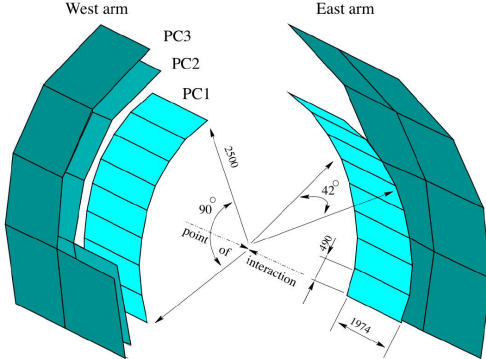


Figure 2.9: PC1, PC2 and PC3 positioning in PHENIX with a few sectors of PC2 and PC3 removed for viewing clarity [85].

Pad Chambers

The Pad Chamber (PC) system [63, 64] is a set of multiwire proportional chambers; there are three sets in PHENIX. The PC is non-projective, making it an important component to pattern recognition and track reconstruction. The innermost layer, PC1, at a distance of ~ 2.5 meters radially away from the collision point, is right behind the Drift Chamber and in front of the Ring Imaging Cherenkov Counters (RICH). It provides critical information for determining the three-dimensional space points and the z position of the charged track momentum vector from the DC with a resolution of 1.7 mm. Additionally PC2 and PC3 add more space coverage and function in removing secondary interactions and decays etc. PC2 resides behind RICH and is only available in the west arm. PC3 is placed in front of the Electromagnetic Calorimeter (EMCal) and like PC1 it covers both west and east wings. Fig. 2.9 is a clear way to view the PC system with a few sectors of PC2 and PC3 along with the rest of the PHENIX detectors removed from the picture.

Each pad chamber consists of one plane of anode and wires immersed in a gas volume contained inside two cathode layers. One cathode is plain copper and the other is segmented into arrays of pixels specially designed for optimizing the readout. As illustrated in the left diagram in Fig. 2.10, the pixels are linked in a staggered configuration, which minimize the number of readout channels while maximizing position resolution. A cell is defined as the three neighboring pixels which belong to three different readout channels, shown in the right diagram of Fig. 2.10. Therefore a hit in a cell is determined when all of the three pixels receive signals, drastically reducing the probability of finding a false hit caused by electrical noise.

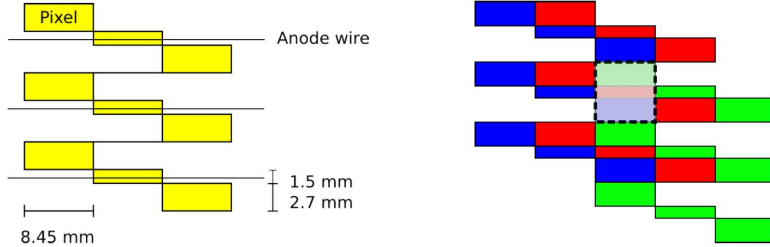


Figure 2.10: Left: a 9×9 pixel pattern that connects to one readout channel. Right: A demonstration of pad and pixel layout. Blue, red and green represent for 3 different 9×9 pixel arrangement. A cell is defined as the shaded box with dashed lines, which contains three pixels that are connected to different but neighboring readout pads [79].

Central arm track reconstruction

The PHENIX central arm magnet provides a magnetic field, allowing track momentum determination within an polar angle range of $70^\circ - 110^\circ$. It consists of two concentric coils and gives a non-uniform magnetic field parallel to the beam direction. The magnet can be operated in two modes: same or inverse polarities, corresponding to the "++" and "+-" fields. In the "++" configuration, an axial field of about 0.5 T is generated about 1 m radially from the beam. The magnetic field becomes very weak beyond the DC region by construction. The field strength is carefully designed. It is strong enough for carrying out the momentum measurement up to 10 GeV particles; but also chosen to be weak enough, so that charged particles with transverse momentum down to 150 MeV/c can travel to DC without being deflected away.

In PHENIX, the DC track reconstruction is performed using a combinatorial Hough transform (CHT) method. The CHT parameters that need to be determined are ϕ and α shown in Fig. 2.11. The circle defines the reference radius that corresponds to the radial distance between the collision vertex and the mid-point of one DC. ϕ is the polar angle of the crossing point of the track and the reference circle while α stands for the inclination. The CHT technique maps the hit information in X1 and X2 wire planes inside the DC module pair-by-pair into a space in (ϕ, α) . This determines the track trajectories in the $r - \phi$ plane. It is worth noting that an estimate of the

track momentum can be obtained assuming it is inversely proportional to the inclination angle α . The reconstructed DC track is characterized by its pointing direction: ϕ and α . The track reconstruction in the non-bend plane can be carried out by projecting the DC track to PC1. In addition, knowledge of the hits in the UV wire planes and that in the PC system provides further discrimination in the pattern recognition in (r, z) coordinates. The procedure involves several iterations which takes into account the PC1 hit association combinations.

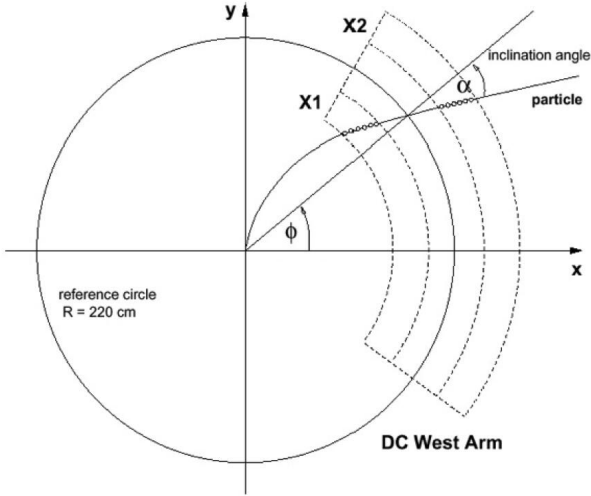


Figure 2.11: An illustration of the DC track reconstruction, including the combinatorial Hough Transform parameters ϕ and α [66]. The method is discussed in the text.

There are hierarchies among all the reconstructed tracks depending on how they are reassembled. Typically we assign a unique quality number to a particular set of charged tracks relating to the way they are determined. This quality parameter encodes the information of which DC wire planes are hit, whether they are unique and whether there is a PC1 hit associate with it and whether that is unique. The highest and second highest quality tracks come with the number 63 and 31, respectively, which is one of the track selection requirement used in this analysis. 63 is a signed to tracks that leave hits in both X1 and X2 planes, together with a unique UV and PC1 hits. 31 labels tracks that are found using hits in X1 and X2 layers, and a unique hit in UV plane and a non-unique hit in PC1. More details will be discussed in section

3.4.3.

Besides the track pattern recognition, the momentum reconstruction is essential for track reconstruction. Since the PHENIX central magnets have complicated and non-uniform field patterns, a precise analytical solution for track momentum determination is not possible. Instead look-up tables (LUT) are used.

A full GEANT simulation is conducted using different charged particle species. They are generated initially with a grid of possible values for their p_T , ϕ , polar angle θ and z-vertex position z_v . Detector geometry and acceptance, together with detailed numerical field maps are used during the simulation. As a result, a one-to-one correspondence for the output positions and pointing directions are generated and specified in terms of a set of kinematic variables: α , β , ϕ_{DC} and z_{pad} . α is the inclination angle between the DC track and the reference radius R_{DC} at 2.2 m. $\phi_{DC} = \phi_v + \Phi$, which is measured at the DC reference radius R_{DC} . z_{pad} is the z position measured in PC1. The initial and measured track parameters are shown in Fig. 2.12. This unique mapping is stored in the track model LUT, which gets referenced in the track reconstruction procedure. More detailed description of the track reconstruction method can be found in Ref. [65, 66]

2.2.4 Particle Identification Detectors

Electromagnetic calorimeters

Photon and π^0 measurements are important for this analysis, as they serve as triggers in constructing the two-particle correlations. They are measured using the PHENIX Electromagnetic calorimeter (EMCal) system [49].

Highly energetic electrons interact with materials and produce photons through bremsstrahlung radiation. Photons on the other hand, yield electrons and positrons via pair production when they pass through materials. The produced secondary photons and e^+e^- - carrying less energies than the parents - keep traveling and creating more and more photons and e^+e^- on their way by the same production mechanisms, resulting in a cascade of particles. This phenomenon is known as the electromagnetic shower process, depicted in Figure 2.13. The radiation length, X_0 , is the distance an electron travels before its energy reduces to $1/e$ of the original energy. X_0 is a common parameter used to characterize any material. The working principle of an electromagnetic calorimeter is to measure the particle's incident energy

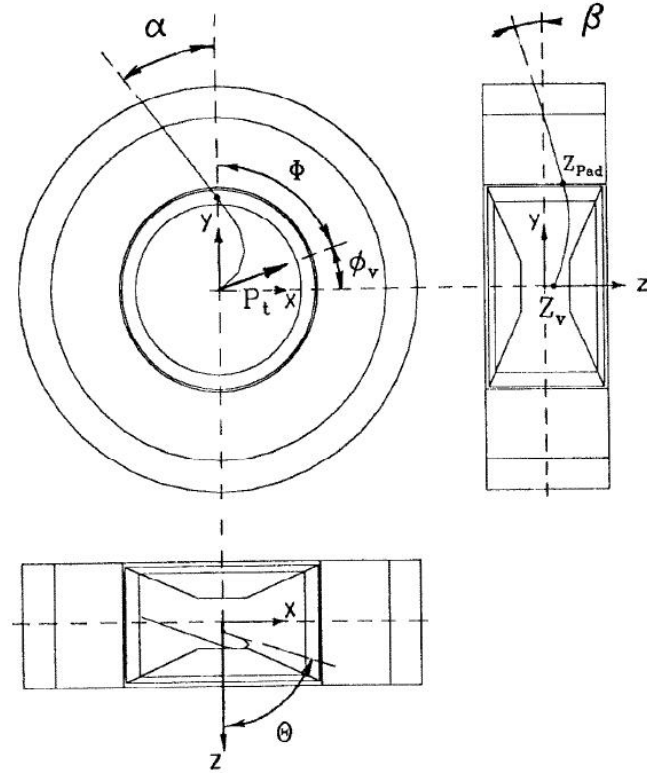


Figure 2.12: Illustration of the initial set of track parameters (p_T , ϕ , θ , z_v) and the measured set of parameters (α , β , ϕ_{DC} , z_{pad}). $\phi_{DC} = \phi_v + \Phi$, which is measured at the DC reference radius R_{DC} . z_{pad} is the z position measured in PC1.

based on the energy it deposits in the detector material. Information such as the shower shape and segmentation of the detector provides the hit position, and particle identification, as well. Typically one could express the EMCal energy resolution in the following fashion:

$$\frac{\sigma}{E} = \frac{a}{\sqrt{E}} \oplus \frac{b}{E} \oplus c \quad (2.5)$$

where the first term on the right-hand side of the equation stands for "the stochastic term" rising from intrinsic fluctuations of the shower development process. The second term is referred to as "the noise term" coming from electrical noise of the readout. The third constant term results from detector

specific effects such as the geometry, damage and so on, which do not depend on particle energy [51].

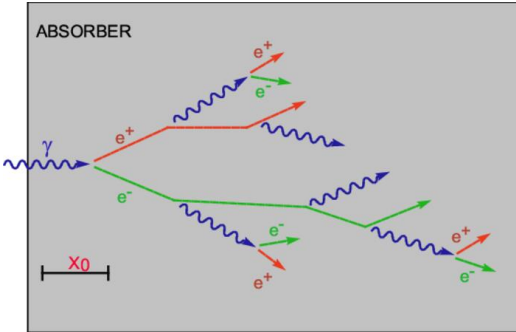


Figure 2.13: An electromagnetic shower induced inside a block of absorber material.

In PHENIX, the EMCAL is designed primarily for photon and electron identification and measuring their spatial positions as well as energy. It consists of two arms, each spanning the full central spectrometer acceptance of $70^\circ \leq \theta \leq 110^\circ$ and 90° in azimuth. It includes two types of detectors: six sectors of lead-scintillator (PbSc) sampling calorimeters - four of which sit on the west side and two on the east of central arm - and two lead-glass (PbGl) Cherenkov calorimeters occupying the east bottom half.

The PbSc is a shashlik type of calorimeter with alternating layers of lead and scintillator that accommodates entirely 15552 single towers. A tower is the finest segment for each PbSc sector and is read out independently. Four towers combine into one module, as shown in the left plot in Figure 2.14. 36 modules are grouped together to make a supermodule (SM) and 18 SMs combine into one sector. Light is produced when charged particles (electrons in the EM shower) pass through the scintillation material. The EMCAL is read out via wavelength shifting fibers into phototubes. The alternating nature of the lead and scintillator tiles allows the detector to collect a fraction of the total shower energy in each layer.

The PbGl has a different design from the PbSc. It is a Cherenkov calorimeter, a type of homogeneous calorimeters, containing 9216 modules in total. An array of 6×4 modules makes a supermodule (SM), which brings out 192 SM in one PbGl sector arranged in a way of 16×12 . Figure 2.15 is an illustration of one PbGl SM. Cherenkov light would be induced by the material when electrons and positrons travel through the material at

a speed faster than the speed of light. The Cherenkov light is collected and individually output to phototubes. Using this detector technology, hadron exclusion can be achieved by the fact that hadrons generally do not shower, or the fraction of energy they leave in the calorimeter is minimal (due to the small thickness compared to the hadronic interaction length). The PbGl only sees Cherenkov light, as a result the hadron response in the calorimeter is minimal.

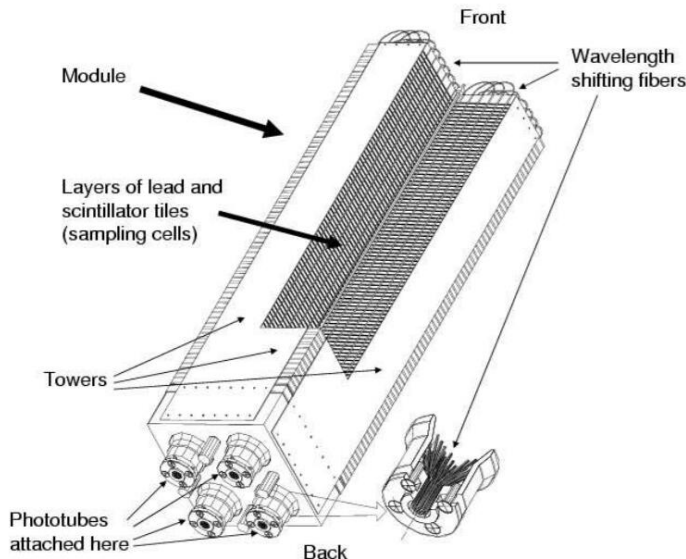


Figure 2.14: A cutaway view of one PbSc module.

Both types of calorimeters have excellent position and energy resolution. The PbSc has better linearity and timing capabilities while the PbGl boasts exceptional granularity and energy resolution. After correcting for noise contribution, the energy resolution of these two types of calorimeters are listed below:

$$\frac{\sigma_{PbSc}(E)}{E} = \frac{8.1\%}{\sqrt{E}} \oplus 2.1\% \quad (2.6)$$

$$\frac{\sigma_{PbGl}(E)}{E} = \frac{5.9\%}{\sqrt{E}} \oplus 0.8\% \quad (2.7)$$

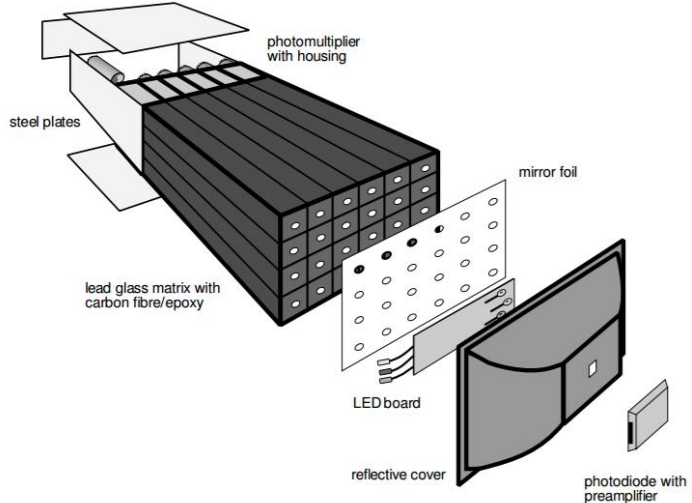


Figure 2.15: A cutaway view of one PbGl supermodule.

The high granularity, 0.011×0.011 for PbSc and 0.008×0.008 for PbGl, allows for π^0 reconstruction via $\pi \rightarrow \gamma\gamma$ channel up to $p_T = 15$ GeV/c [49]. Above 15 GeV/c, the highly energetic photons have small angular separation, causing their showers to merge. This makes it hard for them to be distinguished from a single electromagnetic shower. PbSc has a better intrinsic timing resolution of < 200 ps for electromagnetic showers compared to that of PbGl (< 300 ps). Both detectors have a similar radiation thickness of about 18 radiation length. These two types of calorimeters, with different characteristics, allow for cross checks of photon related measurements.

Generally photons and electrons have a distinctive electromagnetic shower pattern in material which can be distinguished from hadronic particles that usually produce very different energy deposition patterns. An electromagnetic shower shape cut is used in PHENIX data analysis, as one of the requirements to select EMCAL clusters as potential photon candidates. This cut has been carefully studied. The general idea is to use an analytical way to parametrize the energy sharing among neighboring towers and its fluctuations based on identified electron measurement [51]. Then a χ^2 can be calculated to quantify the likelihood that a shower in the EMCAL actually comes from an electromagnetic particle:

$$\chi^2 = \sum_i \frac{(E_i^{pred} - E_i^{meas})^2}{\sigma_i^2} \quad (2.8)$$

where i represents each individual tower that contains the shower; E_i^{pred} is the predicted energy calculated from the model parametrization; σ_i is the model predicted fluctuations; E_i^{meas} is the energy experimentally measured in a single tower i. One can cut on this variable in order to accomplish hadron rejection. Fig. 2.16 shows the χ^2 distributions for showers produced by pions and electrons of 2 GeV. One can observe that the two distributions are distinctly different from each other. Usually a requirement of $\chi^2 < 3$ is used when selecting a cluster as a single electromagnetic shower and including it in the photon sample.

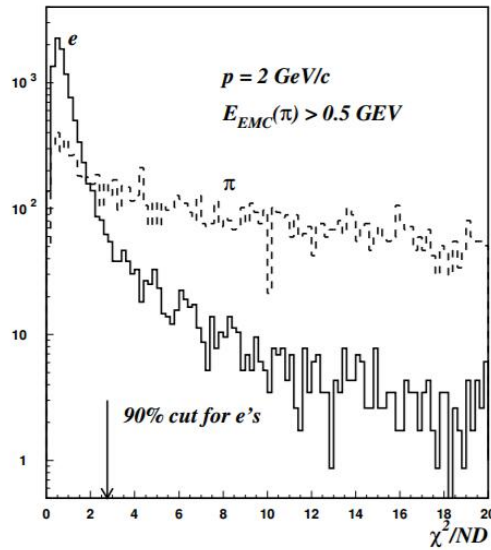


Figure 2.16: χ^2 distributions for electromagnetic showers produced by electrons (solid line) and pions (dashed line) of 2 GeV/c in the PbSc calorimeter.

On the other hand, charged hadrons can sometimes be mistakenly taken as an electron or photon with small energy since they also produce light in the PbSc sectors. A key analysis cut to reject hadrons is the E/p cut. Electrons deposit most of their energy in the calorimeter while hadrons do not. Therefore the ratio of the measured total energy and momentum $E/p \approx$

1 for electrons and $E/p < 1$ for hadrons. This cut is common in analyses requiring electron identification.

EMCal calibrations

A fundamental calibration of the EMCal is determining the "gain factor", that quantifying the conversion from discrete counts (converted from analog voltage signals from PMTs) to a measured energy. In PHENIX, it is achieved by frequently aiming a laser beam of a specific energy at the PMTs during the run (except during bunch crossings), in order to measure live detector shower response and monitor fluctuations in the gain [84]. This maintains the calibration as a function of time.

A recalibration is performed offline to set the absolute energy scale for the calorimeter. We match the reconstructed π^0 mass to its expected mass. It is an iterative procedure as explained below:

- Reconstruct π^0 s in each EMCal tower by pairing photons and plotting their invariant mass distribution. This is done after event selection and applying a few basic requirements on cluster p_T to reduce combinatorial pairs. The tower location was determined by the position of the target photon.
- Fit each mass distribution, fit a Gaussian + polynomial function to determine the π^0 peak position and width. Sample fits are shown in Fig. 2.17.
- Obtain an energy coefficient for each tower by correcting the fitted π^0 mass peak position to the PDG value. Checks were performed after each iteration by eye since the automated fitting does not always work well in which case the peak positions or peak widths are way off. Some necessary manual correction to the fitting therefore needs to be applied.
- Iterate from step 1 after applying the new coefficients. The energy of the cluster is recalculated before reconstructing π^0 s. Note that the energy coefficients of the determined uncalibrated towers and 1840 edge towers are set to the mean value of the coefficients in the corresponding supermodule during iterations.

This type of recalibration is typically used for EMCal-based analyses in PHENIX. Fig. 2.17 to 2.19 demonstrate the result of the EMCal recalibration

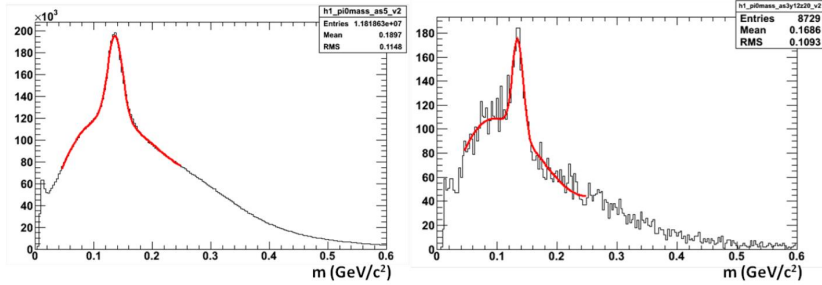


Figure 2.17: 2γ invariant mass distributions showing sample fits for π^0 peaks in one EMCAL PbGl sector (left) and in one tower of a PbSc sector (right).

performed on datasets of uranium-uranium and copper-gold collisions taken in Run-12.

An EMCAL "warnmap" is a list of potentially problematic towers which typically contains hot/dead tower id's. For this particular study, the warnmap is generated by studying the tower-by-tower hit frequency distributions. The frequency distributions are fit to a Gaussian function. Towers are marked as hot if the hits are beyond a certain limit (8 standard deviations for PbSc sectors and 15 standard deviations for PbGl sectors). Towers are marked as dead if there is no hit at all. As a side note, more discussion on warnmap determination regarding the Run-11 gamma-hadron correlation analysis will be presented in section 3.4.1. During the calibration process however, towers that are determined as hot in this way are not necessarily uncalibratable. They are calibrated only as targets (where to select leading photons). They are not used as pair towers in order to reduce the background of combinatorial pairs. Fig. 2.18b shows the initially determined warnmap and the final uncalibrated tower map. There are overlapping regions between the two as expected. The determined coefficient tower map is in Fig. 2.18c. Fig. 2.19 shows the π^0 peak position distributions and the p_T dependence before and after the recalibration. The peak positions become closer to the true value and are relatively independent of p_T . The online calibration was already done properly, so the recalibration step only performed 3 iterations.

Ring Imaging Cherenkov detector

In this analysis, it is important to identify charged hadrons as well as photons. Electrons can in principle contaminate both the trigger and the associate

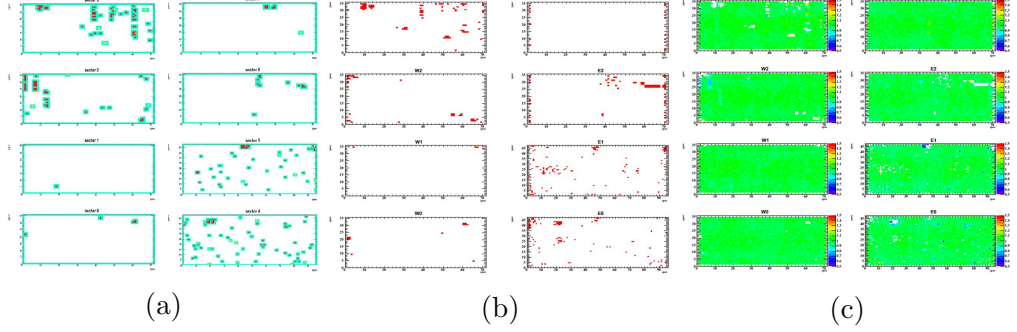


Figure 2.18: Generated EMCAL maps for Run-12 U+U and Cu+Au datasets: (a) a warnmap for each sector. The red areas represent hot/dead towers while the green represents neighboring and edge towers. (b) final uncalibrated tower map. (c) 2-D tower-by-tower coefficients map, in which the blank spots represent the uncalibrated towers. For each map, 4 sectors on the left represent PbSc sectors in the west arm; 4 sectors on the right are in the east arm (with sector 4,5 being PbGl and 6,7 being PbSc). x and y axes label the tower positions along the z and y directions according to the PHENIX coordinates.

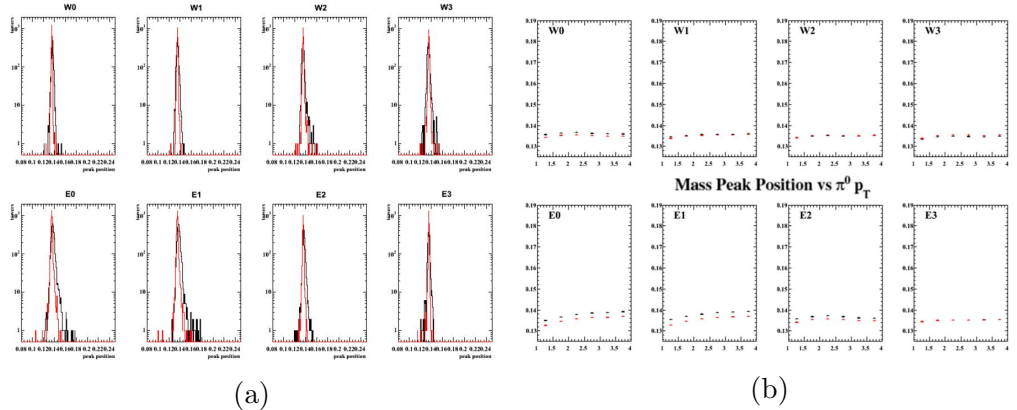


Figure 2.19: Before (black) and after (red) calibration: (a) π^0 peak position tower-by-tower distributions; (b) mean vs p_T .

partner samples, since they produce electromagnetic showers in the EMCal and also taken as charged tracks seen in the central arm tracking system. The Ring Imaging Cherenkov detector (RICH) is one of the primary detector for electron identification in order to remove them from the hadron sample. Cherenkov detectors take the advantage of the fact that prompt photons are produced ("Cherenkov radiation") when particles travel through medium with a speed faster than light in that medium: $v_p > c/n$ with n being the index of refraction of the material. The emission angle of the photons with respect to the direction of the particle trajectory is determined by the particle velocity.

$$\cos\theta_c = \frac{1}{n\beta} \quad (2.9)$$

where $\beta = v_p/c$ with v_p being the particle velocity; The threshold of the particle velocity to produce Cherenkov light is $\beta_t = 1/n$, when the emission angle $\theta_c = 0$. A threshold Cherenkov detector is able to set apart particles with velocities above and below this Cherenkov threshold. Furthermore the number of observed photoelectrons detected together with information of particle momentum are used to determine particle species, with the assistance of the central tracking system [57].

Typically a Cherenkov detector consists of a radiator through which charged particles pass and photons are radiated, as well as a photodetector for light detection and collection. PHENIX has a pair of RICH detectors, with a size of $40 m^3$ each. The RICH is installed behind the PC1 in west and east arms, as shown in Fig. 2.3. For each RICH detector, the Cherenkov light is focused onto 1280 PMTs forming a ring-like image by spherical mirrors of a total reflecting area of $20 m^2$ [56]. Fig. 2.20 is a inside view of one of the RICH detectors. The RICH is designed to distinguish electrons from an abundance of heavier charged particles, predominantly pions. CO_2 is chosen as the radiator gas because of its small index of refraction, to optimize the e/π discrimination capability. As a result, electrons start to radiate at about $0.02 \text{ GeV}/c$, while pions - as the next lightest charged particles - have a Cherenkov threshold at about $4.7 \text{ GeV}/c$. In this analysis a requirement of no hit in PMTs is used to reject electrons from hadron sample.

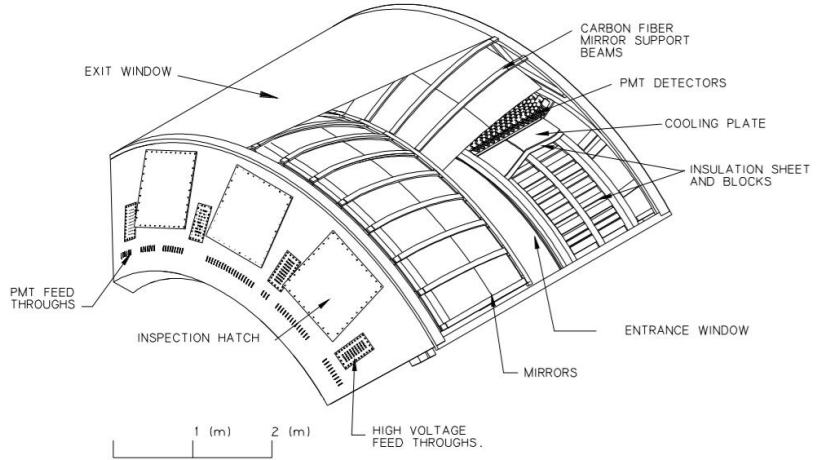


Figure 2.20: An interior view of one of the RICH detector [56]

2.2.5 Silicon Vertex Tracker

In 2011, a silicon vertex tracker (VTX) was installed and started its commissioning in PHENIX. The VTX is positioned close to the collision point, as shown in Fig. 2.3. A beryllium beam pipe with 2.16 cm inner diameter and 760 μm nominal thickness (corresponding to 0.24% radiation length) was also newly installed to reduce conversion electrons as well as multiple scatterings before the VTX. The VTX covers both west and east arms each with an acceptance of $\Delta\phi \approx 0.8\pi$ in azimuth and $|\eta| < 1.2$ in pseudorapidity. The VTX includes 4 layers of silicon detectors illustrated in Fig. 2.21. The two inner layers, B0 and B1 are silicon pixel detectors with a position resolution of $\sigma_\phi = 14.4 \mu m$ along azimuthal direction and $\sigma_z = 123 \mu m$ along z direction. The outer layers B2 and B3 are built using silicon stripixel sensors with an azimuthal resolution of $\sigma_\phi = 23 \mu m$ [81].

The addition of the detector could improve tracking capabilities in the central arms. The major physics drive for using the VTX is to distinguish decay products of particles carrying heavy charm quarks, by measuring the displacement of their trajectories from the collision vertex [67]. The VTX detector is not used in analyzing the data presented in this dissertation.

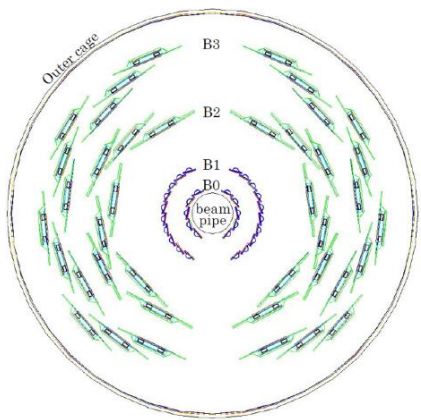


Figure 2.21: A schematic view of the VTX detector layout in PHENIX. Surrounding the beam pipe at radial distances of 2.6 cm and 5.1 cm are the two inner layers B0 and B1, each consisting of 10 and 20 pixel ladders, respectively. Further away from the center at about 11.8 cm and 16.7 cm are the two outer layers B2 and B3, each includes 16 and 24 stripixel ladders.

Chapter 3

Analysis Details

In this chapter, a detailed description of the analysis method will be presented. In a nutshell, there are several types of signals and backgrounds we encounter and deal with in this analysis. During the following discussion, the first type comes up when describing two-particle correlation framework. The signal refers to the "jet pairs" that needs to be extracted. The background means the combinatorial pairs coming from underlying event that do not carry real physical correlations. This background subtraction is based on the assumption of a "two-source model" and it is used to determine inclusive photon-hadron, π^0 -hadron and decay photon-hadron correlations. Since in AA collisions, the background carries a momentum anisotropy known as flow, correlations from flow also needs to be removed. The methods to determine the background level and flow correlation removal are described in section 3.3.

The ultimate signal we measure is the final associated hadron yields triggered by direct photons. This is obtained by using a statistical subtraction method, to remove the decay photon triggered hadron yields from the measured inclusive ones. Decay photon-hadron yields are evaluated using a Monte Carlo simulation pair-by-pair mapping procedure using the input of measured π^0 -hadron yields. The relevant section is 3.7.

Data quality assurance and event selection is presented in section 3.1 and 3.2. Particle selection and the efficiency corrections it comes with are discussed in section 3.4 - 3.6.

In order to study in-medium jet fragmentation function modification, the data is also analyzed in ξ bins (ξ is related to the momentum fraction carried by the hadron from the parton it fragmented from). We present the method

used and explain the analysis procedure. Tests on the method are carried out and summarized in section 3.8.

3.1 Data and event selection

The data set that is analyzed and presented in this dissertation is Au+Au collisions at $\sqrt{s_{NN}} = 200$ GeV, taken with PHENIX detectors in 2011. Minimum bias (MB) events are recorded with using a trigger requirement of BBCLL1 (>1 tube). After all cuts to optimize the data quality, a total of 4.4×10^9 events are processed for this analysis.

Events are selected by applying a standard z-vertex cut: $|z_{vertex}| < 30$ cm. The data is analyzed in centrality binning of 0–20%, 20–40%, 40–60% and 60–92%.

Triggers (photons and π^0 s) are binned in momentum ranges of 5-7, 7-9, 9-12 and 12-15 GeV/c. Partners (associate charged hadrons) are binned in p_T ranges of 0.5-1, 1-2, 2-3, 3-5, 5-7 GeV/c. Since the goal of this analysis is to add statistics to improve the previous direct photon-hadron correlation results, all binnings are kept the same as those in the earlier analyses [74].

3.2 Run quality assurance

Each analysis requires run quality assurance (QA) tailored to the observable(s) of interest. For this analysis, since we study two-particle correlations by measuring angular distributions of the pairs, the run QA is done by looking at the cluster-track $\Delta\phi$ distributions run by run to ensure the pair acceptance is uniform across all runs. In general, the measured two-particle correlations contain both the signal and background pairs and are referred to as foreground pairs.

The azimuthal angular difference $\Delta\phi$ between a cluster and a reconstructed track is calculated and a $\Delta\phi$ distribution for all the cluster-track pairs can be plotted for each run. We compare the $\Delta\phi$ shape of each run with that of all runs combined. The ratios between these foreground pair $\Delta\phi$ for each run to the summed $\Delta\phi$ are fitted with a flat line and the χ^2 per degree of freedom (dof) is calculated. Fig. 3.1 is an example of such run-by-run $\Delta\phi$ distribution ratios, fits and χ^2/dof values.

Run selection is accomplished using the distribution of the resulting fit χ^2/dof as a function of run number, plotted in Fig. 3.2. The purpose of checking the pair distributions is to ensure that the acceptance and track distributions are stable across the full run statistics. Since there could be statistical fluctuations, a relatively large χ^2/dof does not necessarily suggests

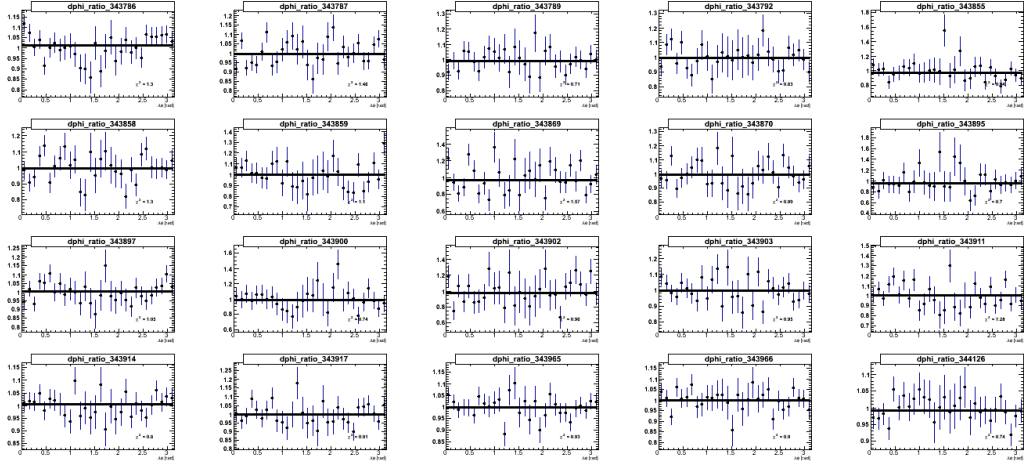


Figure 3.1: Examples of run-by-run $\Delta\phi$ distribution ratios and fits for foreground inclusive cluster and reconstructed track pairs.

a bad run. For all runs with χ^2/dof value above 2, the $\Delta\phi$ ratio is visually inspected to look for shape differences, and the conclusion is that they should be kept for the analysis.

Besides the pair acceptance, additional run-by-run checks are performed by checking the reconstructed π^0 s, which will be discussed later.

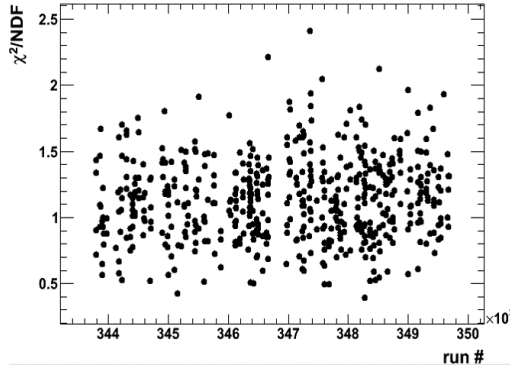


Figure 3.2: χ^2 of a flat line fit to the ratios of the foreground pair distributions to the combined distributions, as a function of run number

3.3 Two particle correlations

We have discussed the importance of measuring two particle correlations in Chapter 1. Given its compelling nature as a statistical technique in studying jet physics, two particle angular correlation method is usually favored over jet reconstruction measurements in high multiplicity situations, as it would be very difficult to remove soft background event-by-event, especially in PHENIX which has limited detector acceptance.

For this analysis, we are interested in studying the modification of the jet fragmentation function in heavy ion collisions by measuring the yield of associated hadrons correlated with high momentum direct photons. In that sense the production rate of the direct photon triggers is not of primary concern. Instead, a quantity typically referred to as the "conditional yield" or "per-trigger yield" is constructed as a function of the azimuthal angle $\Delta\phi$ between triggers (denoted as particle A) and associated partners (denoted as particle B):

$$\frac{1}{N_A} \frac{dN_{AB}}{d\Delta\phi} \quad (3.1)$$

where N_A represents the number of trigger particles and $\frac{dN_{AB}}{d\Delta\phi}$ is the number of jet pairs in a particular $\Delta\phi$ bin ($\Delta\phi = \phi^A - \phi^B$).

3.3.1 Two-Source Model

After detector acceptance correction, only the actual physical correlations between the trigger and partner particles remains. This is usually called as the correlation function $C(\Delta\phi)$, which will be defined in section 3.3.1 . We assume that pairs arise from jet correlations superimposed on a combinatorial background from the underlying event. This two source model assumption can be expressed in the following way:

$$\frac{dN_{AB}^{fg}}{d\Delta\phi} = \frac{dN_{AB}^{jet}}{d\Delta\phi} + \frac{dN_{AB}^{bg}}{d\Delta\phi} \quad (3.2)$$

The background term has contributions from pairing 1) two particles from two unrelated jets, 2) one jet particle and one non-jet particle; 3) both particles coming from non-jet source(s) [69].

One could rewrite the above into:

$$C(\Delta\phi) = J(\Delta\phi) + b_0(1 + 2\langle v_2^A v_2^B \rangle \cos(2\Delta\phi)) \quad (3.3)$$

Correlations after removing the combinatorial background is usually referred to as the jet function $J(\Delta\phi)$. In AA collisions, the background has an azimuthal anisotropy shape quantified by v_n , (dominated by v_2), which will be discussed later. b_0 stands for the background level. The conditional yield or per-trigger yield of associated hadrons therefore can be expressed as follows:

$$\frac{1}{N_A} \frac{dN_{AB}^{jet}}{d\Delta\phi} = \frac{1}{N_A} \frac{N_{AB}^{real}}{\epsilon^B \int \Delta\phi} \left\{ \frac{dN_{AB}^{real}/d\Delta\phi}{dN_{AB}^{mix}/d\Delta\phi} - b_0[1 + 2\langle v_2^A v_2^B \rangle \cos(2\Delta\phi)] \right\} \quad (3.4)$$

In this analysis, we determine inclusive photon-hadron, π^0 -hadron and decay photon-hadron jet functions. Then a statistical subtraction method is used to remove the decay photon triggered hadron yields from the inclusive ones, in order to get the final direct photon-hadron yields. Details on that will be discussed in section 3.7.

Event Mixing

Event mixing is commonly used to determine the acceptance correction and the level of background. As the name suggests, event mixing takes particles of a particular trigger type from one event and pairs them with particles of a partner type from a different event. The events the trigger and associate partner particles are drawn should belong to the same class, i.e. sharing very similar collision centralities and vertex positions. Fig. 3.3 shows a diagram illustrating how two particle pairing is constructed using event mixing. Pairs constructed from mixed events determine detector acceptance as they do not contain any actual physical correlations but all other correlations from background remain. Fig. 3.4 demonstrates a representative azimuthal angular distribution of uncorrelated pairs using event mixing. The measured shape is not uniform in azimuth due to the PHENIX specific limited acceptance, which also includes dead and inefficient detector areas. The two peaks around 0 and π radians arises from the positioning of the two central arms as shown in Fig. 2.3a, each arm covering $\pi/2$ rad in azimuthal angle but are placed not exactly back-to-back, making two-particle correlation measurement near $\Delta\phi = \pi/2$ possible (statistics are lower in this region). Taking a ratio of the same event pair distribution to mixed pair distribution reveals physical correlations, as the pair detector acceptance effects cancel out. An analytical proof is presented in [88].

The correlation function $C(\Delta\phi)$ can be obtained as the following:

$$C(\Delta\phi) = \frac{dN_{AB}^{real}(\Delta\phi)}{d\Delta\phi} / \frac{dN_{AB}^{mix}(\Delta\phi)}{d\Delta\phi} \quad (3.5)$$

which is essentially the acceptance corrected correlations.

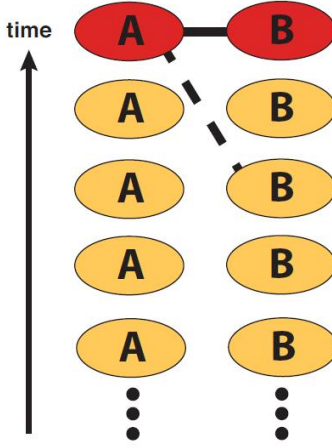


Figure 3.3: A cartoon illustrating event mixing in a simplified way [82]. The solid line denotes a pair from the same event which is not allowed, while the dashed line connects a mixed event pair. Events are characterized according to the collision centralities and z-vertex positions. Particles of type B from each event is stored in the corresponding designation in the mixing pool. Pairing is carried out by associate trigger particles of type A with particle B that shares the same global event characteristics.

When using event mixing to determine background level, the assumption is that the pair rate from mixed events can match the true background in the measured foreground distributions. Particles come from either jets or non-jet sources. The "signal" we are looking for is the particle yield from jet fragmentation. Particle pairs can either come from the same jet, or from back-to-back jets. The former shows as a peak at $\Delta\phi$ around zero ("the near-side") and the latter produces a broadened peak at $\Delta\phi$ around π ("the away-side"). The broadened peak arises from the fact that the away-side jets suffer multiple scattering when traversing through the medium. It also has contributions from the effect of k_T - the initial momentum imbalance

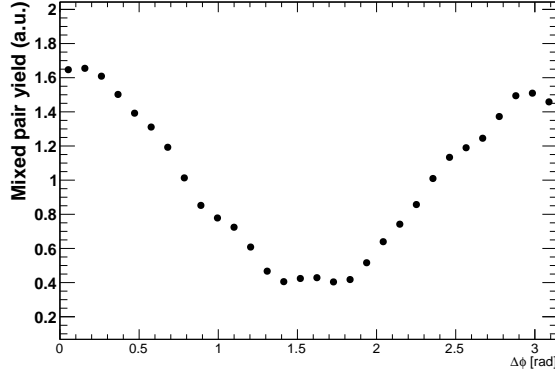


Figure 3.4: A typical $\Delta\phi$ distribution of uncorrelated pairs measured using event mixing.

between the colliding photon and parton due to the intrinsic acoplanarity carried by the parton inside the nucleon.

Next, the background normalization can be determined using event mixing, or by ZYAM as described later. The following discussion is for illustration purpose to explain how one determines the background level using event mixing.

We take the near-side pair distributions as an example. When constructing foreground pairs from one event, the following five cases are all possible combinations and need to be taken into account to calculate the total number of pairs $N_{AB}^{fg,i}$ (i labels each case) [87]:

1. A and B come from the same jet: $N_{AB}^{fg,1} = N_{jet} \langle N_A^{jet} N_B^{jet} \rangle$
2. A comes from a jet and B comes from background: $N_{AB}^{fg,2} = N_{jet} \langle N_A^{jet} \rangle N_B$
3. A comes from background and B comes from a jet: $N_{AB}^{fg,3} = N_{jet} \langle N_B^{jet} \rangle N_A$
4. A and B come from two different jets: $N_{AB}^{fg,4} = N_{jet} (N_{jet} - 1) \langle N_A^{jet} \rangle \langle N_B^{jet} \rangle$
5. A and B both come from background: $N_{AB}^{fg,5} = N_A N_B$

Here N_A (N_B) is the number of trigger type (partner type) background particles per event. N_{jet} is the number of jets per event. $\langle N_A^{jet} \rangle$ ($\langle N_B^{jet} \rangle$) is the average number of type A (B) particles per jet in an event. It is clear to see that except scenario 1, all sources belong to background and needs to be subtracted:

$$N_{AB,bg}^{real} = N_{jet} \langle N_A^{jet} \rangle N_B + N_{jet} \langle N_B^{jet} \rangle N_A + N_{jet} (N_{jet} - 1) \langle N_A^{jet} \rangle \langle N_B^{jet} \rangle + N_A N_B \quad (3.6)$$

Now if we consider the same quantity $N_{AB}^{mix,i}$ constructed using event mixing technique, all the possible pair combinations are:

1. A and B both come from background: $N_{AB}^{mix,1} = N_A N'_B$
2. A comes from background and B comes from a jet: $N_{AB}^{mix,2} = N_A N'_{jet} \langle N_B^{jet'} \rangle$
3. A comes from a jet and B comes from background: $N_{AB}^{mix,3} = N'_B N_{jet} \langle N_A^{jet} \rangle$
4. A and B comes from two different jets: $N_{AB}^{mix,4} = N_{jet} N'_{jet} \langle N_A^{jet} \rangle \langle N_B^{jet'} \rangle$

where $'$ denotes a different event. Since we construct event mixing in the way that type B particles are pulled out of the "mixing pool", N'_B , N'_{jet} and $\langle N_B^{jet'} \rangle$ represent the number of partner particles per mixed event, the number of jets per mixed event, average number of partners per jet in an mixed event, respectively. Hence the total number of mixed pairs are:

$$N_{AB,bg}^{mix} = N_A N'_B + N_A N'_{jet} \langle N_B^{jet'} \rangle + N'_B N_{jet} \langle N_A^{jet} \rangle + N_{jet} N'_{jet} \langle N_A^{jet} \rangle \langle N_B^{jet'} \rangle \quad (3.7)$$

Equating $N_{AB,bg}^{real}$ and $N_{AB,bg}^{mix}$ would involve a few assumptions as will be explained below. Careful construction and treatment in the analysis set-up for event mixing is required. Foreground pairs come from the same event, with same collision vertex and centrality values. For mixed pairs, on the other hand, come from two different events. Therefore it is critical to make sure that the pairing in mixed events are identical or carry only infinitesimal differences compared to what is done in real events (ideally the only difference should be that the trigger and partner particles come from two events instead of one). One important step is to ensure the mixed event to share very similar global characteristics, most importantly, centrality and vertex position. To minimize the possible event level difference that leads to mixed events being not representative for depicting detector acceptance, we require partners to come from an event that falls in a particular small centrality and vertex bin as the real event. In this analysis we are using 5% in centrality binning and 5 cm in z-vertex binning. Mixing triggers from central events with partners from peripheral events, for example, will underestimate the pair production rate and therefore also the background level.

We store real event information in an event mixing pool (with a large but finite depth of 180 events). Triggers from a real event are paired with

hadrons picked from a different event in the event pool. Since the pool size is reasonably large, we can assume that $N_B = N'_B$ and $N_{jet}\langle N_B^{jet}\rangle = N_{jet}\langle N_B^{jet}\rangle$, namely the production rate of jets as well as that of the associate hadrons from a mixed event equals to what is in the foreground (real) event. On top of that, if we assume $N_{AB}^{fg,4} = N_{AB}^{mix,4}$, event mixing is able to reproduce the background level. There is a multiplicity effect resulting from the finite centrality binning of the mixed events and needs to be corrected for. This will be discussed in section 3.3.1. Any correction from the z-vertex binning in the mixing procedure was found to be negligible [83].

ZYAM method

Typically in p+p and d+Au collisions, where the event multiplicity is relatively low, the background shape is assumed to be flat across $\Delta\phi$. One way to determine the background level to be subtracted is the Zero-Yield-At-Minimum (ZYAM) procedure. This method assumes that the jet correlation is zero (or negligible) at the minimum value of the correlation function in $\Delta\phi$ [69]. Given the premise that the jet contribution and combinatorial background are from independent sources, the latter can be subtracted. An illustration of signal and background separation is shown in Fig. 3.5. For the case where both the near-side and away-side peaks are relatively narrow and therefore are well-separated in $\Delta\phi$, there is a nearly flat and broad continuum in the middle $\Delta\phi$ region (see Fig. 3.5a). ZYAM is a reliable method to determine the level of the combinatorial background since the background contribution is dominant there. On the other hand, if the jet shapes are modified and the peaks are broadened, there could be significant jet yield contributing to the normal ZYAM region. Using the ZYAM method in situations like this is sensitive to the finite binning along $\Delta\phi$ and may result in finding a wrong spot to perform the background subtraction. ZYAM also becomes unreliable when there are not enough statistics (for example in high p_T situations). In that case, locating the ZYAM point/region would be challenging and under-subtraction of background is likely.

The ZYAM procedure is usually an iterative process. First a specific region in $\Delta\phi$, containing the point where the jet yield is zero, is selected. A small initial value is assigned as the tentative background level. The amount of "under-subtraction" (since the starting background level is low) is the difference between this value and the correlations across the $\Delta\phi$ region. The $\Delta\phi$ location with the minimum "under-subtraction" value is located. The

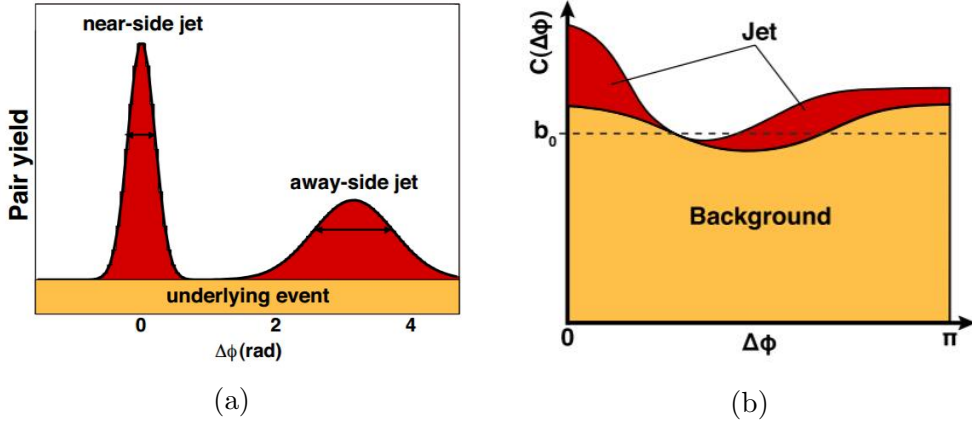


Figure 3.5: An illustration of two-source model: how background shapes and separation from signals in two-particle angular correlation measurements. Red peaks stand for jet signals and the yellow regions are background. (a) represents a typical p+p collision that background is flat and the level is relatively low. (b) is for Au+Au collisions, in which the background is much higher and has harmonic shape known as flow. Both ZYAM and ABS method can be applied for background subtraction in these two cases. For the Au+Au analysis discussed in this dissertation, ABS method is used to determine background level.

starting normalization level is then increased by half of the under-subtracted amount at the ZYAM $\Delta\phi$. Next, a new and possibly different "ZYAM point" would be determined by repeating the procedure. The iteration continues until the difference falls to nearly zero. The ZYAM method can also be applied to heavy-ion collisions, in which the background is not flat but has a harmonic shape from flow, the determined "ZYAM" point is not usually the lowest point in the initial correlation function in this case. The jet and background shape in such a scenario are illustrated Figure 3.5b.

ABS method

In this analysis, the absolute normalization method (ABS) is used to determine combinatorial background level. It is achieved by using the event mixing technique discussed above. It has been demonstrated to be robust in both p+p and Au+Au collisions [83, 80]. The ABS method has an advantage over ZYAM method for high p_T situations in which the statistics are

low, which makes locating "zero-yield" point/region difficult.

Ideally, the background pair production rate is equal to the product of single particle production rates:

$$\langle n_{bg}^{AB} \rangle = \langle n^A \rangle \langle n^B \rangle \quad (3.8)$$

The background level therefore is:

$$b_0^{ideal} = \frac{\langle n_{bg}^{AB} \rangle}{\langle n_{same}^{AB} \rangle} = \frac{\langle n^A \rangle \langle n^B \rangle}{\langle n_{same}^{AB} \rangle} \quad (3.9)$$

where $\langle n^A \rangle$ and $\langle n^B \rangle$ are measurable.

When making mixed pairs, partner particles are taken from the event pool in which events with the same collision centrality and vertex positions. One bias in reproducing the mixed particle single and pair production rate arises because of the finite centrality binning in the event pool. Namely n^A and n^B are larger for more central events compared to peripheral events. Consequently, the measured background pair number would be larger than the foreground pair number: $\langle n_{mix}^{AB} \rangle > \langle n^A \rangle \langle n^B \rangle$. This effect should be corrected to accurately determine the background level. We define as follows a scale factor to correct for this multiplicity effect:

$$\xi \equiv \frac{\langle n^A n^B \rangle}{\langle n^A \rangle \langle n^B \rangle} \quad (3.10)$$

Naturally one would expect that the single-particle production rates for both triggers n^A and associate partners n^B can be expressed as a function of a certain global quantity that relates to the particle production of the collision. Typically we can use the number of participants in the collision N_{part} or the number of binary collisions N_{coll} , which characterizes the centrality (or particle multiplicity) of the collision. The variation in the measured $\langle n^A \rangle$ and $\langle n^B \rangle$ depends on the centrality binning in the event mixing: wider centrality bins would yield to larger variation on the particle production rate.

To calculate ξ , we utilize Glauber calculations. If we rewrite the above equation as:

$$\xi = \frac{\sum_i n_i^A n_i^B w_i^{glaub}}{\sum_i n_i^A w_i^{glaub} \sum_i n_i^B w_i^{glaub}} \sum_i w_i^{glaub} \quad (3.11)$$

in which index i loops over all N_{part} or N_{coll} values; n_i^A (n_i^B) is the average number of type A (B) particles for a given N_{part} or N_{coll} ; w_i^{glaub} represents the probability of a specific N_{part} or N_{coll} value to contribute to this particular centrality selection. The multiplicity correction therefore can be viewed as the ratio of event-weighted averages of n^A , n^B and $n^A n^B$ for a centrality bin. Fig. 3.6 is an illustration of how the factor ξ is calculated. Fig. 3.7 shows an example of N_{part} and N_{coll} distributions from the Glauber Monte Carlo calculation.

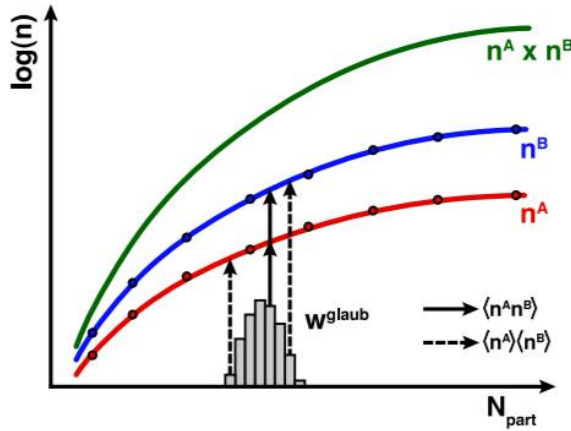


Figure 3.6: ξ calculation [69]

The relation between n^A (n^B) and N_{part} (or N_{coll}), is plotted as a function of N_{part} and N_{coll} as shown in Fig. 3.8. Two functional forms are used to fit the distributions: a saturated exponential function:

$$n^{A,B} = \gamma(1 - e^{-\beta N^\alpha}) \quad (3.12)$$

and an inverse tangent function:

$$n^{A,B} = \gamma \arctan(\beta N^\alpha) \quad (3.13)$$

where γ , α and β are independent parameters determined by the fits. These two functional forms are chosen due to their smoothness when fitting the data and the well-behaved nature at large N. Using two different fitting functions

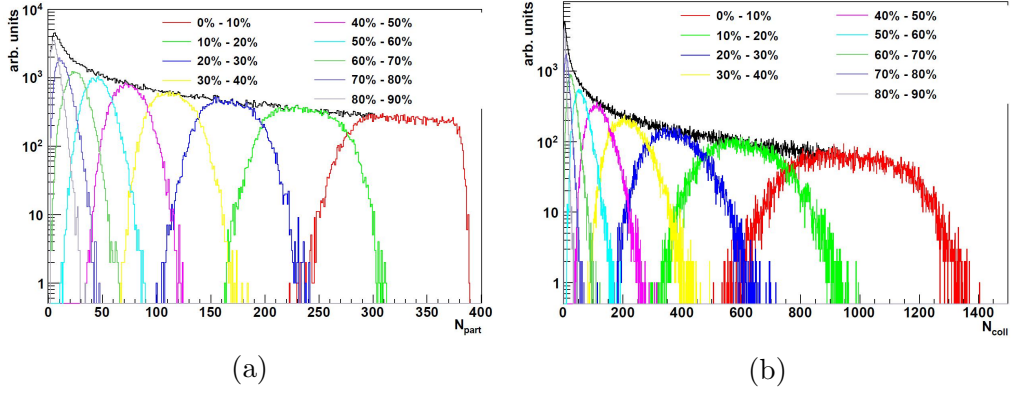


Figure 3.7: N_{part} (a) and N_{coll} (b) distributions from the Glauber calculations.

to fit two types of N (N_{part} and N_{coll}) provides a way to evaluate systematic uncertainty on this procedure. ξ is determined by taking the average of the different fits and the systematic uncertainty is calculated from the maximum dispersion. Fig. 3.9 shows ξ for trigger photon with p_T 5-7 GeV/c and associated hadrons with p_T 0.5-1 GeV/c.

Intuitively we expect that ξ is larger than unity, given the fact that n^A and n^B change in the same direction when centrality changes. Also shown in Fig. 3.9 is the rising trend as the centrality percentile gets bigger. This is because the variation in particle production rates are larger in more peripheral events (particle yields changes more quickly). The calculated ξ has larger values for wider centrality bins as compared to finer bins for the exact same reason.

Elliptic Flow

As v_2 quantifies the azimuthal anisotropy in momentum space caused by the pressure gradient from the initial collision geometry, the values should not change across runs on the same collision system. Therefore the v_2 values that are used in this analysis are from a separate, earlier analysis [80]. Table 3.1 and 3.2 list the v_2 values for inclusive γ , π^0 , decay γ and charged hadrons for 0-20% and 20-40% centrality bins, respectively.

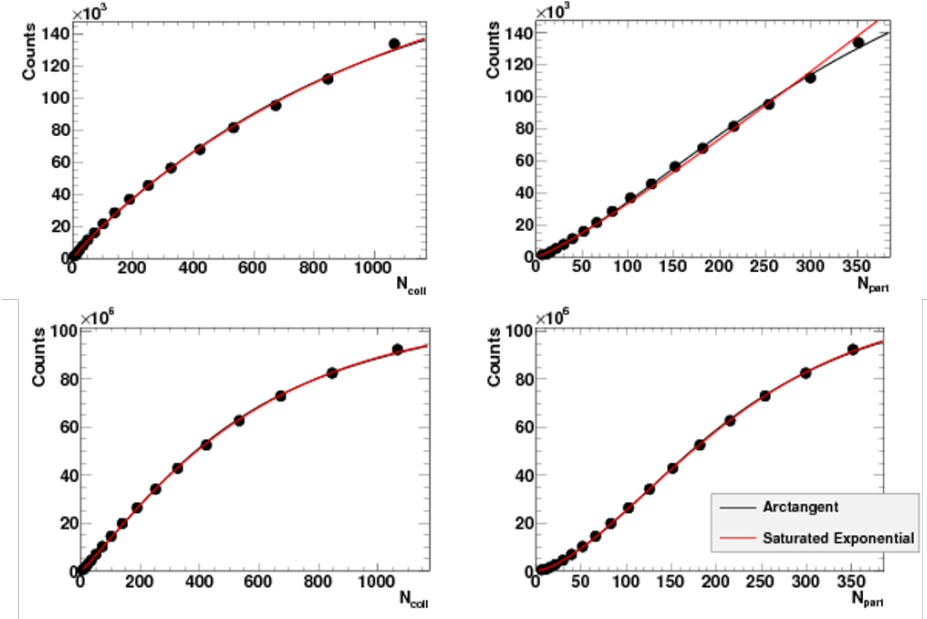


Figure 3.8: Top: number of inclusive photon as a function of N_{coll} and N_{part} ; Bottom: number of hadrons as a function of N_{coll} and N_{part} ; All distributions are fitted with an arctangent (black) and a saturated exponential (red) functional forms.

3.4 Particle Selection

In this analysis, it is important to select good samples of trigger type particles and the the associated partner type particles. The former refers to photons and π^0 s and the latter is charged hadrons. Photons and π^0 are measured in the EMCAL by imposing cuts on the clusters. Charged hadrons are reconstructed via the central arm tracking, using drift chambers and pad chambers. The following sections describe how the particles are selected.

3.4.1 EMCAL Cluster Selection

Exclusion of EMCAL hot towers

Generally, hot towers are those that fire frequently, regardless of whether the signals are actual hits depositing energy in the EMCAL. Hot towers are regarded as problematic and are excluded from the EMCAL acceptance for the

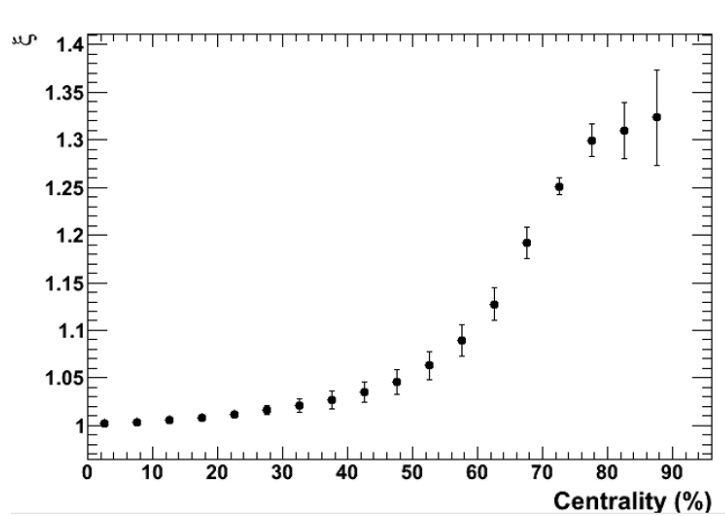


Figure 3.9: ξ as a function of centrality.

Particle	p_T	v_2	Stat. err	Sys. err
inclusive γ	5-7	0.0423226	0.00175307	0.0076029
	7-9	0.0461296	0.00454517	0.00432369
	9-12	0.0398415	0.00836215	0.00344175
π^0	5-7	0.0835297	0.00287215	0.0118235
	7-9	0.0755782	0.00531345	0.00960588
	9-12	0.0839048	0.0101393	0.0180581
decay γ	5-7	0.0802729	0.00259655	0.0106477
	7-9	0.0769908	0.00440387	0.0111283
	9-12	0.0831338	0.00951379	0.0208089
hadron	0.5-1	0.0440219	0.000145508	0.00137609
	1-2	0.0745276	7.62922e-05	0.002022
	2-3	0.109507	0.000216781	0.0030719
	3-5	0.110372	0.000591522	0.003229
	5-7	0.08275	0.00844	0.005

Table 3.1: Triggers and charged hadrons v_2 values for 0-20% centrality bin

analysis. This avoids contamination in the inclusive photon sample, which is imperative for the later statistical subtraction procedure to extract direct photon triggered hadron yields. Hot towers are usually noisy during the

Particle	p_T	v_2	Stat. err	Sys. err
inclusive γ	5-7	0.0852710	0.00207489	0.0179611
	7-9	0.0738878	0.00558803	0.01509860
	9-12	0.0520371	0.01062420	0.02247170
π^0	5-7	0.1335370	0.00330527	0.0229443
	7-9	0.1162020	0.00587208	0.02417620
	9-12	0.1030550	0.01122400	0.03859360
decay γ	5-7	0.1270690	0.00292113	0.0236515
	7-9	0.1142120	0.00505774	0.02610160
	9-12	0.1005180	0.01043080	0.03353270
hadron	0.5-1	0.0826719	0.000171826	0.00296920
	1-2	0.1381520	8.20737e-05	0.00419830
	2-3	0.1933760	0.000249992	0.00579030
	3-5	0.1907190	0.000680041	0.00616680
	5-7	0.1297000	0.01350	0.00830

Table 3.2: Triggers and charged hadrons v_2 values for 20-40% centrality bin

whole run or stay for most of the run, but the definition can be sensitive to the cluster energy thresholds. Two hot tower maps, specific to this analysis are made, using two different cluster energy ranges. The two ranges are above and below 5 GeV, with the first relevant for the inclusive photon selection, and the second for reconstructing π^0 s.

For each cluster energy range, the hit frequency is plotted. Fig. 3.10 shows the tower hit distributions for both cluster energy ranges. Note that the convention we use here to number the 8 sectors is in the following way: 0-3 - PbSc sectors in west arm; 6, 7 - PbSc sectors in east arm; 4, 5 - PbGl sectors in east arm. A cut of 5 sigma above the average is selected, and all towers with higher hit frequency are marked as hot. A 3x3 tower block is removed when the center tower is regarded as hot. Further it is worth mentioning that a fiducial cut and a 2 tower sector edge cut are also applied, excluding photons that happen to hit the edge of the detector and therefore have some fraction of their energy undetected.

Fig. 3.11 and 3.12 show the raw hit distributions for cluster energy smaller and larger than 5 GeV respectively in each EMCal sector, before the hot tower map is applied. Fig. 3.13 and 3.14 show similarly the hit distributions for cluster energy smaller and larger than 5 GeV respectively, but after the

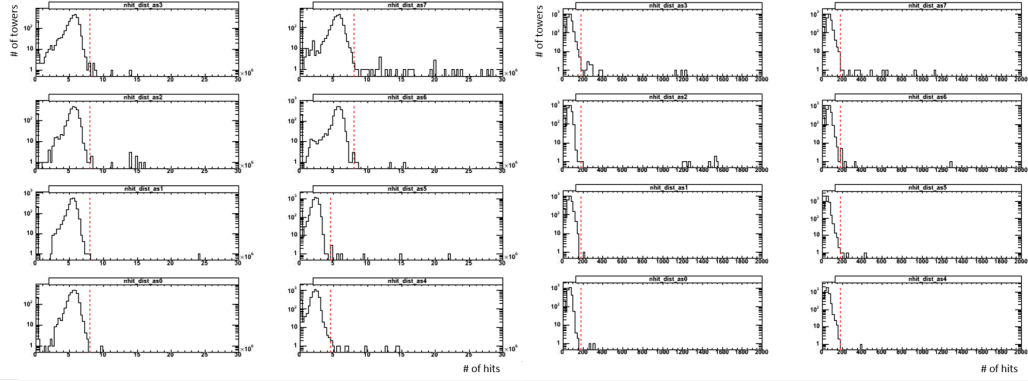


Figure 3.10: Tower hit distributions for cluster energy less than 5 GeV (left) and greater than 5 GeV (right). Red dashed lines represent the 5σ cut that assigned the towers that lie beyond as hot towers.

hot tower map is applied. One would observe that after removing hot towers, the hit distributions are much more uniform, without towers with a very large number of hits. One could also see that the determined hot tower map is not the same for the two energy ranges, allowing to recover some EMCal acceptance for high p_T photons and π^0 measurement.

After the exclusion of hot towers and edge towers, additional run QA was performed by looking at the reconstructed π^0 mass and peak width run-by-run. Fig. 3.15 shows reasonably well-behaved reconstructed π^0 across all runs.

Shower shape cut

The electromagnetic shower shape cut has been discussed in the detector section 2.2.4 above. It is to select photon candidates based on the showering shape clusters leave in the EMCal. In this analysis a standard $\chi^2 < 3$ is used when selecting photon candidates.

Track veto (pair cut)

Pair cuts are necessary in two-particle correlation analyses when the trajectories of both the trigger and associate partner are close enough within the same detector for the resulting signals to merge or interfere with one another. As this analysis pairs EMCal clusters with charged tracks, we also remove

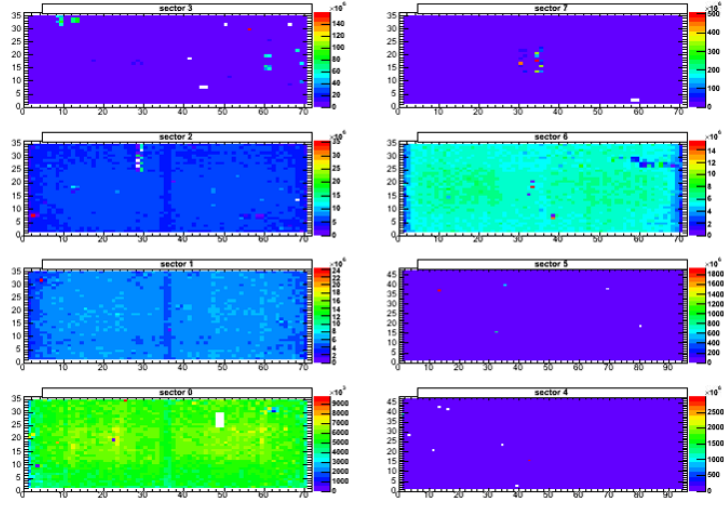


Figure 3.11: Hits in each EMCAL sector for cluster energy less than 5 GeV, before the hot tower map is applied. Four sectors on the left represent EMCAL sectors in west arm (PbSc); Four sectors on the right are in the east arm (with sector 4,5 being PbGl and 6,7 being PbSc). x and y axes label the tower positions along the z and y directions according to the PHENIX coordinates.

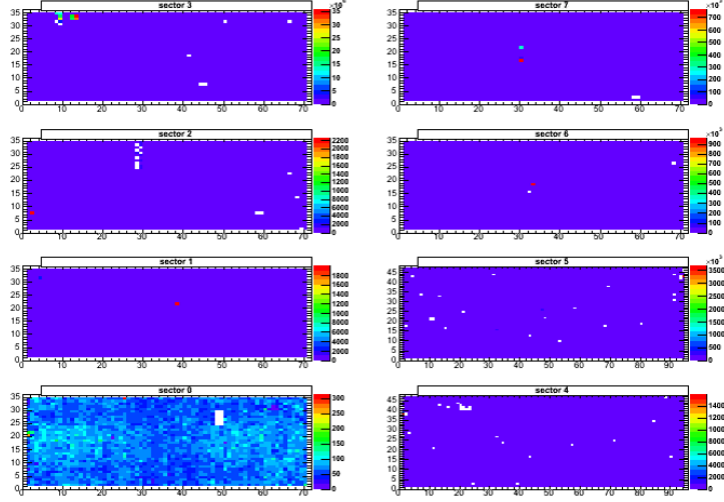


Figure 3.12: Hits in each EMCAL sector for cluster energy greater than 5 GeV, before the hot tower map is applied.

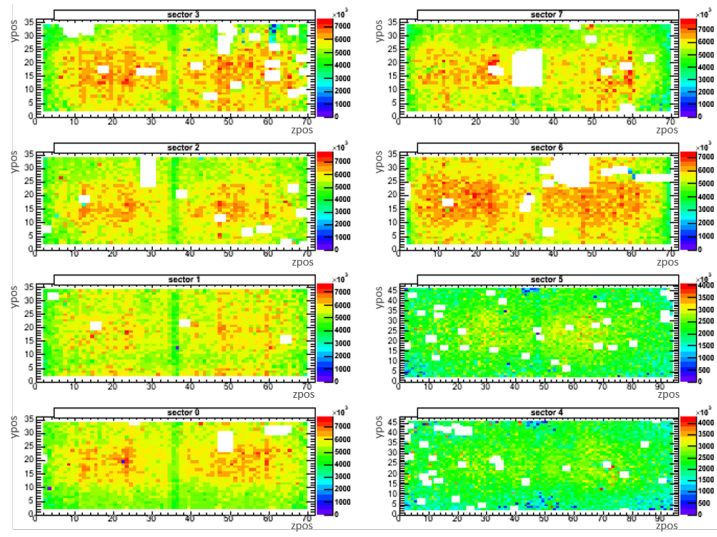


Figure 3.13: Hits in each EMCAL sector for cluster energy less than 5 GeV, after the hot tower map is applied.

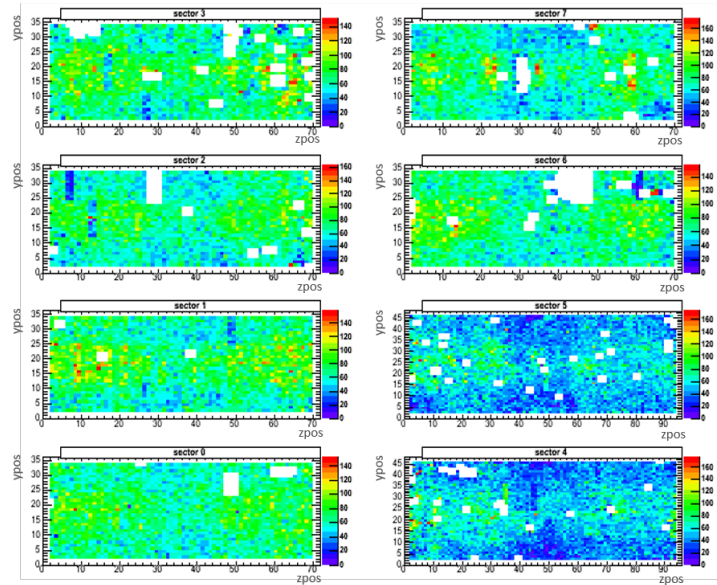


Figure 3.14: Hits in each EMCAL sector for cluster energy greater than 5 GeV, after the hot tower map is applied.

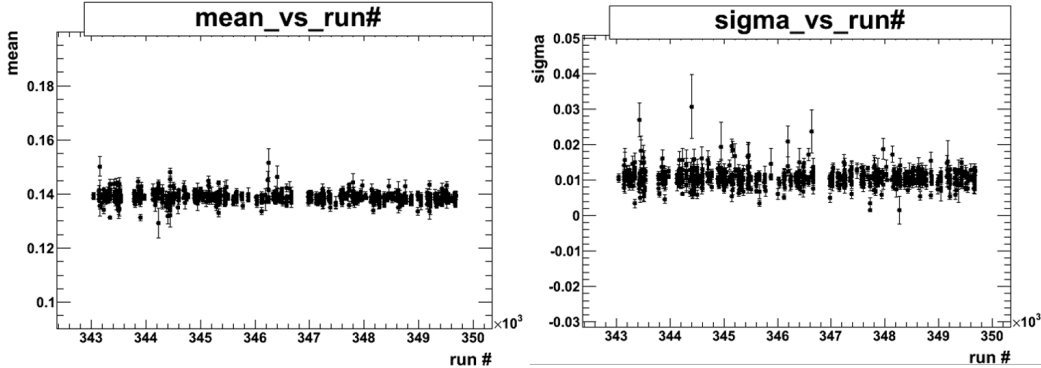


Figure 3.15: Reconstructed π^0 mass peak positions (left) and widths as a function of run number.

background that arises from signals in the two detectors that come from the same particle, so-called "auto-correlations". The two main sources of such background are the hadron straight-through peak in the EMCAL and hadronic contamination of EMCAL clusters. To select a clean photon sample, we apply a χ^2 cut to remove particles giving non-single-electromagnetic shower shapes in EMCAL. The pair cut is useful in rejecting the remaining hadronic showers and some electron contamination.

The pair cut between the EMCAL and hadrons is determined by plotting the distance between each EMCAL cluster and the projection of all tracks to the EMCAL plane; all combinations within the same event are included. The distributions are shown in Fig. 3.16. The bumps at small distance region are recognized as auto-correlations. Hence if the EMCAL cluster has a track closer than 8 cm, the cluster is rejected from further analysis. The same pair cut is implemented in the mixed events, to ensure that the pair acceptance is the same in mixed events as in real events.

3.4.2 π^0 identification

π^0 -hadron correlations are measured in this analysis to determine decay photon-triggered hadron yields. Therefore π^0 identification is important. π^0 s are reconstructed via the $\pi \rightarrow \gamma\gamma$ channel. In each event all photons are paired with one another. The leading photon has the same cuts described above. This ensures that the π^0 sample would have basically the same acceptance as the inclusive photon sample. Both photons are required to come

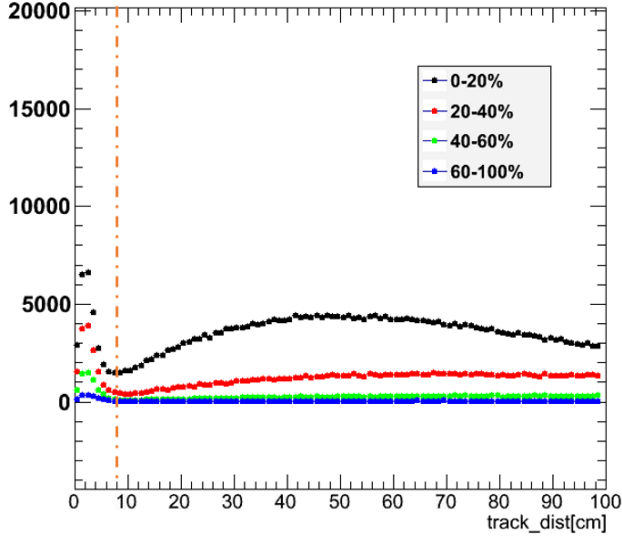


Figure 3.16: Distance between cluster position and track projection in the EMCAL in the same event, for 4 centralities. The dotted dashed line specifies the cut value 8 cm.

from the same EMCAL arm and have cluster energy $E > 1$ GeV in order to reduce the combinatorial background pairs. To cut down more effectively on the amount of incorrect paired photons that are not from the same parent π^0 , we apply an invariant mass requirement as well as an asymmetry cut. The invariant mass is calculated as:

$$m_{\gamma\gamma} = \sqrt{2E_1E_2 - 2(\vec{p}_1 \cdot \vec{p}_2)} \quad (3.14)$$

Fig. 3.17 shows 2γ invariant mass distributions for various trigger p_T bins. Pairs with $0.12 < m_{\gamma\gamma} < 0.16$ GeV/c^2 are accepted as the potential π^0 candidates. A π^0 peak has a finite width is due to the natural broadening and the energy resolution of the EMCAL.

Although a requirement of both photons having energy larger than 1 GeV helps to cut down the combinatorial background pairs constructed with low momentum daughters, a powerful asymmetry cut is implemented to further reduce the background contamination. Most background pairs contain one

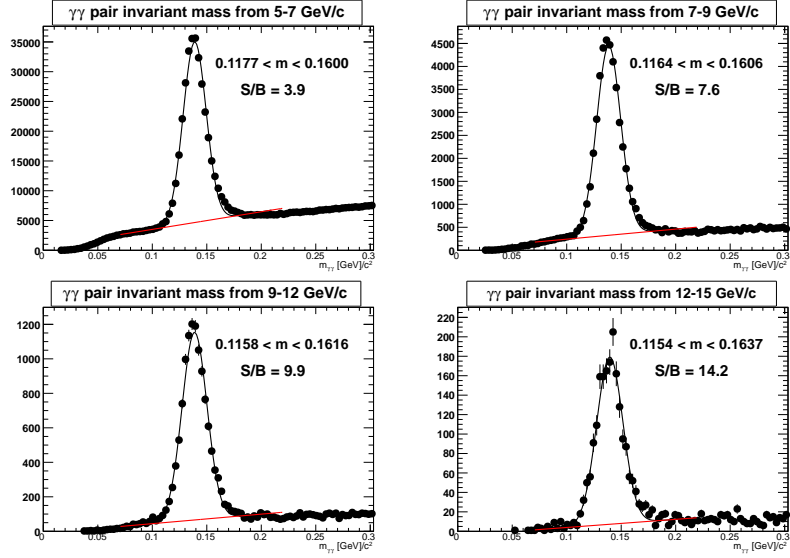


Figure 3.17: 2γ invariant mass distribution showing reconstructed π^0 peaks, for different trigger p_T ranges.

soft photon and one high momentum photon. The energy asymmetry parameter is defined as:

$$\alpha = \frac{|E_1 - E_2|}{E_1 + E_2} \quad (3.15)$$

Two photons that carry a large energy asymmetry have a higher probability of randomly pairing a high momentum photon and a low-momentum photon. Here we use a energy dependent asymmetry cut on π^0 of $4 < p_T < 5.25$ GeV/c in 0-40% most central events: $\alpha < 0.15 + 0.85(E_{\pi^0} - 4)^2/1.25^2$.

3.4.3 Track selection

quality cut

A detailed discussion is presented in the drift chamber section 2.2.3. In this analysis, a standard DC track quality is required for the charged tracks to be included in the hadron sample. The quality has to be either 63 or 31. Tracks with the highest quality, 63, use information from both X1 and X2 planes,

and a unique UV and PC1 hits. 31 labels the second highest quality tracks that are found using hits in X1 and X2 layers, plus a unique hit in UV plane and a non-unique hit in PC1.

n0 cut

As discussed in section 2.2.4, the RICH detector can be used for electron identification. Considering the fact that pions have a Cherenkov threshold of about 4.7 GeV/c and start to fire the RICH detector at that energy, we use a n0 cut ($n0 < 0$) to remove electrons below 5 GeV/c by requiring no hit in the RICH PMTs, in order to reject electrons from hadron sample. The loss of pions due to this cut is accounted for in the charged hadron efficiency correction.

PC3 and EMCal matching recalibration

One important role of PC3 is to reject background tracks. Positioned more than 2 meters away from the inner trackers, PC3 provide confirmation information for the tracks reconstructed using the DC and PC1, which are projected outwards according to the track model. The distance between the projected and registered PC3 hit positions allow matching the reconstructed track trajectories. Similarly one could match the track projections and the hits in the EMCal plane. This can be regarded as an alignment calibration. A recalibration of PC3 (EMcal) matching is a procedure that normalizes the differences between the track model projections from DC and hits in PC3 (EMCal). Such differences are stored in variables $pc3d\phi$, $emcd\phi$, $pc3dz$ and $emcdz$, where $d\phi$ (rad) refers to the polar angle between projected track from DC and hits in PC3/EMCal and dz is the spatial distance between the projected track and hits in PC3/EMcal plane. An example demonstrating the raw distributions of matching variables is shown in Fig. 3.18. A double Gaussian is used to fit the distribution in each p_T and zed bin, allowing for describing both the signal and background. One would observe that the background gets larger as track p_T increases, as expected according to the discussion in a previous section.

The idea of standardizing these matching variables and expressing them in terms of σ is to simplify the cuts to be implemented in the relevant analyses to select good tracks independent of track momentum, charge, centrality and so on. Therefore the recalibration should normalize out these dependencies.

In the ideal case, the distributions of these "sigmalized" variables ($pc3sd\phi$, $emcsd\phi$, $pc3sdz$ and $emcsdz$) should have a mean value of 0 and a width of 1, given the definition of $pc3sd\phi$ as an example:

$$pc3sd\phi = \frac{pc3d\phi - \langle pc3d\phi \rangle}{\sigma_{pc3d\phi}} \quad (3.16)$$

where $\langle pc3d\phi \rangle$ and $\sigma_{pc3d\phi}$ represent the mean and width of $pc3d\phi$ distribution, respectively.

The p_T and centrality dependence of the determined mean and width can be parametrized using fits. The fitting procedure is iterated until the mean and sigma values approach 0 and 1 respectively. This recalibration procedure is important for all analyses that require good central arm track selections. Fig. 3.19 and Fig. 3.20 are presented here as an example of the recalibration results: the mean and sigma values of variable $emcd\phi$ for positively charged tracks before and after calibration. One could observe that the mean has been corrected to 0 and sigma to 1, with p_T and zed dependence being accounted for. There is a slight residual after the recalibration at very low p_T . This could result from the specific fit functional forms we chose, to ensure the possibility to extrapolate the calibration to higher p_T , at the cost of not describing the low p_T dependence extremely well.

In the similar analyses presented in [80, 79], besides the commonly used quality and n0 cut, only a radial PC3 matching cut is applied when selecting charged hadron sample. For this analysis, we use an EMCAL matching for tracks when there is no PC3 acceptance, in order to extend the detector coverage and improve hadron efficiency. The effect of using this PC3 and EMCAL matching cut on reducing track background contamination is studied by plotting ratios of hadron yields with a looser cut to a tight cut, as shown in Fig. 3.21. As one could observe in the ratios, a very narrow cut as 1σ produces nearly pure charged hadrons (assuming a 0.5σ selects only real charged hadrons) since the ratio is flat across the full p_T range. The hadron sample being selected by a 1σ cut contains about a factor of 3.5 more statistics. A 2σ cut increases the sample size by almost another factor of 2 for tracks below 4 GeV/c, at a cost of a visible rise of the ratio at higher p_T , indicating some background presence. When a 3σ matching cut is used, the gain in statistics is limited compared to the introduced significant background contamination at large p_T . A 2σ cut is implemented in this analysis out of the consideration of keeping enough statistics while maintaining hadron purity.

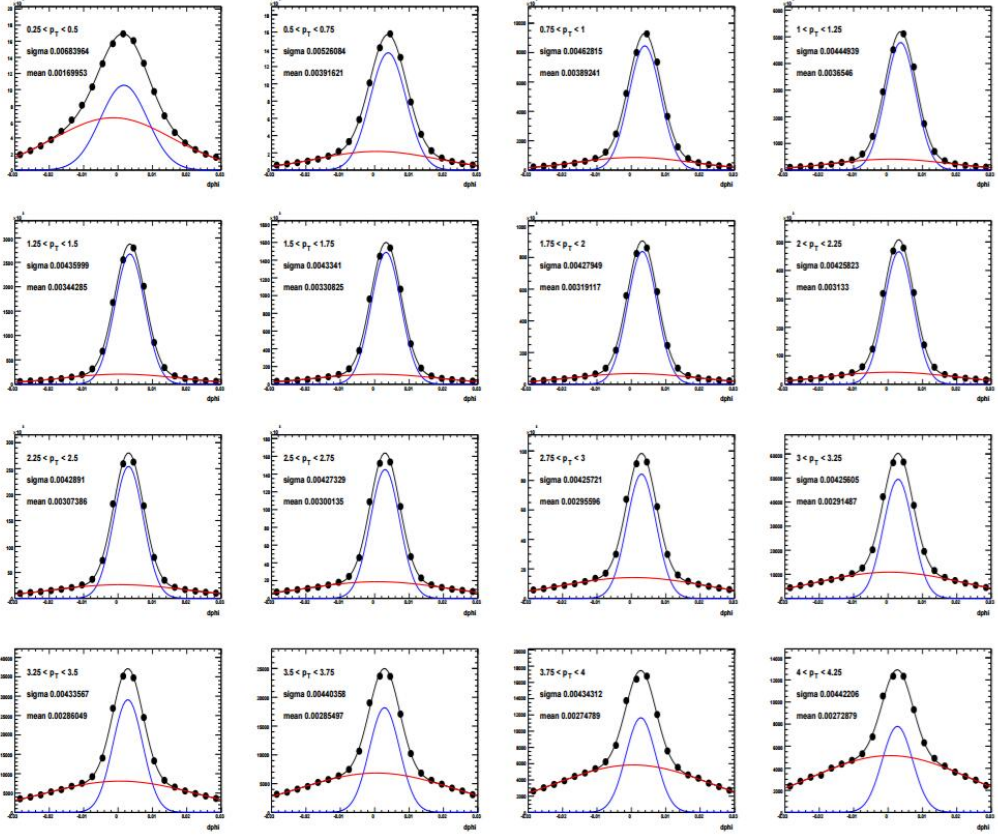


Figure 3.18: An example of $\text{emcd}\phi$ distribution for east arm for $0.25 < p_T < 4.25 \text{ GeV}/c$ positively charged tracks within $-75 < z_{\text{ed}} < -60 \text{ cm}$. A double Gaussian fit of the distribution (black) in each bin decomposes into signal (blue) and background (red).

Below is a list to summarize the requirement for particle selections:

Photon/Cluster cuts

- 3x3 EMCAL hot/dead tower map cut
- 2 tower edge cut at each EMCAL sector edge
- EMCAL fiducial cut: $|z_{\text{EMC}}| < 155 \text{ cm}$
- Shower shape cut: $\chi^2 < 3$

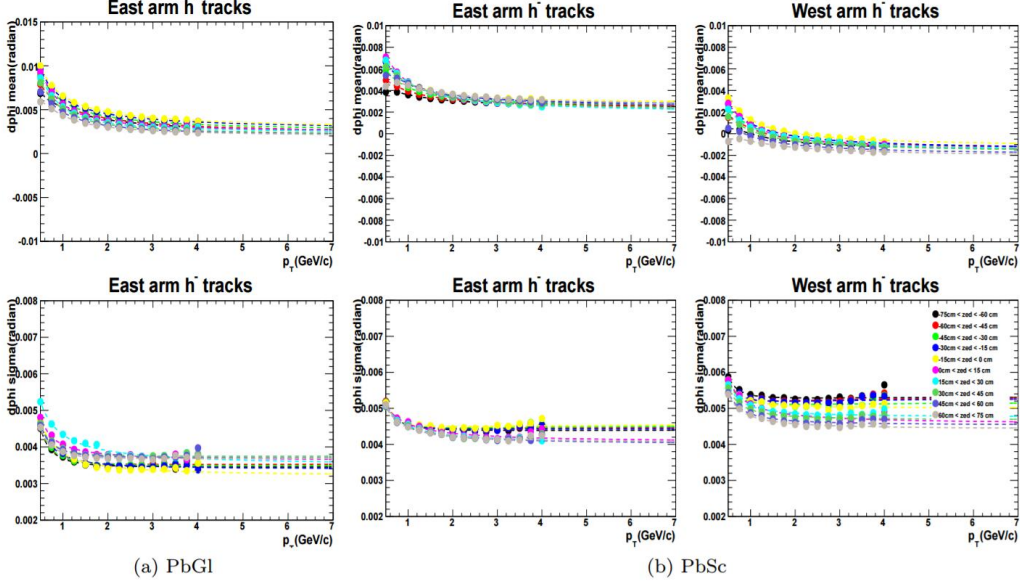


Figure 3.19: Mean (top) and sigma (bottom) of $\text{emcd}\phi$ as a function of p_T in different zed bin for positively charged tracks. Column (a) - PbGl sectors; Column (b) - PbSc.

- track based charged hadron veto cut (pair cut): $d_{min} \geq 8 \text{ cm}$

π^0 cut

For π^0 with $4 < p_T < 17 \text{ GeV}/c$: leading photons have the same cuts as the above. Both photons are required to come from the same EMCAL arm and have $E > 1 \text{ GeV}$. Photon pairs are selected to construct a π^0 according to the following requirement:

- invariant mass window: $0.12 < m_{\gamma\gamma} < 0.16 \text{ GeV}/c^2$
- $E_{\gamma 1} + E_{\gamma 2} > 4 \text{ GeV}$
- asymmetry cut for $4 < E_{\pi^0} < 5.25 \text{ GeV}$:

$$\alpha < 0.15 + 0.85(E_{\pi^0} - 4)^2/1.25^2; \alpha = \frac{|E_1 - E_2|}{E_1 + E_2}.$$

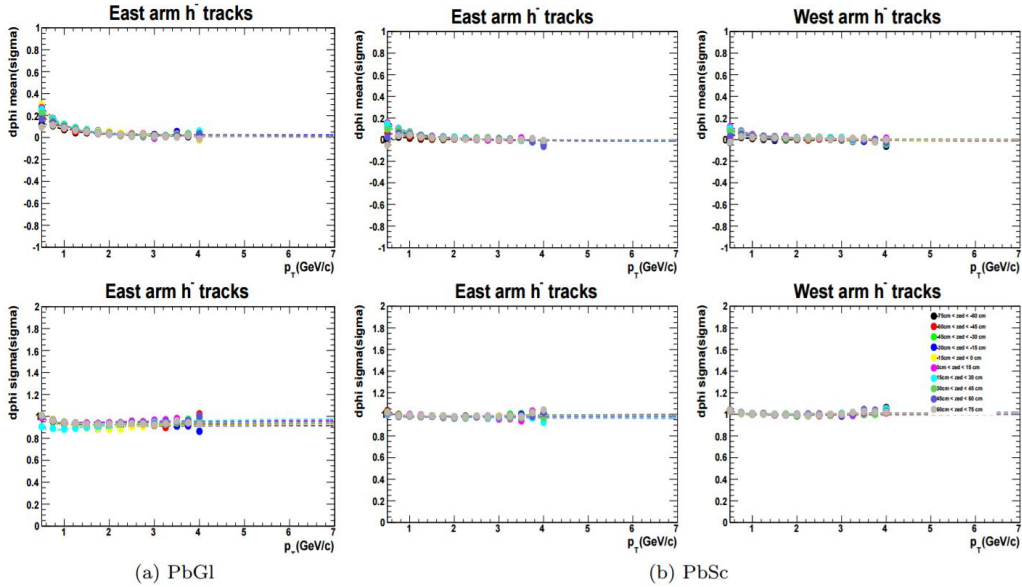


Figure 3.20: Mean (top) and sigma (bottom) of $emcsd\phi$ as a function of p_T in different zed bin for positively charged tracks. Column (a) - PbGl sectors; Column (b) - PbSc.

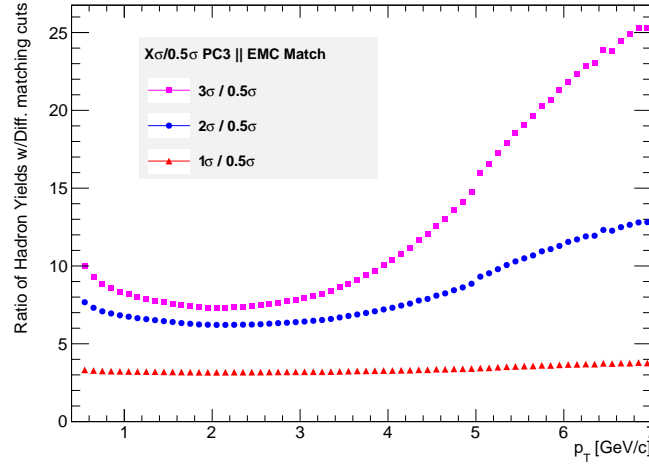


Figure 3.21: Ratios of hadron yields with different PC3/EMCal matching cut, as a function of hadron p_T . A 2σ cut is used in this analysis.

Hadron cuts

- quality == 31 || 63
- for tracks $< 5 \text{ GeV}/c$, $n_0 < 0$
- Radial PC3 and EMCal matching cut:

$$\sqrt{\sigma\phi_{pc3}^2 + \sigma z_{pc3}^2} < 2.0 \parallel \sqrt{\sigma\phi_{emc}^2 + \sigma z_{emc}^2} < 2.0$$

3.5 Charged hadron efficiency correction

For this analysis the trigger efficiency will be divided out in reporting the per-trigger yield. The charged hadron efficiency ϵ_h , however, should be included in the calculation shown in Eqn. 3.4. Single particle efficiency correction is a correction that accounts for the loss or misreconstruction of tracks due to detectors' limited acceptance, dead or inefficient areas, momentum resolution, and finite reconstruction efficiency etc. In heavy ion collisions, an additional correction referred to as the "occupancy correction" is needed to account for tracking inefficiency in high multiplicity events.

The evaluation of the single hadron acceptance \times efficiency correction is performed using a full GEANT simulation. First, as we know that the unidentified charged particles are predominantly comprised of pions, kaons and (anti)protons, we use the single particle random generator EXODUS to throw p , \bar{p} , π^\pm and K^\pm , with 50 thousand of each type. These particles are produced with a flat p_T distribution, ranging from 0 to 12 GeV/c. The acceptance coverage was chosen to fall within 0 to 2π in azimuth and -0.5 to 0.5 in pseudorapidity. Charged particles are generated using a wider acceptance and p_T range as compared to what is selected in the actual analysis in order to avoid any edge effects. The z-vertex was generated within -30 to 30 cm, as is used in the data analysis.

Next, particles are run through the PHENIX simulation package based on GEANT3, the *PHENIX Integrated Simulation Application* ("PISA"), which tracks those particles through the detectors. This simulates the detector response, as well as information about conversions and decay background particles. The output from PISA is usually referred to as a "hit file", which contains all the information each detector records as the particles traverse

the active area, provided that the subsystem is relevant and chosen to be "ON". Essentially the file is a collection of simulated event-by-event data.

Naturally, the following step is to process the PISA hit file using the standard PHENIX offline tracking and reconstruction framework. Detector configuration specific for Run-11 (i.e. drift chamber dead map) is set, in order to accurately simulate the performance. Same track selection cuts listed in the previous section 3.12.3 are applied to the simulated tracks.

The final efficiency is determined by taking a ratio of the number of final reconstructed tracks surviving all the analysis cuts to that of the initial input tracks generated from EXODUS.

Fig. 3.22 shows the resulting single charged hadron efficiency as a function of p_T for the six particle species. The efficiency is low at small p_T due to multiple scattering and also because the bending of the tracks causes them to miss PC3 and EMCAL. The kaons are observed to have a bit lower efficiency compared to pions and protons in the lower p_T range, due to their in-flight decays. A weighted average is taken to combine the different species with weights being the particle production ratios taken from [93], to reflect a realistic contribution of each particle type. The averaged efficiency distribution is separated into two p_T regions and fitted independently with the following saturated exponential function:

$$f(x) = Ae^{Bp_T} + C \quad (3.17)$$

A drop in the efficiency at around 5 GeV/c is due to the n0 cut ($n0 < 0$ for $p_T < 5$ GeV/c) that cuts into real pions as they start to fire the RICH at around 4.7 GeV/c. That is why the region $3 < p_T < 5$ GeV/c is separately fitted. The uncertainty on the fitting is taken and propagated as one source of systematic uncertainties.

In order to account for the multiplicity effect on the tracking efficiency, an additional correction is needed. An embedding technique is typically used for this occupancy correction. With one simulated track embedded in a real event before reconstruction, one then calculates the efficiency by comparing the reconstructed true track with embedding and without, the latter represents the scenario with no occupancy effects. The occupancy correction that is implemented in this analysis uses the values reported in these studies [79, 80].

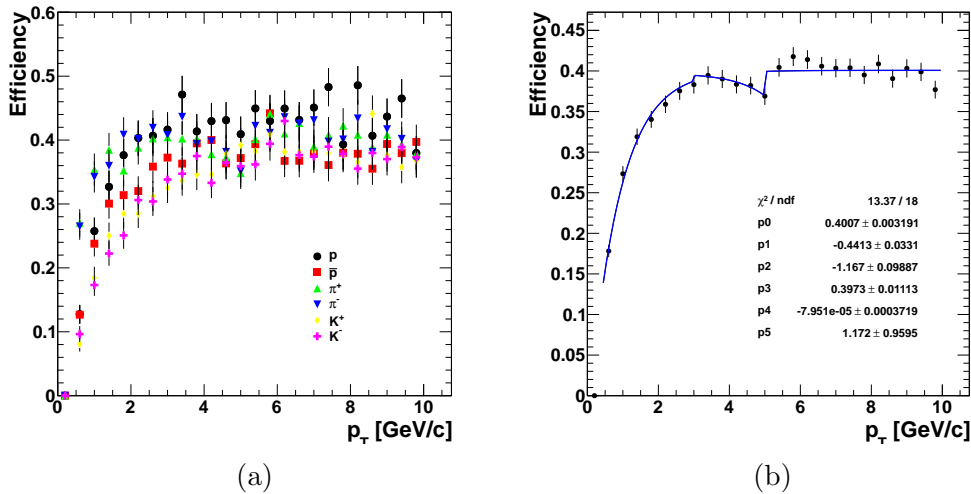


Figure 3.22: Single hadron acceptance \times efficiency determined for p_*/π^\pm , K^\pm (a) and particle type averaged (b) from simulation.

3.6 π^0 efficiency correction

The π^0 efficiency is determined by scaling the measured raw π^0 spectra to a power law fit to data published in [78]. A strict asymmetry cut was applied in the two most central bins to ensure a clean sample. The efficiency for π^0 s cancels out when calculating the conditional yield of hadrons per trigger. Therefore Fig. 3.23 is plotted in arbitrary normalization units, as only the shapes matter. The π^0 efficiency is needed together with the decay probability weighting function (see discussion in section 3.7.2) to properly map the measured $\pi^0 - h$ correlations to the $\gamma_{dec} - h$ correlations for statistical subtraction.

3.7 Statistical Subtraction Method

The direct photon-hadron correlations were determined by statistical subtraction of measured decay photon-hadron correlations from the inclusive photon-hadron correlations. This is the same analysis approach used in both p+p and Au+Au [76, 74]. The definition of direct photons may vary with the focus of different analyses. For this analysis, direct photon refers to any

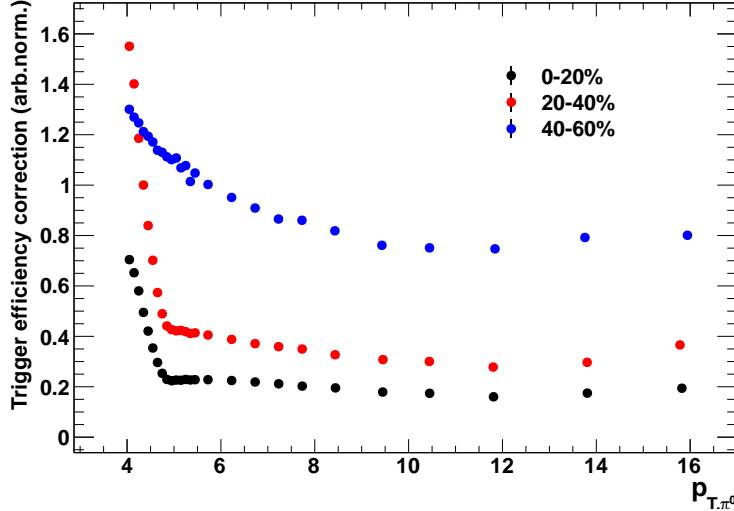


Figure 3.23: π^0 efficiency for 0-20% (black), 20-40% (red) and 40-60% (blue) centrality classes.

photon that is not coming from a decay process. For $p_T > 5$ GeV/c, direct photons consist primarily of prompt and fragmentation photons. The relative contribution of direct versus decay photons varies with p_T and centrality.

We can write down the following equation relating the number of triggers and the per-trigger yield for each component:

$$N_{inc}^\gamma Y_{inc} = N_{dec}^\gamma Y_{dec} + N_{dir}^\gamma Y_{dir} \quad (3.18)$$

where inc, dec, dir denote inclusive, decay and direct, respectively; N stands for the number of triggers of each type; Y means per-trigger yield associated with a particular type of triggers. These notations will be used repeatedly in the following sections.

The inclusive yield of hadrons per trigger photon can be expressed as the weighted sum of direct and decay components as follows:

$$Y_{inc} = \frac{N_{dir}^\gamma}{N_{inc}^\gamma} Y_{dir} + \frac{N_{dec}^\gamma}{N_{inc}^\gamma} Y_{dec} \quad (3.19)$$

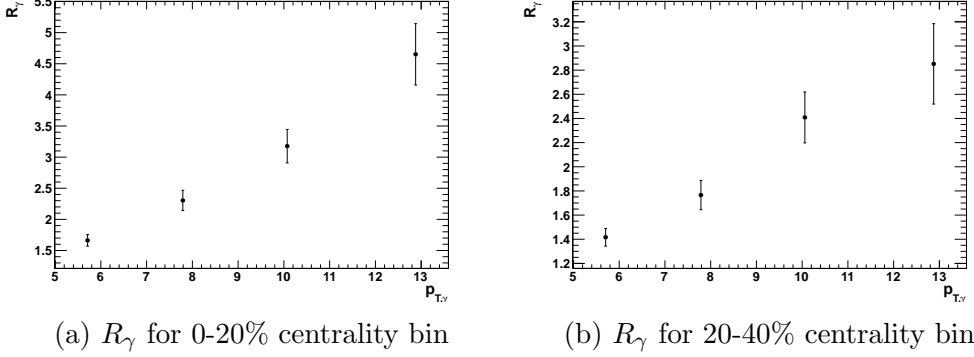


Figure 3.24: R_γ input used in this analysis. These are determined from a separate analysis and rebinned for the current analysis. The error bars showing here include both statistical and systematic uncertainties.

The weighting factors can be expressed in terms of the double ratio observable R_γ [77],

$$R_\gamma = \frac{N_{inc}^\gamma}{N_{dec}^\gamma} = 1 + \frac{N_{dir}^\gamma}{N_{dec}^\gamma} \quad (3.20)$$

The yield per direct photon can then be calculated via:

$$Y_{dir} = \frac{R_\gamma Y_{inc} - Y_{dec}}{R_\gamma - 1} \quad (3.21)$$

3.7.1 R_γ

The R_γ values used in this analysis are measured independently [77]. That particular analysis used Run-4 Au+Au data and results are determined using PbSc and PbGl clusters separately. The values are combined using a weighted average method and then rebinned into trigger p_T and centrality bins to match the ranges we use in the current analysis. Fig. 3.24 shows the R_γ values used for 0-20% and 20%-40% in this analysis.

3.7.2 Decay Mapping

The background of hadron yields associated with decay photons is estimated using a Monte Carlo pair-by-pair mapping procedure. A detailed description of the method can be found in [86] and the main points are discussed here. Since the dominant decay contribution comes from $\pi \rightarrow \gamma\gamma$, the simulation calculates the probability of getting photons from decay (or $\gamma_{dec} - h$ pairs) within a certain photon p_T range from the measured π^0 (or $\pi^0 - h$ pair) yields. A small correction is then applied to include the higher mass meson decay contribution. The actual mapping involves counting γ_{dec} -h pairs (or decay photons) via a weighted summation over all individual π^0 -h pairs (π^0 s), where the weighting factor reflects the kinematic probability that a π^0 at a given p_T will decay into a photon in a selected p_T range.

If we denote $P(p_T^{\pi^0} \rightarrow p_T^\gamma)$ as the probability of a π^0 with transverse momentum $p_T^{\pi^0}$ to decay into a photon of p_T^γ , the decay photon (or decay photon-hadron) yields can be converted from that of π^0 (or π^0 -h) using the probability function:

$$\frac{dN^{\gamma(-h)}}{dp_T^{\gamma(-h)}} = \int dp_T^{\pi^0} P(p_T^{\pi^0} \rightarrow p_T^\gamma) \frac{dN^{\pi^0(-h)}}{dp_T^{\pi^0(-h)}} \quad (3.22)$$

The integration range lies within 4-17 GeV/c to yield decay photons of 5-15 GeV/c. The effect of truncating the π^0 p_T at 17 GeV/c will be discussed in the following section.

Because the probability of getting a decay photon of $0 < E^\gamma < p_T^{\pi^0}$ is uniform and gets smaller as the decay phase space increases, it can be written as $2/E^{\pi^0}$, taking into account the effect of the two-body decay (where the factor of 2 comes from). At the ultra-relativistic limit $p_T^\gamma \approx E^\gamma$ measured in the EMCal. The probability to yield a decay photon (or a $\gamma_{dec} - h$ pair with triggers) of $a < p_T^\gamma < b$ can be expressed in the form below:

$$P(p_T^{\pi^0} \rightarrow p_{T,a-b}^\gamma) = \int_a^b \frac{2}{p_T^{\pi^0}} dp_T^\gamma \quad (3.23)$$

Considering three types of scenarios regarding different $p_T^{\pi^0}$ gives the following analytical form of the probability function for yielding a decay photon within a momentum range of $a < p_T^\gamma < b$ from a π^0 of $p_T^{\pi^0}$:

$$P(p_T^{\pi^0} \rightarrow p_T^\gamma_{a-b}) = \begin{cases} 0 & , p_T^{\pi^0} < a \\ \int_a^{p_T^{\pi^0}} dp_T^\gamma \frac{2}{p_T^{\pi^0}} = 2(1 - \frac{a}{p_T^{\pi^0}}) & , a < p_T^{\pi^0} < b \\ \int_a^b dp_T^\gamma \frac{2}{p_T^{\pi^0}} = 2(\frac{b-a}{p_T^{\pi^0}}) & , p_T^{\pi^0} > b \end{cases} \quad (3.24)$$

In Fig. 3.25 the solid black line represents the probability distribution for a π^0 to decay into a photon of $5 < p_T < 7$ GeV/c, as a function of the parent π^0 p_T . The shape earns the probability function a nickname "the shark fin", due to the overall resemblance.

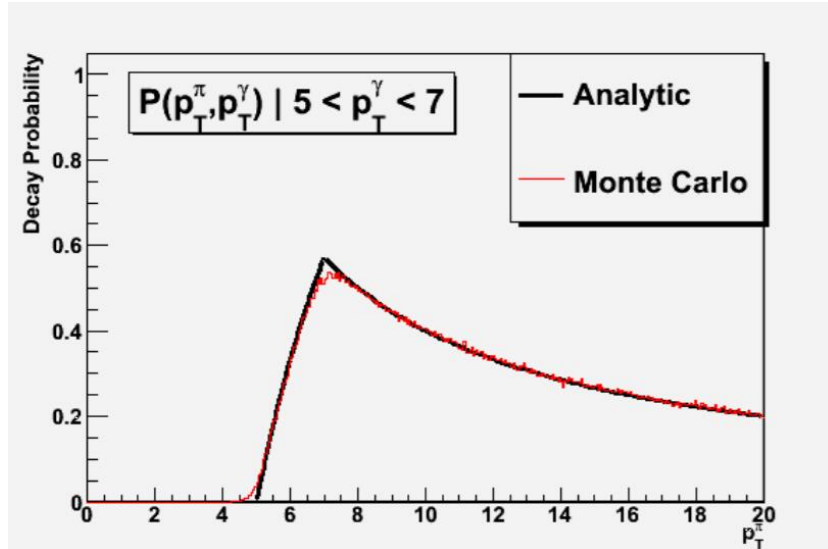


Figure 3.25: A "shark fin": probability function for a π^0 to decay into a photon of $5 < p_T < 7$ GeV/c, as a function of the parent π^0 p_T . The black solid line represents the analytical calculation, as compared to the red curve demonstrating the simulation result.

Experimentally, the probability function is determined from Monte Carlo simulation. First, the π^0 reconstruction efficiency is corrected, and the true decay photons are obtained according to the decay kinematics. Secondly, the specific detector effect (namely the EMCAL response including acceptance, energy and position resolution) is taken into account, so that the efficiency

of getting decay photons (or $\gamma_{dec} - h$ pairs) can be generated as realistic as possible, producing decay photons that would actually be detected in the EMCAL.

For high energy π^0 s, the opening angle between the two decay photon pairs is small. The resulting clusters in the EMCAL could not be well separated, so they are removed from the initial inclusive photon sample by the shower shape cut. The loss of photons caused by this merging effect at high p_T is unaccounted for in the MC simulation. Instead the efficiency to detect photons from a high momentum parent meson is calculated from a GEANT simulation. This is then included in the probability function as an additional correction. Due to the reconstruction efficiency dependence on $\pi^0 p_T$, the probability function is determined in separate p_T bins. Also studied and accounted for is the dependence on z_{EMC} . An example is shown in Fig. 3.26. The decay probability is lower for π^0 near the edge of the detector, due to the fact that the daughter photons are likely to fall outside the acceptance. Therefore those π^0 are less likely to produce a photon compared to the ones closer to the center of the detector.

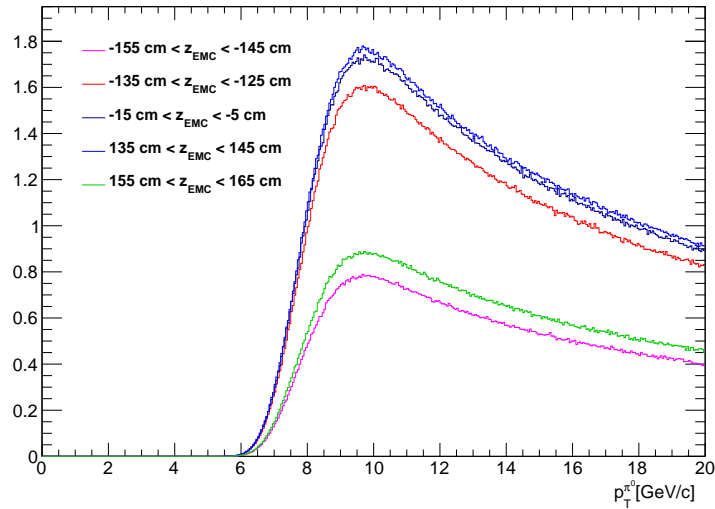


Figure 3.26: Probability for a π^0 to decay into a $7 < p_T^\gamma < 9$ GeV/c photon for a few different z_{EMC} bins.

A simulated "shark fin" is also shown in Fig. 3.25, as a comparison to the analytical calculation. The two curves agree well across the whole p_T range,

with the simulation curves being more smooth around the peak and the lower edge of the distribution due to detector finite resolution. The smearing at 5 GeV/c is taken into consideration by reconstructing π^0 down to 4 GeV/c in the analysis.

After obtaining the probability function, the charged hadron triggered by decay photons within $a < p_T^\gamma < b$ is given as:

$$Y_{dec} = \frac{N_{a-b}^{\gamma-h}}{N_{a-b}^\gamma} = \frac{\int \epsilon_{\pi^0}^{-1} P(p_{T\pi^0} \rightarrow p_{T\gamma}) N_{\pi^0-h} dp_{T\pi^0}}{\int \epsilon_{\pi^0}^{-1} P(p_{T\pi^0} \rightarrow p_{T\gamma}) N_{\pi^0} dp_{T\pi^0}} \quad (3.25)$$

Looping through reconstructed π^0 s and adding up the number of the resulting decay photons or $\gamma_{dec} - h$ pairs within a certain momentum range $a < p_T^\gamma < b$ gives:

$$N_{a-b}^{\gamma(-h)} = \sum_i^{N^{\pi^0-h}} \epsilon_{\pi^0}^{-1} P(p_{Ti}^{\pi^0} \rightarrow p_{T,a-b}^\gamma) \quad (3.26)$$

Equation (25) is then equivalent to the following:

$$Y_{dec} = \frac{\sum_i^{N^{\pi^0-h}} \epsilon_{\pi^0}^{-1}(p_{Ti}^{\pi^0}) P_{a-b}(p_{Ti}^{\pi^0}, z_{EMCi}^{\pi^0})}{\sum_i^{N^{\pi^0}} \epsilon_{\pi^0}^{-1}(p_{Ti}^{\pi^0}) P_{a-b}(p_{Ti}^{\pi^0}, z_{EMCi}^{\pi^0})} \quad (3.27)$$

where $P_{a-b}(p_{Ti}^{\pi^0}, z_{EMCi}^{\pi^0})$ represents the probability of a π^0 with transverse momentum $p_{Ti}^{\pi^0}$ and position z_{EMC} along the z direction in the EMCAL, to decay into photons within momentum range of $a < p_T < b$. $\epsilon_{\pi^0}(p_T^{\pi^0})$ is the π^0 reconstruction efficiency discussed above.

3.7.3 π^0 cutoff correction

When constructing π^0 -h pairs, π^0 are selected within a p_T range of 4-17 GeV/c. The lower bound is chosen to include the detector resolution when populating decay photon p_T bin probabilities. The upper bound is selected to minimize the merging effect at high p_T , as well as to reduce the uncertainty in the later statistical subtraction step, since statistics are very low at large p_T . Since π^0 with p_T larger than 17 GeV/c will also contribute to the decay photon p_T bins, a correction to the $\gamma_{dec} - h$ yields due to the π^0 momentum

cutoff is applied. This correction is evaluated using a power law fit to the measured π^0 spectra for different associated hadron p_T bins. The fits are used to determine the cutoff correction C_{cutoff} by calculating the yield deficiency D_{cutoff} according to:

$$D_{cutoff} = 1/C_{cutoff} = \frac{\int_{<17} dp_T^{\pi^0-h} P(p_T^{\pi^0-h}) \frac{dN^{\pi^0-h}}{dp_T^{\pi^0-h}} / \int_{<\infty} dp_T^{\pi^0-h} P(p_T^{\pi^0-h}) dp_T^{\pi^0-h}}{\int_{<17} dp_T^{\pi^0} P(p_T^{\pi^0}) \frac{dN^{\pi^0}}{dp_T^{\pi^0}} / \int_{<\infty} dp_T^{\pi^0} P(p_T^{\pi^0}) dp_T^{\pi^0}} \quad (3.28)$$

The values used in this analysis is tableted in Table 3.3.

p_T^γ (GeV/c)	p_T^h (GeV/c)	Correction
5-7	0.5-1	1.0
	1-2	1.0
	2-3	1.0
	3-5	0.998
	5-7	0.994
7-9	0.5-1	0.998
	1-2	0.998
	2-3	0.996
	3-5	0.992
	5-7	0.977
9-12	0.5-1	0.993
	1-2	0.993
	2-3	0.983
	3-5	0.969
	5-7	0.930
12-15	0.5-1	0.977
	1-2	0.977
	2-3	0.944
	3-5	0.908
	5-7	0.825

Table 3.3: Cutoff correction for π^0

3.8 Fill-time method for ξ binned results

We aim to quantify the medium modification of the jet fragmentation function in Au+Au collisions, compared to p+p. The jet fragmentation function describes the probability of an outgoing parton to yield a hadron with momentum fraction $z = p_{\text{hadron}}/p_{\text{parton}}$. Since, at leading order, the momentum of the trigger photon balances that of the opposing parton, variables $z_T = p_T^h/p_T^\gamma$ or $\xi = \ln(1/z_T)$ are often used. It is most intuitive to analyze the data in bins of hadron p_T , as reconstruction efficiency and acceptance effects depend on p_T , rather than z_T or ξ . Converting results in p_T bins into ξ bins results in overlapping points which would need to be combined. It is more straightforward to bin all pair $\Delta\phi$ histograms in ξ from the very beginning. We implemented the fill-time method, as was used in previous analyses [80, 92]. This method applies acceptance and efficiency corrections (which are hadron p_T dependent) as weights event-by-event when filling the pair $\Delta\phi$ distributions at the analysis level. We measure the acceptance by constructing $\Delta\phi$ distributions of pairs from mixed events in a first pass over the data. In the second pass, we use the mixed event results to correct for acceptance.

The following equations demonstrate how to extract jet signals using a standard fill-time weighting procedure, according to the two-source model. Note that A and B denote triggers and partners respectively.

$$\frac{dN^{AB}(\Delta\phi)}{N^A d\Delta\phi} = \frac{dN^{AB}(\Delta\phi)}{N^A \epsilon^B d\Delta\phi} \text{Acc}(\Delta\phi)^{-1} - b'_0 (1 + v_2^A v_2^B \cos(2\Delta\phi)) \frac{dN_{\text{mix}}^{AB}(\Delta\phi)}{N_{\text{mix}}^A \epsilon^B d\Delta\phi} \text{Acc}(\Delta\phi)^{-1} \quad (3.29)$$

The first term on the right side of the equation is the foreground weighted by the charged hadron efficiency and an acceptance correction obtained from a first pass over the data, as noted above. The second term describes the background weighted by efficiency and acceptance correction, as well as the flow modulation. Lastly, the division of number of triggers (N_A) and the multiplicity correction factor denoted as b'_0 here (previously denoted as ξ in section 3.3.1) are included in the subtraction after taxi process. The normalized acceptance function is given by:

$$\text{Acc}(\Delta\phi) = \frac{\pi \frac{dN_{\text{mix}}^{AB}(\Delta\phi)}{d\Delta\phi}}{\int d\Delta\phi \frac{dN_{\text{mix}}^{AB}(\Delta\phi)}{d\Delta\phi}} \quad (3.30)$$

In order to extract jet signals, the per trigger yield of hadrons is determined by subtracting background pairs coming from uncorrelated pairs from all pairs. This is applied to calculate $\gamma_{inc}\text{-}h$, $\pi^0\text{-}h$ and decay $\gamma_{dec}\text{-}h$ jet pair yields.

During code implementation, we observed that the assumption that hadron efficiency correction and acceptance correction factorization does not entirely hold. Distortions of the $\Delta\phi$ distributions were observed when using weights from the above equations, especially in the lower hadron p_T (higher ξ) bins (Fig. 3.27). Consequently, a modified fill-time method is used. This includes the effect of hadron efficiency correction on the acceptance in the first pass over the data to construct the mixed pair $\Delta\phi$ distribution. The equation below demonstrates the modified acceptance function.

$$Acc'(\Delta\phi) = \frac{\pi \frac{dN_{mix}^{AB}(\Delta\phi)}{d\Delta\phi}}{\int d\Delta\phi \frac{dN_{mix}^{AB}(\Delta\phi)}{\epsilon^B d\Delta\phi}} \quad (3.31)$$

With applying modified acceptance correction, we are able to get smooth foreground and background $\Delta\phi$ distributions. The outcome is compared with a non-weighting analysis. The good agreement suggests that the weighting method is working properly. See Fig. 3.28 and Fig. 3.29.

We have discussed how the p_T dependent v_2 values are implemented for the p_T binned results. To get ξ binned results, We use an interpolation procedure to estimate a continuous function for $v_2(p_T)$ to be used in the weights. Since the decay weighting is performed for discrete bins, it is reasonable to use the measured trigger v_2 in those same bins. Fig. 3.30 illustrates the v_2 values evaluated for weighting hadrons in the 0-20% centrality bin.

3.9 Effect of increased conversions in Run-11 on results or R_γ

Run-11 data were taken with the VTX detector installed, causing a higher photon conversion probability than in Run-10 and Run-7. The question came up whether the increased conversion probability requires a change in the value of R_γ for the statistical subtraction. In principle, it should not, as the loss of photons to conversion should cancel when taking the per trigger yield of

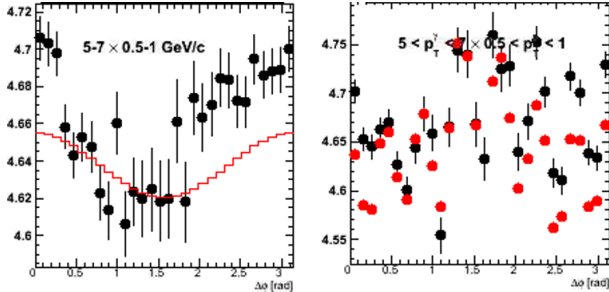


Figure 3.27: Distortions observed in foreground (black) and background (red) $\Delta\phi$ distributions for lower associate hadron p_T bins, before modifying fill-time weights, compared to the left (no weighting case).

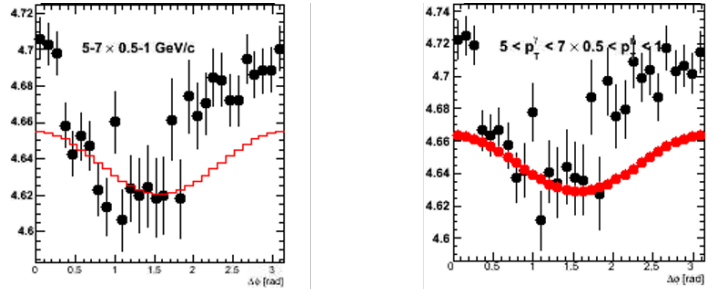


Figure 3.28: Left: inclusive photon-hadron foreground (black) and background (red) in no weighting case; Right: weighting case. This is an example for trigger 5-7 GeV/c and associate partner in 0.5-1 GeV/c.

associated hadrons. R_γ is a physics quantity and should be the same if losses are properly accounted for. Nevertheless, a study was done to investigate whether the final jet functions are sensitive to the photon conversions.

Two ratios were constructed and compared to the same ratios in Run-10. The first was the ratio of the inclusive photon-hadron jet function to the π^0 -hadron jet functions. The second was the ratio of the inclusive photon-hadron jet function to the decay photon-hadron jet function. Both ratios were compared to run-10 by constructing a double ratio $\frac{Run-10}{Run-11}$, and found to be consistent with 1. This double ratio and the χ^2 test is carried out for each trigger p_T and associated hadron p_T bin. Fig. 3.31 shows an example for 5-7 GeV triggers correlated with charged hadrons within 0.5-1 GeV/c bin in 0-20% centrality bin. Fig. 3.32 is the χ^2 distribution and the corresponding p value distributions for all the studied trigger and partner p_T bins in 0-20%

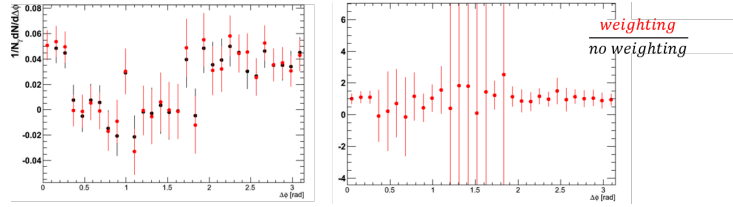


Figure 3.29: An example demonstrating background subtracted inclusive photon-hadron yields using weighting method (red) and no weighting (black) and their ratio.

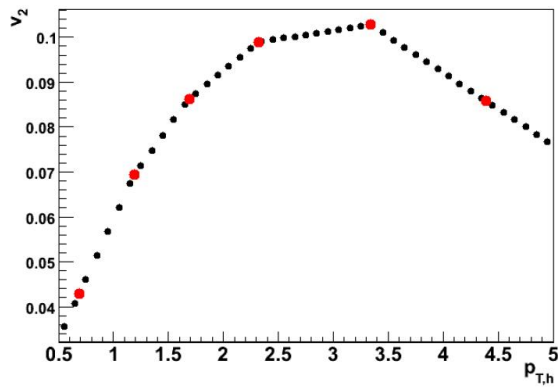


Figure 3.30: A demonstration of v_2 implementation in fill-time weighting procedure. The red points stand for the measured 0-20% hadron v_2 in each p_T bin, the weights are taken from the interpolation between these points.

centrality bin.

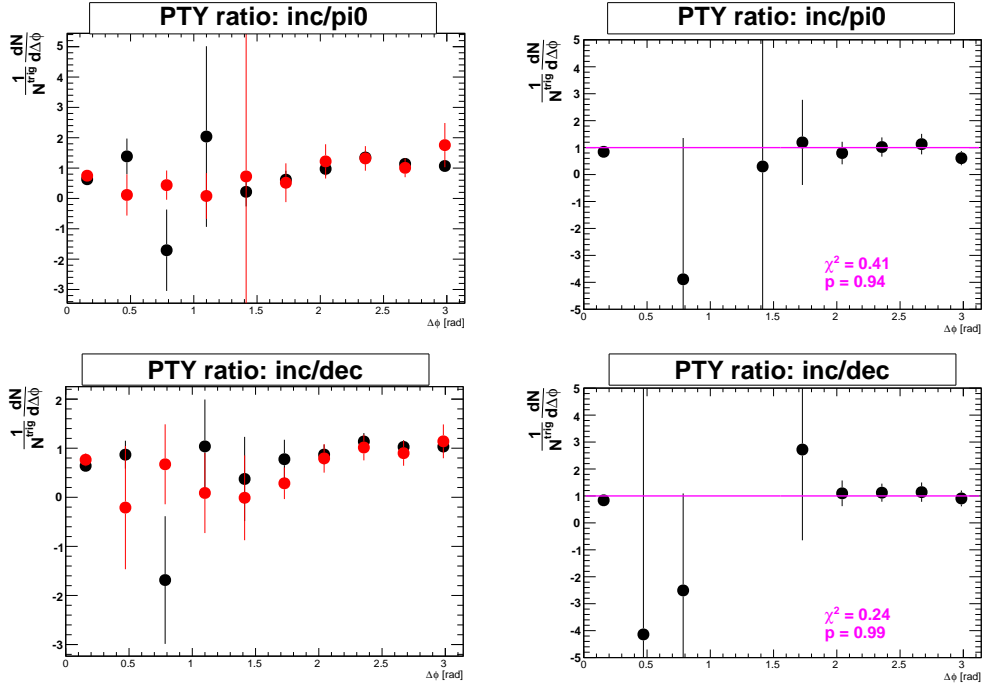


Figure 3.31: The upper two panels show ratios of inclusive photon-hadron to π^0 -hadron jet functions in Run-11 (Red) and Run-10 (Black) and the double ratio (Run-10/Run-11). The jet functions presented here are the per-trigger yield (PTY). The lower two panels show ratios of inclusive photon-hadron to decay photon-hadron jet functions in Run-11 (Red) and Run-10 (Black) and the double ratio (Run-10/Run-11). The double ratios on the right are compared to 1 and a χ^2 test is done. This example is for 5-7 GeV triggers correlated with charged hadrons within 0.5-1 GeV/c bin in 0-20% centrality bin.

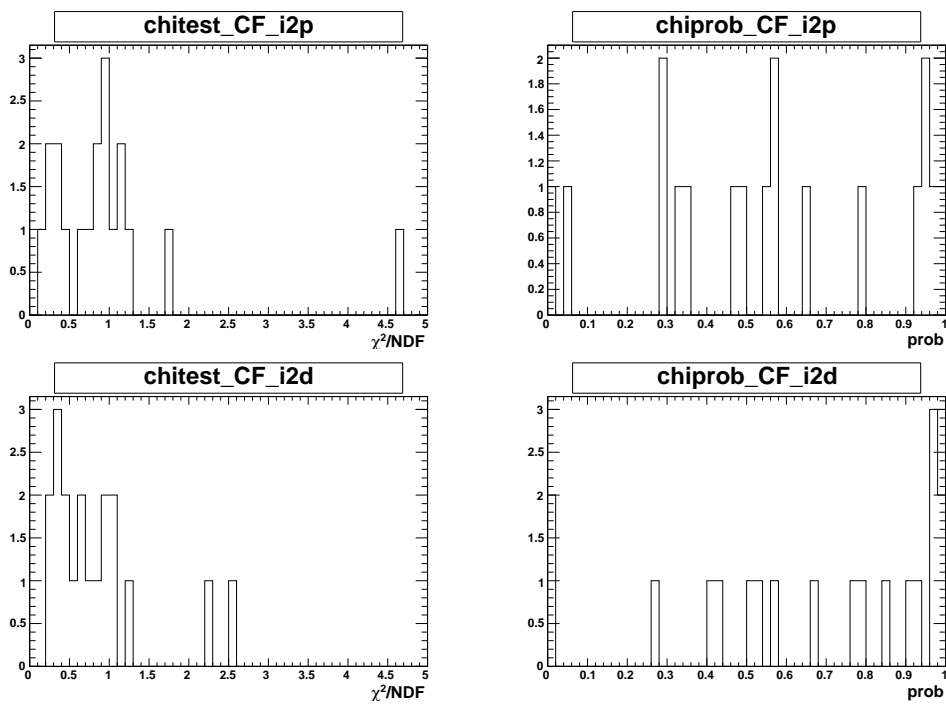


Figure 3.32: χ^2 test results on conversion effect: ratios of inclusive γ -h over π^0 -h or decay γ -h between run11 and run10 are consistent with 1.

Chapter 4

Uncertainties

In this chapter, a discussion of the systematic uncertainties in this analysis will be outlined. Since the final Au+Au direct photon-hadron correlation results are presented in the form of combined statistics from Run-7 + Run-10 + Run-11, the uncertainty propagation involved in the combining process will also be described.

There are several sources of systematic uncertainties in this analysis. The uncertainty in the subtraction method is dominated by the statistical and systematic errors of R_γ . There are also uncertainties on jet function extraction due to the uncertainties on the v_2 measurement. The absolute normalization method and the determination of decay photon-hadron correlations also contribute to the overall systematic uncertainties. Uncertainty from hadron efficiency determination comes in as a global scale uncertainty.

Each source of uncertainty contributes differently to the final systematic uncertainty on the measurement of direct photon triggered hadron yields. Since the signal-to-background ratio is low at lower hadron p_T bins (high ξ bins) and since statistics are limited at higher hadron p_T bins (low ξ bins), different sources of uncertainty dominate in different kinematic ranges. For lower hadron p_T , since the combinatorial background is high, the determination of the background level and measurement of v_2 modulation is crucial. The dominant uncertainties in this region come from v_2 and ABS method. For higher trigger p_T , the leading uncertainty comes from the measurement of R_γ , due to the fact that both statistical and systematic uncertainties are larger at higher p_T for R_γ . Uncertainty from the determination of decay photon-hadron correlations is high for lower p_T triggers because the combinatorial background under the π^0 invariant mass peaks is higher. The global

scale uncertainty is not included in the plots since it contributes as a constant percentage across all p_T ranges.

4.1 Uncertainty Propagation

In this analysis, all statistical uncertainties are propagated using the following general formula, in which the quantity y is a function of variables x_1, x_2, \dots, x_n : $y = f(x_1, x_2, \dots, x_n)$. The uncertainty on y is calculated as the following [94]:

$$\Delta y = \sqrt{\left(\frac{\partial y}{\partial x_1} \Delta x_1\right)^2 + \left(\frac{\partial y}{\partial x_2} \Delta x_2\right)^2 + \dots + \left(\frac{\partial y}{\partial x_n} \Delta x_n\right)^2} \quad (4.1)$$

The systematic uncertainty on the final direct photon triggered hadron yields has contributions from a variety sources, which will be discussed further in the following sections. The effect of the systematic error from each source is estimated by varying the input value by the uncertainty on that particular source to obtain the upper and lower bound of the measured quantity accordingly. The relative error δ_i of y arising from uncertainty on x_i is evaluated as the following:

$$y\delta y_i = \frac{1}{2} \left(\left| \frac{f(x_1, \dots, x_i + \delta_i, \dots) - f(x_1, x_2, \dots, x_n)}{f(x_1, x_2, \dots, x_n)} \right| - \left| \frac{f(x_1, \dots, x_i - \delta_i, \dots) - f(x_1, x_2, \dots, x_n)}{f(x_1, x_2, \dots, x_n)} \right| \right) \quad (4.2)$$

The total systematic uncertainty on the measured yield can then be calculated taking the quadratic sum of all the contributions:

$$\Delta y_{sys} = \sqrt{\sum_i (y\delta y_i)^2} \quad (4.3)$$

where δy_i represents the uncertainty carried by the i^{th} source that contributes to the final systematic uncertainties.

Any uncorrelated components of the systematic uncertainty are summed in quadrature with the statistical uncertainty.

The systematic uncertainty on the I_{AA} is given by the spread resulting from the upper and lower bounds of the uncertainties on the Au+Au and p+p per-trigger yields, when taking the ratio Y_{AA}/Y_{pp} .

4.2 R_γ and Statistical Subtraction

The R_γ input for statistical subtraction is discussed in section 3.7.1. R_γ is determined from a separate and independent analysis of the ratio of inclusive and decay photons in Run-4 Au+Au collisions [77]. Defined as a ratio of the number of inclusive photons to decay photons, the measured R_γ is larger than unity, indicating the presence of direct photons. R_γ is a physics quantity and does not change with runs. It can thus be used directly as an input in this analysis. Fig. 3.24 shows the R_γ values for 0-40% most central Au+Au data used for the statistical subtraction in this analysis. R_γ increases with centrality (larger R_γ values for more central Au+Au events). This is due to π^0 and higher mass mesons being suppressed, therefore producing fewer decay photons in more central collisions. The uncertainties on the R_γ shown in Fig. 3.24 includes both the statistical and systematic components, each listed in table 4.1. Both statistical and systematic uncertainties increase with the photon p_T .

The main contributions to the systematic uncertainty in the R_γ measurement are the energy scale of the calorimeters, π^0 extraction, additional sources to the decay photon yield and the merging effect for clusters energy larger than 10 GeV [49]. The uncertainties in this measurement coming from R_γ are correlated in p_T , given the fact that R_γ changes with photon p_T . The statistical uncertainty from the R_γ measurement, however, results in uncorrelated uncertainties across the different trigger p_T bins.

Centrality (%)	p_T^γ (GeV/c)	R_γ	Stat.	Sys.
0-20%	5-7	1.662	0.008	0.092
	7-9	2.304	0.021	0.162
	9-12	3.176	0.056	0.263
	12-15	4.651	0.221	0.440
20-40%	5-7	1.416	0.009	0.073
	7-9	1.766	0.021	0.119
	9-12	2.408	0.060	0.202
	12-15	2.852	0.204	0.263

Table 4.1: R_γ values and statistical and systematic uncertainties

4.3 Decay Mapping

The uncertainty due to π^0 combinatorial background subtraction is the main contribution to uncertainties in the determination of decay photon triggered hadron yields. As discussed in section 3.4.2, π^0 are reconstructed by pairing photons and selecting those that fall in a certain π^0 invariant mass window. The previously discussed analysis cuts, such as the asymmetry cut and invariant mass cut, are imposed on the leading and the pair photons to cut down on random pairing so the combinatorial pair background is reduced. However the measured π^0 still contain a mixture of real signals and combinatorial background. The background decreases as $\pi^0 p_T$ increases because there are fewer photons at high p_T .

The following equation expresses the measured $\pi^0 - h$ per trigger yield in terms of a combination of hadron yields associated with real and false π^0 s:

$$Y_{meas} = \frac{1}{N_{trig}}(N_{bg}Y_{bg} + N_{sig}Y_{true}) \quad (4.4)$$

where Y_{true} is the signal of hadron yields triggered by real π^0 s and Y_{bg} represents the background yields. N_{sig} and N_{bg} stand for the number of real and background π^0 's, respectively. N_{trig} is the total number of π^0 triggers and can be broken down into the following:

$$N_{trig} = N_{sig} + N_{bg} \quad (4.5)$$

We define the uncertainty on the π^0 combinatorics as:

$$\sigma_{comb}^{\pi^0} = \frac{Y_{true} - Y_{meas}}{Y_{meas}} \quad (4.6)$$

In order to measure $\sigma_{comb}^{\pi^0}$ we can write out the signal-to-background ratio definition as $S/B = N_{sig}/N_{bg}$ and plug in Eqn 4.4. After some rearrangement we get:

$$\sigma_{comb}^{\pi^0} = \frac{1 - Y_{bg}/Y_{meas}}{S/B} \quad (4.7)$$

Fig. 4.1 and 4.2 are π^0 's signal-to background ratios calculated for 4 trigger p_T bins in 0-20% and 20-40% centrality bins. After fitting each π^0 mass peak using a Gaussian + polynomial functional form, the S/B is determined by taking the ratio of the integral under Gaussian peak only to the integral

under the polynomial within 2σ of the fitted mass peak. The invariant mass fitting ranges and the corresponding extracted S/B values are listed in each panel.

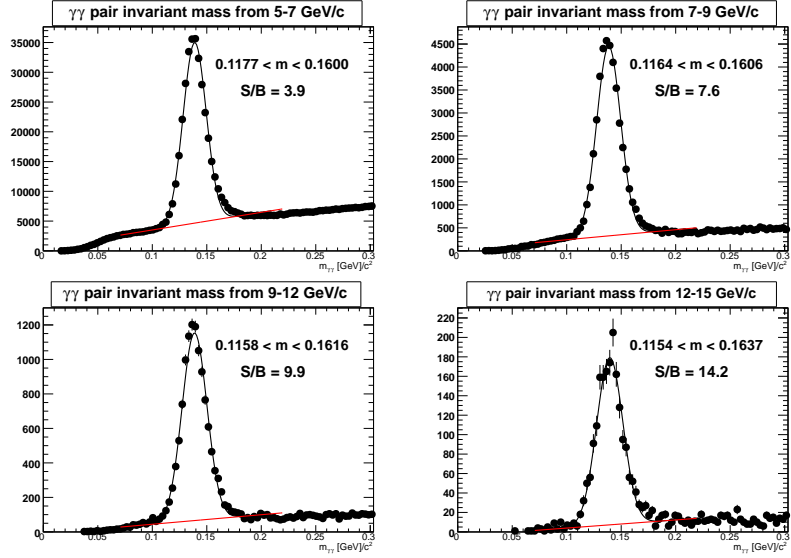


Figure 4.1: π^0 invariant mass peaks and signal-to-background ratios for 0-20% centrality class. The four panels corresponds to four π^0 p_T trigger bins.

According to Eqn 4.7, besides the S/B, Y_{bg}/Y_{meas} must be measured to determine $\sigma_{comb}^{\pi^0}$. Y_{meas} is the measured $\pi^0 - h$ yield. Y_{bg} can be determined using two methods. The first method is a side-band analysis, which is a typical way to determine Y_{bg} . It is carried out by measuring charged hadron yields that are associated with the "background π^0 's", as opposed to using measured reconstructed π^0 's as triggers. The background π^0 's are selected as those 2σ away from the mean position of the π^0 invariant mass peak. This can be used as an estimate of the combinatorial background under the π^0 mass peak, which are not subtracted when reconstructing and selecting π^0 's within 2σ . In the ideal case, the measured background π^0 -h yields should be zero, as there should not be any physical correlations between "fake π^0 's" and hadrons. Y_{bg} being zero is equivalent to $Y_{bg}/Y_{meas} = 2$ when calculating the error on π^0 combinatorics, according to Equation 4.7. Realistically speaking, the measured Y_{bg} is not zero, as some correlations could exist between the selected "background π^0 's" and hadrons; the background π^0 's are mostly photons from other π^0 decays, even though they are not correctly paired with

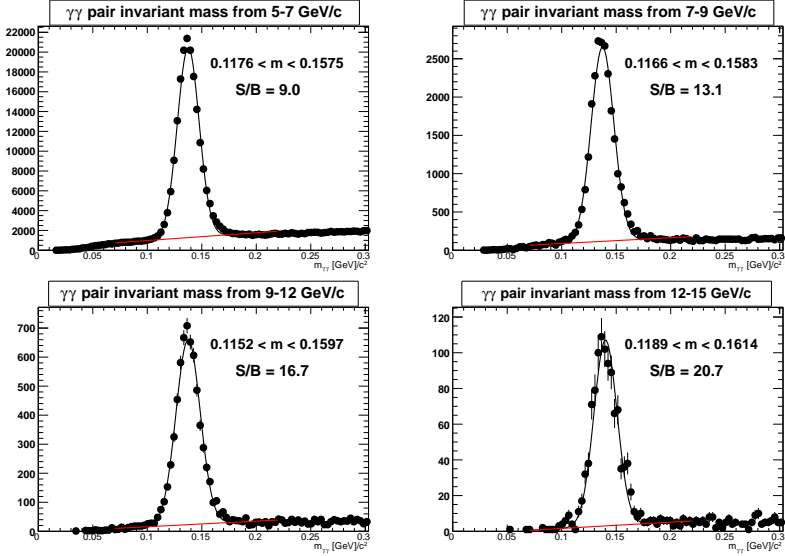


Figure 4.2: π^0 invariant mass peaks and signal-to-background ratios for 20–40% centrality class

their true decay partners.

Another method to determine Y_{bg}/Y_{meas} is by utilizing the Monte Carlo decay mapping, discussed in 3.7.2, to correct the measured decay photon p_T to the true p_T . Y_{bg}/Y_{meas} therefore is calculated via an iterative process during which the correction is applied to the measured yields. The yields are then plotted as a function of trigger p_T . Fig. 4.3 shows an example of the away-side $\pi^0 - h$ per-trigger yield as a function of $\pi^0 p_T$. As discussed in Ref. [80], the value of 2 is adopted as a conservative estimate for Y_{bg}/Y_{meas} and used for Y_{bg}/Y_{meas} to determine $\sigma_{comb}^{\pi^0}$ in all p_T bins. The same is done in this analysis. Together with the determined signal-to-background ratios in each trigger p_T bin, the π^0 combinatorial error can be obtained.

4.4 Uncertainties on Jet Function Extraction

Uncertainties on the procedure of extracting jet functions arise when removing combinatorial pairs coming from the underlying event. As discussed in chapter 3, this procedure involves the determination of the background shape and level. The former is achieved by measuring the azimuthal asymmetry

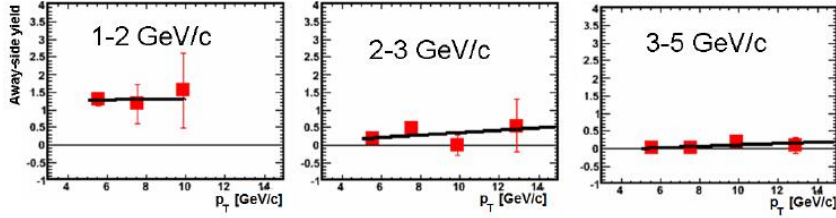


Figure 4.3: $\pi^0 - h$ per trigger yield on the away-side as a function of $\pi^0 p_T$ for hadron p_T within 1-2, 2-3 and 3-5 GeV/c. A linear fit is used in the method to determine the π^0 combinatorial background [80].

of trigger and associated partner particles quantified by the flow parameter v_2 . The latter is obtained using absolute normalization. Consequently the systematic uncertainties are a combination of the errors from the v_2 measurement and the ABS method.

The statistical and systematic errors of the measured v_2 values are listed in Table 3.1 and 3.2. The leading uncertainties in the v_2 measurement originate from the resolution of the reaction plane determination and they are largely correlated. Since the same charged hadron v_2 values are used in the subtraction step when determining jet functions for $\gamma_{inc} - h$ and $\gamma_{dec} - h$ correlations, systematic uncertainties on those are treated as correlated errors and propagated accordingly when getting the $\gamma_{dir} - h$ correlations.

The uncertainty on the ABS method includes the statistical error on the normalization and the systematic uncertainty of the multiplicity correction determination. As discussed in section 3.3.1, the multiplicity correction or ξ correction is determined by fitting N_{coll} and N_{part} with two functional forms. After applying this multiplicity correction obtained from the fit results, the systematic error is obtained by calculating the maximum spread of the determined background levels. This uncertainty from determining the background level for v_2 subtraction is treated as a correlated error and is propagated accordingly for different trigger p_T bins. This is because the associated charged hadron samples are the same for all trigger p_T momentum ranges.

4.5 Propagation of uncertainties

4.5.1 Combining Trigger p_T bins

The Run-11 data is initially analyzed in four separate trigger p_T bins: 5-7, 7-9, 9-12 and 12-15 GeV/c. We also combined them into a wider trigger p_T bin of 5-9 GeV/c. The combination is done using a weighting procedure with weights set by the statistical significance in each trigger p_T bin. We use a power law fit to the measured direct photon spectrum reported in Ref [95] and extract the number of direct photons in the relevant p_T ranges; we use these as weights. As discussed in the earlier sections, part of the systematic uncertainties are uncorrelated for R_γ and v_2 across different trigger photon p_T bins. They are treated as correlated errors and propagated during the averaging, the same way as the rest sources of systematic uncertainties. The resulting systematic error is therefore slightly larger. As the statistical uncertainties are large in this measurement, this overestimation of systematic uncertainty has no impact. In the end the final total systematic uncertainty is calculated by taking a quadratic sum of the individual sources, shown as shaded boxes in the yield plots for the trigger p_T combined bins.

4.5.2 Combine Datasets and Centralities

The previous result is binned into the 0-40% most central Au+Au bin [74]. Therefore a summation of the 0-20% and 20-40% centrality bins is performed. This is also a weighted sum taking the statistical significance in each centrality bin. A 0-40% R_γ is calculated by taking a weighted average of the R_γ values for 0-20% and 20-40% centrality bins, with weights being the number of inclusive photon triggers in each centrality bin.

The previous publication is an aggregation of Run-7 and Run-10 Au+Au result. Considering that inputs such as R_γ and v_2 are common and therefore completely correlated across different runs, we combine the statistics of each run before background subtraction and statistical subtraction, to avoid double/triple evaluation of the significance of some of the systematics. As compared to combining $\gamma_{dir} - h$ at the last stage, this way of combining statistics reduces the overall statistical uncertainty on the jet functions as well as R_γ . Similarly, a weighted sum is performed to accurately take into account the statistical precision available in each run. The only uncorrelated error is from the hadron efficiencies which vary run-to-run. The occupancy

correction is assumed to be the same. The data agree well (within statistical uncertainties) before taking systematic uncertainties into consideration. This indicates that the quoted uncertainty on hadron efficiency from Run-7 is adequate. Therefore, taking a quadratic sum of the 7.2% uncertainty on single hadron efficiency and 5% uncertainty on the occupancy correction in Run-7 analysis, we determine the overall scale uncertainty to be 8.8% [92].

Table 4.2 shows a break down of each source of systematic uncertainty on the measured $\gamma_{dir} - h$ yields for 5-9 GeV/c trigger p_T in 0-40 % Au+Au collisions. The corresponding values of all components are listed.

ξ	Yield	Stat.	Total Sys.	R_γ	Decay	ABS	v_2
0.2	3.7e-3	2.0e-3	+3.3e-3	+6.3e-4	+3.2e-3	+2.3e-4	+4.6e-5
			-3.3e-3	-8.3e-4	-3.2e-3	-2.3e-4	-3.3e-5
0.6	2.8e-2	5.5e-3	+7.0e-3	+6.1e-4	+6.5e-3	+1.9e-3	+3.4e-4
			-7.0e-3	-7.9e-4	-6.5e-3	-1.9e-3	-3.3e-4
1.0	1.4e-1	1.4e-2	+2.0e-2	+7.2e-4	+1.6e-2	+9.2e-3	+1.7e-3
			-2.0e-2	-6.7e-4	-1.6e-2	-9.2e-3	-1.7e-3
1.4	2.5e-1	2.8e-2	+5.1e-2	+5.7e-3	+3.9e-2	+3.3e-2	+5.7e-3
			-5.1e-2	-7.3e-3	-3.9e-2	-3.3e-2	-5.7e-3
1.8	5.7e-1	4.3e-2	+1.0e-1	+8.8e-3	+5.6e-2	+8.2e-2	+1.5e-2
			-1.0e-1	-7.6e-3	-5.6e-2	-8.2e-2	-1.4e-2
2.2	5.2e-1	9.1e-2	+2.0e-1	+1.1e-2	+4.1e-2	+1.9e-1	+2.9e-2
			-2.0e-1	-1.2e-2	-4.1e-2	-1.9e-1	-2.3e-2
2.6	5.9e-1	1.2e-1	+2.8e-1	+6.6e-2	+1.6e-2	+2.6e-1	+5.0e-2
			-2.8e-1	-4.3e-2	-1.6e-2	-2.6e-1	-7.8e-2

Table 4.2: Direct photon-hadron per-trigger yield in ξ bins for 0-40% central Au+Au for trigger photon p_T within 5-9 GeV/c. In addition to the total statistical and systematic uncertainties, a breakdown into individual sources that contribute to the total systematic error and the corresponding values are listed.

Chapter 5

Results and Discussion

In this chapter we present the results of measuring direct photon-hadron correlations in PHENIX. First, a description of the p+p baseline measurement will be given in section 5.1. This is essential for quantifying the medium modification in Au+Au collisions.

Next, a brief review of the previous Au+Au results achieved in PHENIX will be presented in section 5.2. The Run-4 Au+Au result shows the first measurement, in which the modification factor I_{AA} is found to be smaller than unity for the trigger bin of $5 < p_T^\gamma < 12$ GeV/c and partner bin of $3 < p_T^h < 5$ GeV/c, establishing that a suppression of the jet fragments in Au+Au is observed. An attempt to measure the away-side fragmentation function is made but no difference was discovered comparing to p+p given the large uncertainties. The Run-7 and Run-10 combined result further explored the jet fragmentation function modification in Au+Au collisions and observed a suppression in the low ξ (high z_T) region and an enhancement at higher ξ (low z_T) with respect to p+p. This result suggests that in Au+Au collisions an energy redistribution is involved so that additional lower momentum particles appear. The comparisons with theory predictions show a qualitative agreement. However qualitative study of the trigger p_T dependence of the observed I_{AA} trend and further investigation of the parton energy loss in the medium require higher statistics measurements.

In section 5.3, the Run-11 Au+Au $\gamma - h$ result is shown. By combining it with the Run-7 and Run-10 statistics, we present in section 5.4 the final result in forms of angular distributions of the per-trigger yield. Fragmentation functions are measured by integrating the away-side per-trigger yields and plotting as a function of the variable ξ . Finally I_{AA} is calculated for each

trigger bin. The improved statistics allow for studying the trigger photon p_T (the jet p_T) dependence of the modification. Comparisons to the theoretical models described in chapter 1 are shown and physics interpretation is discussed.

5.1 The p+p baseline

In order to investigate the medium effect in heavy ion collisions, a p+p baseline measurement is needed for comparison. The p+p data shown in this chapter are derived by analyzing the Run-5 and Run-6 combined data set for p+p collisions at the center-of-mass energy of 200 GeV [76].

Not discussed in the previous text, a photon isolation method can be used when measuring $\gamma_{dir} - h$ in small collision systems. The purpose of this method is to select direct photons and reject photons from jet fragmentation. This event-by-event direct photon identification minimizes the statistical and systematic uncertainties on the $\gamma_{dir} - h$ measurement.

The procedure includes the application of tagging and isolation cuts. First, photons above some p_T threshold are paired those with invariant mass in a certain π^0 invariant mass window are tagged as decay photons and removed from the sample. Next an isolation criterion is applied to the remaining photons to further reduce the decay background and improve the measurement uncertainties. This also reduces the fragmentation photon contamination - taking into account the non-leading order effects. The basic isolation requirement is that the energy in a cone around the trigger photon be less than some threshold, which is typically 10% of the photon energy in p+p collisions. In the d+Au analysis this cut is modified slightly to include the effect of the modest underlying event. Some decay photons are missed by the π^0 or π^0 tagging cut and get isolated as direct photons. The falsely isolated decay photon-hadron correlations are corrected using a statistical subtraction, illustrated in the following Eqn. 5.1, similar to what is done in Au+Au.

$$Y_{dir}^{iso} = \frac{1}{R'_\gamma - 1} \cdot (R'_\gamma Y_{inc}^{miss,iso} - Y_{dec}^{miss,iso}) \quad (5.1)$$

$$R'_\gamma = \frac{N_{inc} - N_{dec}^{tag} - N_{inc}^{niso}}{N_{dec}^{miss,iso}} \quad (5.2)$$

where $Y_{inc}^{miss,iso}$ refers to the per-trigger yield of hadrons correlated with all remaining photons after π^0 tagging and isolation cuts. R'_γ is defined as the ratio of the total number of photons surviving the tagging and isolation cuts to the number of decay photons that pass the same cuts.

In central Au+Au collisions it is quite challenging to implement the isolation technique event-by-event due to the large multiplicity. Therefore it is

difficult to apply the traditional isolation cut by requiring the energy inside a cone around a trigger photon be less than a fraction of the photon energy, since even when using a smaller cone size the total energy of the adjacent particles is usually larger than the photon energy.

On the other hand, a tagging cut study was conducted using the Run-7 Au+Au data set, assuming it is possible to remove a certain fraction of decay photons if they can be reconstructed as part of a π^0 , as reported in Ref. [80]. Since the probability is larger for a direct photon to be mistakenly tagged as a decay photon in the high multiplicity situation, a good measurement of R'_γ is required so that the falsely tagged direct photons can be corrected via the statistical subtraction. The conclusion of the study is that the uncertainty on the determined R'_γ is too large for implementing this tagging method in Au+Au collisions. The π^0 tagging cut might be effective at higher p_T , where the background is smaller, or in peripheral events, where the multiplicity is lower. Pursuing such an improvement in signal-to-background would be promising if there is a better measurement of R_γ , for example from a data set with much higher statistics. Considering that the statistics in higher p_T bins are limited and the peripheral cases are out of the scope of this work, the study is not further explored in this analysis.

The p+p baseline measurement in this dissertation results from Run-5 and Run-6 p+p collisions at the center-of-mass energy of 200 GeV. Fig. 5.1 shows azimuthal angular distributions of measured $\pi^0 - h$, direct $\gamma - h$ and isolated $\gamma - h$ in p+p [76].

From this plot, one can immediately make the following observations. For π^0 triggered correlations, there are hadron yields in both the near-side and the away-side. The presence of a near-side peak can be explained by the fact that π^0 's are fragments from a jet and so are accompanied in the same direction by other particles from the same jet. The magnitude of the $\pi^0 - h$ near-side yield is higher than that of the away-side is because of the trigger bias. Since the jets are not exactly produced back-to-back considering the parton's intrinsic k_T inside the nucleus, experimentally it is more likely to select on jets that carries larger k_T as it is more likely for it to produce a high p_T fragment. This effect manifests itself as a higher yield associated with the near-side jet.

On the other hand, the hadron yield triggered using direct photons, or isolated photons are only observed on the away-side, indicating the effectiveness of statistical subtraction of the decay background as well as the isolation cut. At leading order, high momentum direct photons are produced back-to-back

against partons in the initial hard scattering via QCD Compton scatterings, therefore negligible yield on the near side should be expected. Correlations triggered by isolated photons have no near-side associated particles by construction.

On the away-side in the same trigger p_T range, the $\pi^0 - h$ yields are larger than photon-triggered yields. This can be understood because π^0 s are fragments from a jet and consequently as triggers they sample larger jet energy than direct photons with the same p_T .

Fig. 5.2 shows the x_E distribution of the full away-side ($|\Delta\phi - \pi| < \pi/2$) integrated per-trigger yield measured using $\pi^0 - h$ and isolated direct $\gamma - h$ correlations for trigger p_T ranges of 5-7, 7-9, 9-12 and 12-15 GeV/c [76]. The variable x_E is defined as the following:

$$x_E \equiv -\frac{\vec{p}_T^{trig} \cdot \vec{p}_T^{assoc}}{|\vec{p}_T^{trig}|^2} = -\frac{|p_T^{assoc}|}{|p_T^{trig}|} \cos\Delta\phi \quad (5.3)$$

x_E is equivalent to z_T when $\cos(\Delta\phi) = 1$. Larger x_E corresponds to higher momentum fraction p_T^h/p_T^γ , i.e. higher hadron momentum bins. A change of variable into $\xi = -\ln(x_E)$ converts the distribution into Fig. 5.3 [76]. Fig. 5.2 and Fig. 5.3 are a measure of the away-side jet fragmentation function. In Fig. 5.2, the x_E distributions are fit with an exponential functional form. Both $\pi^0 - h$ and isolated $\gamma - h$ per-trigger yield exhibit x_E scaling for the fit ranges shown in the figures. The slope of the isolated direct $\gamma - h$ is determined to be 8.2 ± 0.3 , which is in good agreement with the exponential slope of 8.2 for quark fragmentation. The slope of gluon fragmentation function is 11.4. This result agrees with the expectation that the measurement of isolated $\gamma_{dir} - h$ arises from Compton scattering, so the photons trigger predominantly quark jets. π^0 s trigger on a mixture of quark and gluon jets [80].

In Fig. 5.3 the ξ distributions show an agreement with the TASSO measurement from e^+e^- collisions [96]. The distribution from TASSO is the quark fragmentation function. The TASSO data points are arbitrarily scaled down by a factor of 10, in order to account for the PHENIX acceptance and match the data [76]. The reasonable agreement confirms that the p+p measurement is a gauge of the quark jet fragmentation function.

In the later section 5.3 and 5.4, the new Au+Au $\gamma_{dir} - h$ will be presented. The jet fragmentation function measured in Au+Au collisions is compared to that in p+p. The p+p measurement discussed in this section is used as

a baseline to quantify the modification observed in Au+Au, as there is not any possible medium effects in p+p collisions.

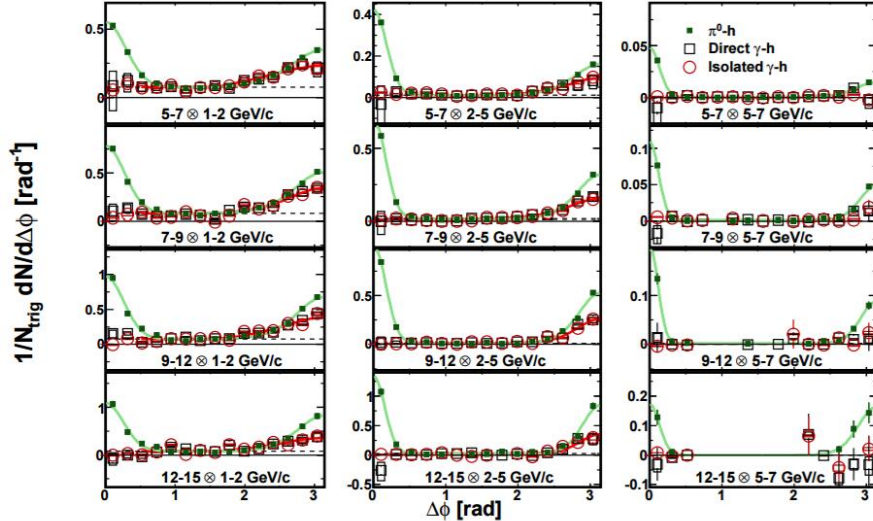


Figure 5.1: Azimuthal angular distributions of $\pi^0 - h$, direct $\gamma - h$ and isolated $\gamma - h$ in p+p collisions for different trigger and associated hadron p_T bins with momentum ranges of $5 < p_T^{trig} < 15$ GeV/c and $1 < p_T^h < 7$ GeV/c [76].

This p+p result is published in Ref. [76]. In order to directly compare with the Au+Au results here, the p+p baseline results are re-derived so that the binning matches what is chosen in the Au+Au analyses, instead of taking final analyzed results from the published PHENIX paper. The derived p+p results together with the Run-7 and Run-10 Au+Au result are published in Ref. [74]. The jet fragmentation function using this p+p analysis is regenerated and checked against the published values, before comparing to the new Au+Au data.

5.2 Previous Au+Au $\gamma_{dir} - h$ results

The first $\gamma_{dir} - h$ correlation measurement in Au+Au collisions reported from PHENIX is the Run-4 result published in [75]. In Fig. 5.4, the top and bottom panels show respectively the azimuthal angular distributions of the measured $\gamma_{dir} - h$ yields in p+p collisions and Au+Au 0-20% most central

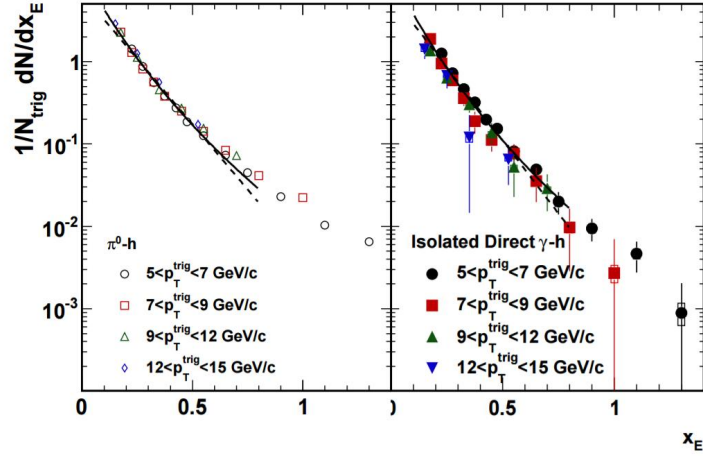


Figure 5.2: x_E distributions of the integrated full away-side yields triggered by π^0 s and isolated direct photons in transverse momentum ranges of 5-7, 7-9, 9-12 and 12-15 GeV/c. Fits to the data using an exponential functional form and a modified Hagedorn function are shown in the dashed line and the solid line, respectively [76].

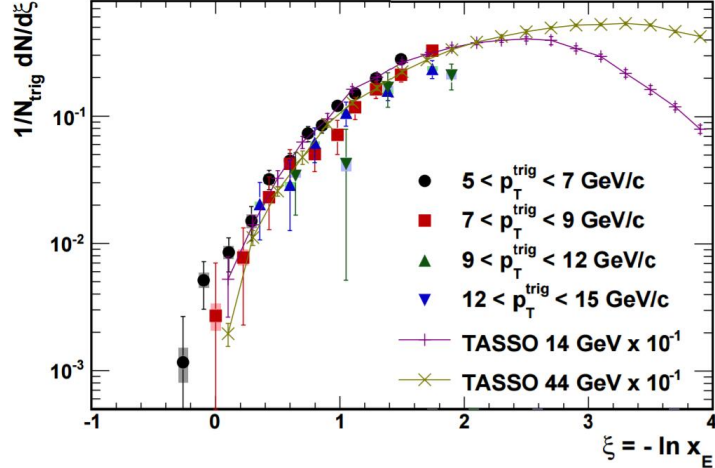


Figure 5.3: ξ distributions for the integrated full away-side yields triggered by isolated direct photons in transverse momentum ranges of 5-7, 7-9, 9-12 and 12-15 GeV/c. TASSO data in e^+e^- collisions at $\sqrt{s} = 14$ and 44 GeV are included for comparison [76].

collisions. In addition, the inclusive and decay $\gamma - h$ correlations are plotted as well. As defined before, they are all so-called jet functions which are correlation functions after all corrections and flow removal. One can see that for either the inclusive or decay $\gamma - h$ correlations, there is a near-side peaks and an away-side peak. The near-side peak exists because photons (mostly from decays) are correlated with particles that are fragments from the same jet, demonstrated in the form of more pairs in small $\Delta\phi$ range around zero. This is also true for di-hadron correlations. On the contrary, direct photons are predominantly produced from an initial hard scattering, they are not originated from a jet, the measured yield of hadrons that travel along the same direction as those are therefore negligible (ignoring NLO effect), as the data show.

On the away-side, hadrons associated with direct photons are observed in both p+p and Au+Au collisions, with a suppression observed in this particular kinematic range in Au+Au collisions, shown by this plot. This agrees with our understanding that the opposing jet suffers energy loss when traversing through the medium created in Au+Au collisions, compared to the situation in p+p collisions.

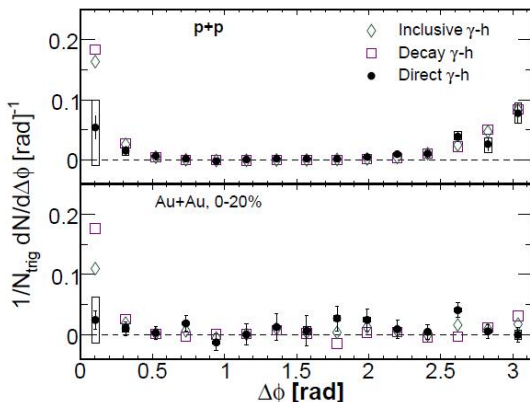


Figure 5.4: Per-trigger hadron yield with transverse momentum of $3 < p_T^h < 5$ GeV/c triggered by inclusive photons, decay photons and direct photons in $5 < p_T^\gamma < 7$ GeV/c bin in p+p (top panel) and central Au+Au collisions (bottom panel) [75].

The initial analysis tested the z_T scaling of the measured away-side yield inside the range of $|\Delta\phi - \phi| < \pi/5$ ("head region"). The reason for choos-

ing this region for integration is to maximize the statistical precision, as the signal is the largest there. This is an attempt to explore and quantify any modification of the away-side jet fragmentation function in Au+Au collisions. Taking into account the statistical and systematic uncertainties of the Au+Au measurement, the conclusion is that the data show consistency with the shape measured in p+p collisions. In the latter case the measured distributions are fitted with a simple exponential and the resulting slope agrees with quark fragmentation function [75]. The medium modification factor I_{AA} was determined with high precision only in the $3 < p_T^h < 5$ GeV/c bin for trigger p_T range of 5-12 GeV/c, with the value of $0.32 \pm 0.12^{stat} \pm 0.09^{syst}$. The level of suppression in I_{AA} in this p_T range as a function of centrality is consistent with the R_{AA} measurement [75], although the uncertainties are large, agreeing with the expectation that the geometry dependence of suppression is important.

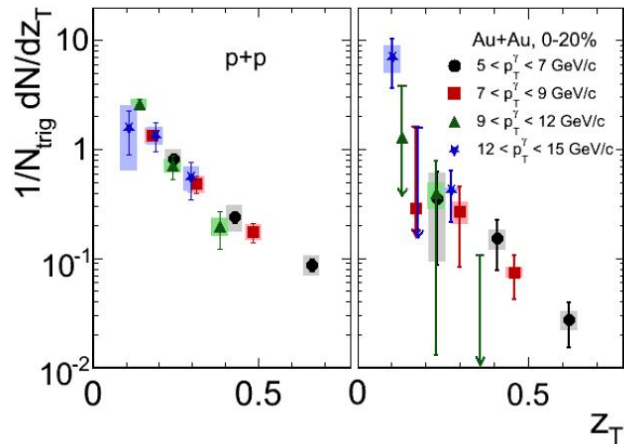


Figure 5.5: z_T distributions of $\gamma_{dir} - h$ per-trigger yield measured in p+p (left) and central Au+Au (right) collisions for trigger p_T bins of 5-7, 7-9, 9-12 and 12-15 GeV/c [75].

A more recent publication from PHENIX studied specifically the medium modification of jet fragmentation in Au+Au collisions using direct $\gamma - h$ correlation measurement. This is a product of combining the Run-7 and Run-10 results. With much improved statistics, it was possible to extend the I_{AA} measurement to a wider z_T or ξ range. In Fig. 5.6, the top panel shows the integrated full away-side ($|\Delta\phi - \pi| < \pi/2$) yield as a function of ξ and

corresponding z_T axis in 0-40% central Au+Au collisions, we compare to the p+p baseline, for trigger photon p_T of 5-9 GeV/c, correlated with hadrons with transverse momenta of $0.5 < p_T^h < 7$ GeV/c. Enhanced statistics allow for exploring the actual particle spatial positions by choosing different away-side integration ranges. By studying the particle distribution around the away-side jet axis, one probes the inner structure of the recoil jet. The bottom panel is I_{AA} - the ratio of the two distributions - defined as Y_{AA}/Y_{pp} . I_{AA} shows a suppression in Au+Au at the small ξ region and an enhancement at higher ξ . This indicates that with the presence of the medium, hadrons that carry higher momentum fraction from the parton are suppressed, while the number of soft hadrons are increased. The suppression can be understood by what we have learned so far, that jets are quenched in the medium. The origin of the observed enhancement, however, is suggested to be coming from a redistribution of the energy from the jet.

Not calculated in exactly the same kinematic ranges as the data were analyzed, the theory predictions included in the plot agree qualitatively with the data while failing to describe the actual transition point where I_{AA} exceeding unity. Both models include parton energy loss and a redistribution of the lost energy into soft particle production [74, 97, 98].

5.3 Run11 Au+Au $\gamma_{dir} - h$ results

It is not yet clear how exactly the enhancement at high ξ (low z) appears. Intuitively, it can be a result of a full redistribution of the lost energy from the propagating jet, into producing more low momentum particles. A more complicated scenario is that the jet deposits some energy in the medium and it thermalizes with the medium. The medium reacts to the jet and produces extra soft particles. The latter picture corresponds to jet-induced medium excitations, described in section 1.6.3. Experimentally, as the energy of the photon is used as a proxy for the recoil jet energy, one can study the dependence of I_{AA} enhancement on the trigger photon p_T and determine whether/how the medium affects the jet in generating more soft particles.

The physics motivation of the Run-11 Au+Au $\gamma_{dir} - h$ analysis is to add more statistics and extend the Run-7 and Run-10 result, so that it is possible to subdivide the 5-9 GeV/c trigger p_T bin presented in the previous publication [74]. I will investigate whether the observed enhanced production of soft fragments changes with photon trigger p_T , and whether the I_{AA} crossing

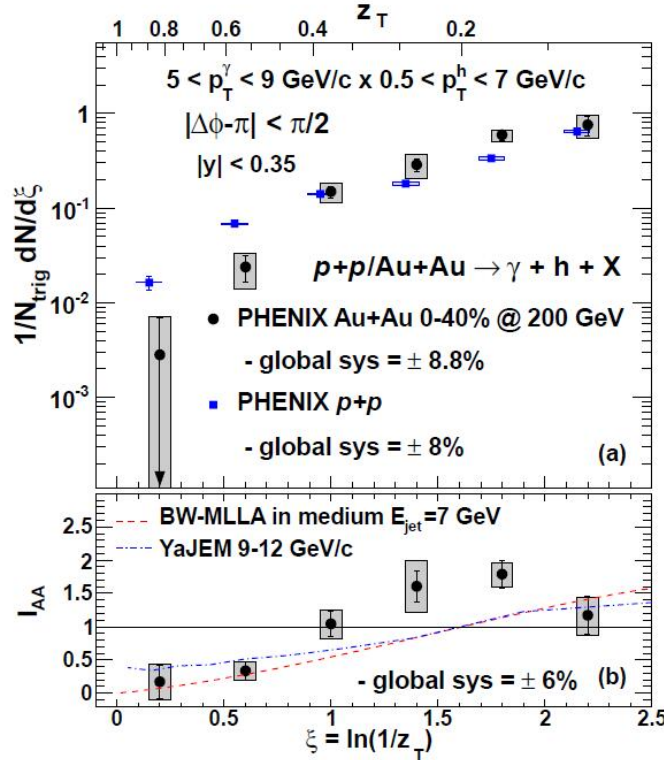


Figure 5.6: Top panel: ξ distribution of $\gamma_{dir} - h$ per-trigger yield for 0-40% most central Au+Au (black circles) collisions and p+p (blue squares) collisions. Bottom panel: I_{AA} as a function of ξ , compared to theory predictions from BW-MLLA (red dashed line) for $E_{\text{jet}} = 7 \text{ GeV}$ in medium in 0-10% most central Au+Au collisions and YaJEM (blue dot-dashed line) calculated for 0-40% centrality bin and trigger p_T of 9-12 GeV/c.

point from suppression to enhancement occurs at the same ξ value. This will improve our understanding of how jets lose energy, how the jet structure changes, and how jets and the medium interact with each other.

In 2011, PHENIX collected data from Au+Au collisions at $\sqrt{s} = 200 \text{ GeV}$. After event selection and quality cuts, the total number of minimum bias events analyzed is 4.4 billion. These are combined with the previously collected and analyzed 3.9 billion minimum bias Au+Au events from 2007 and 2.9 billion from 2010, as will be discussed in the next section.

The analysis is done using the fill-time method described in section 3.8, in

order to present correlations in ξ bins from the very beginning without having to convert data from p_T bins which would require combining overlapping points. The results presented in this section and the next section 5.4 are in ξ bins.

Fig. 5.7 shows the Run-11 Au+Au $\gamma - h$ correlations for trigger photon p_T from 5-7 GeV/c, correlated with charged hadrons of $0.5 < p_T^h < 7$ GeV/c. Azimuthal angular distributions are presented for inclusive, decay and direct $\gamma - h$ pairs. For reference the p+p $\gamma_{dir} - h$ is also plotted. Note that in PHENIX, the acceptance in rapidity is relatively small ($-0.35 < \eta < 0.35$); the measured $\Delta\eta$ distributions show little jet correlations if we project onto the y-z plane. Therefore we mainly focus on correlation measurements in the $x - y$ plane, i.e. in $\Delta\phi$.

The ξ bins are chosen to be 0-0.4, 0.4-0.8, 0.8-1.2, 1.2-1.6, 1.6-2.0, and are plotted from high to low ξ , corresponding to the conventional rising order of p_T^h binning. The $2 < \xi < 2.4$ bin is not included since it is not fully filled given the particular trigger and partner p_T ranges above.

The gray boxes displayed on the measured $\gamma_{dir} - h$ data points are the systematic uncertainties, including R_γ , decay determination and background determination. On the near side, the $\gamma_{dir} - h$ yields are consistent with zero, indicating that the statistical subtraction is done properly. The statistical uncertainties are large for $\Delta\phi \sim 1.5$ rad due to the PHENIX acceptance, i.e. the two arm configuration results in fewer pairs being measured since one particle of the pair is very likely to miss the detector. The overall statistics are poor for the highest ξ bin, due to the small signal-to-background ratio for low p_T hadrons. For inclusive and decay $\gamma - h$, the jet functions display a more peaked structure on the near-side than the away-side, with decreasing ξ . This is because hadrons with high momentum are more likely to be fragments from the jet correlated with the trigger photon. For softer hadrons, a large portion are combinatorial background, which carries a significant flow modulation. After flow subtraction, the level of the real physical correlations on the near-side are comparable to that on the away-side.

Fig. 5.9 shows the Run-11 $\Delta\phi$ distribution of $\gamma_{dir} - h$ with trigger p_T of 5-9 GeV/c, compared with p+p baseline. The uncertainties are large in the Au+Au result, however we can still observe a consistency with the Run-7 + Run-10. On the away-side, the Au+Au data show an enhancement and change over to a suppression as ξ gets smaller. The $2 < \xi < 2.4$ bin shows a slight over-subtraction of background, which can be understood from the fact that the background is large for the lowest ξ bin. This bin is dominated by

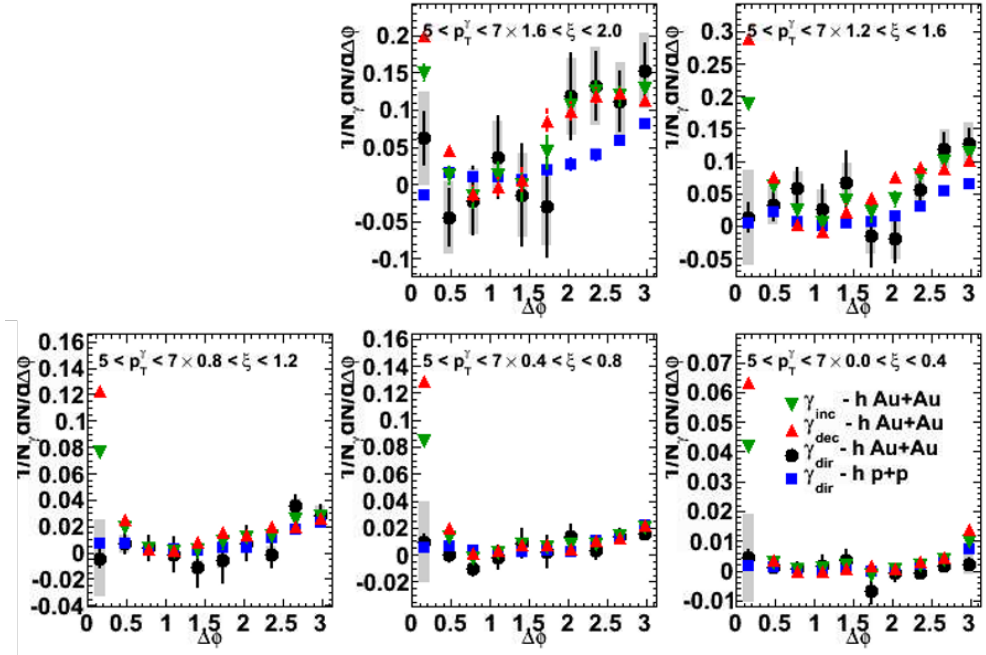


Figure 5.7: γ_{inc} -h (green), γ_{dec} -h (red) and γ_{dir} -h (black) correlations for trigger photon $5-7$ GeV/c, in Au+Au 0-40% most central collisions from Run-11. γ_{dir} -h in p+p collisions (blue) is included for comparison.

triggers from 7-9 GeV/c, since the 5-7 GeV/c trigger bin does not completely fill the kinematic range, as mentioned earlier.

When combining trigger photon p_T bins, the systematic uncertainties are estimated conservatively by treating the errors on R_γ and v_2 as correlated, despite the fact that there are also uncorrelated components across trigger bins. However given the large statistical uncertainties, the modest overestimate of the systematic uncertainties is acceptable.

In order to reduce the statistical uncertainties on the $\gamma_{dir} - h$ analysis, the Run-11 Au+Au result is combined with those from Run-7 and Run-10, as presented in the following section.

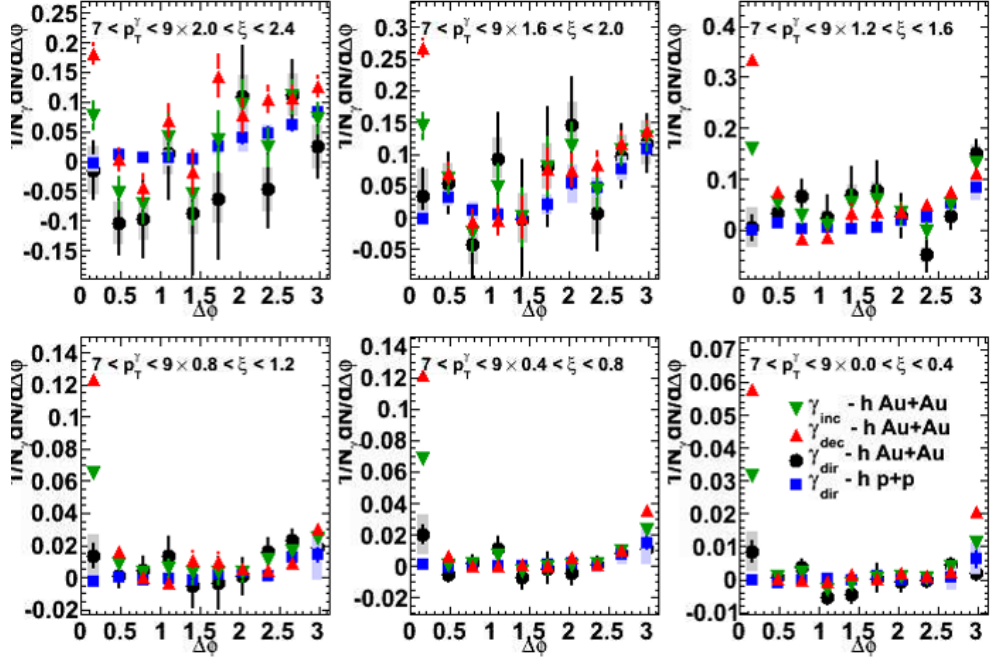


Figure 5.8: γ_{inc} -h (green), γ_{dec} -h (red) and γ_{dir} -h (black) correlations for trigger photon $7-9$ GeV/c, in Au+Au 0-40% most central collisions from Run-11. γ_{dir} -h in p+p collisions (blue) is included for comparison.

5.4 Combined Au+Au $\gamma_{dir} - h$ results

5.4.1 $\Delta\phi$ distributions

Fig. 5.10 and 5.11 present the azimuthal angular distribution of the $\gamma - h$ per-trigger yield for 0-40% most central Au+Au data combining Run-7, Run-10 and Run-11. The figures show trigger p_T ranges of 5-7 and 7-9 GeV/c respectively, and Fig. 5.12 shows the two trigger bins combined. The Au+Au data are shown in black circles, with shaded boxes representing systematic uncertainties on the measurement. Together with the $\gamma_{dir} - h$ correlations, the $\gamma_{inc} - h$ and $\gamma_{dec} - h$ components used as inputs in the statistical subtraction step are plotted in green and red triangles respectively. The p+p $\gamma_{dir} - h$ result is also shown as a comparison, in blue squares. The p+p baseline measurement is the derived result from analyzing and combining the Run-5 and Run-6 p+p data, discussed above. It is worth noting that the tagging and isolation cut in the p+p analysis makes the near-side yield not measurable.

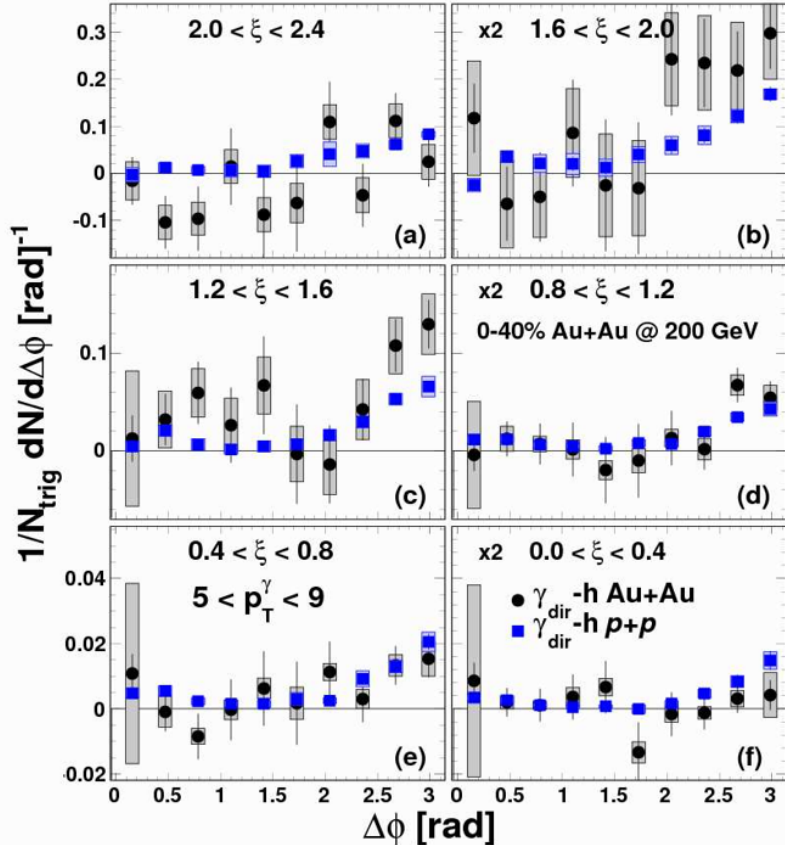


Figure 5.9: γ_{dir} -h (black) correlations for trigger photon $5-9$ GeV/c, in Au+Au 0-40% most central collisions from Run-11, compared to γ_{dir} -h in p+p collisions (blue). Panels (b), (d), and (f) are scaled up by a factor of 2.

Consequently, the p+p points with $\Delta\phi < 1$ are not shown in the distributions.

On the near side, the Au+Au direct photon triggered hadron yields are consistent with zero given the uncertainties, showing that the statistical subtraction is properly carried out and the fragmentation photon contribution is negligible. The yield around $\pi/2$ is also consistent with zero indicating that the soft background has been properly removed. On the away-side, one sees an enhancement in the Au+Au yields in the high ξ bins compared to p+p. As we go down to lower ξ bins, the Au+Au per trigger yield is suppressed. The effect can be seen more clearly in Fig. 5.13 to Fig. 5.15, which zoom in to show just the $\gamma_{dir} - h$ results.

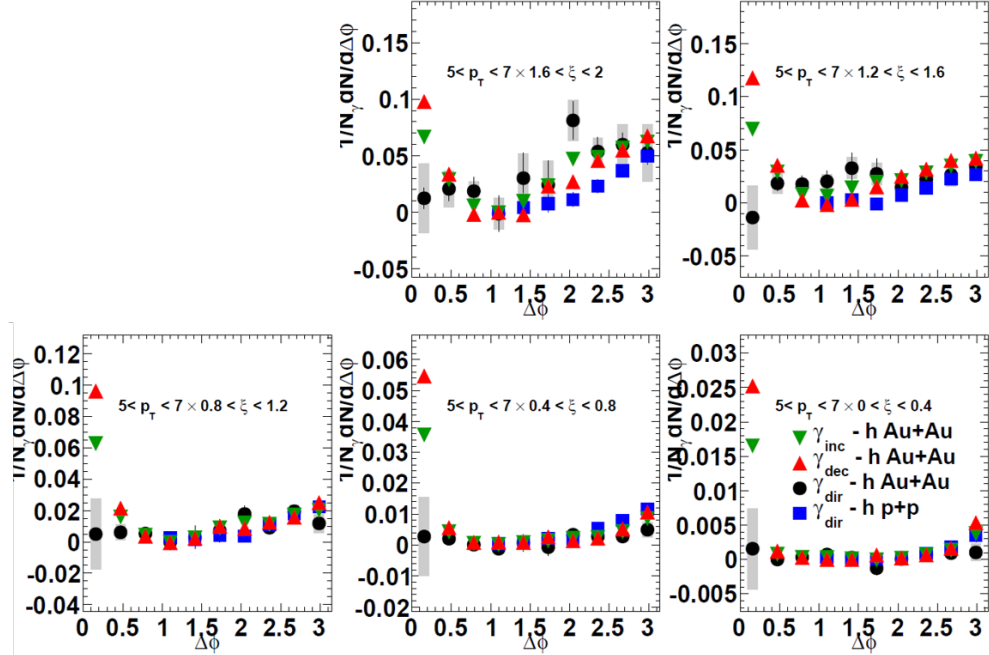


Figure 5.10: γ_{inc} -h, γ_{dec} -h and γ_{dir} -h for trigger photon 5-7 GeV/c, using combined statistics from Run-7, Run-10 and Run-11.

5.4.2 Integrated away-side yields

Parton energy loss in the medium can be observed as a modification to the jet fragmentation function in heavy ion collisions. As discussed earlier, the fragmentation function represents the probability for a parton to fragment into a hadron carrying a certain fraction of the partons energy.

We use the momentum of the trigger photon as a proxy of the away-side jet momentum and the fragmentation function is expressed in terms of z_T . To focus more on the low z_T region where the enhancement in Au+Au with respect to p+p is, one can express the fragmentation function in terms of variable ξ .

To obtain the fragmentation function, we integrate the away-side yield of the distribution and plot as a function of ξ , as illustrated in Fig. 5.16. The integrated away-side yields in Au+Au collisions are shown as black circles, and the p+p baseline in blue open squares. Note that the data points are plotted on the ξ axis at the middle of each ξ bin: 0.2, 0.6, 1.0, 1.4, 1.8, 2.2. The p+p points have been shifted to the left in ξ for viewing clarity.

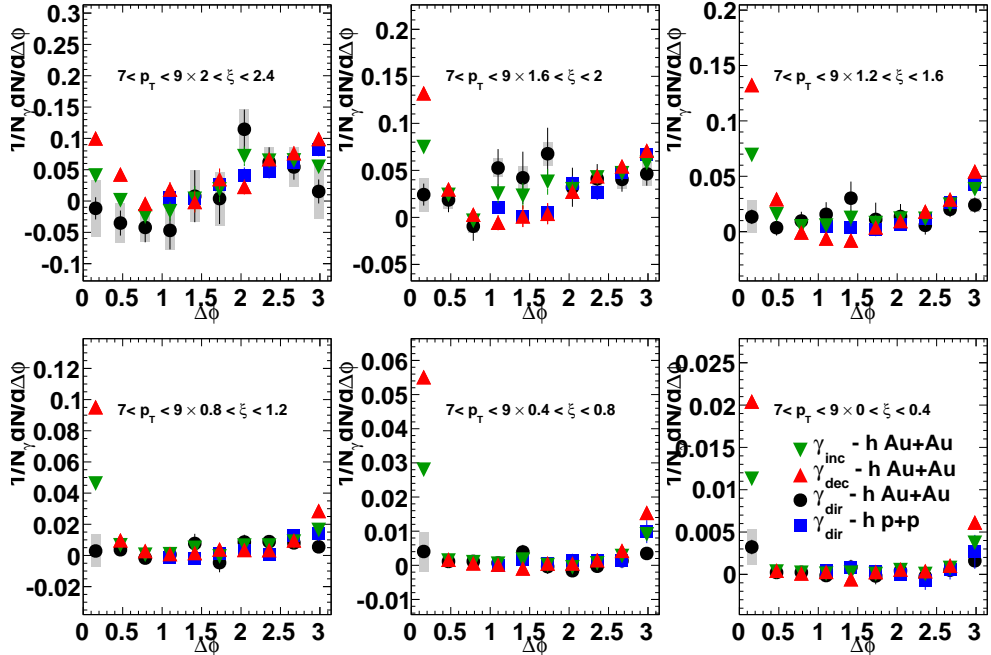


Figure 5.11: $\gamma_{inc}\text{-}h$, $\gamma_{dec}\text{-}h$ and $\gamma_{dir}\text{-}h$ for trigger photon 7-9 GeV/c, using combined statistics from Run-7, Run-10 and Run-11.

Fig. 5.17 shows ξ distributions for trigger photon momentum ranges of $5 < p_T^\gamma < 7$ GeV/c, $7 < p_T^\gamma < 9$ GeV/c and $9 < p_T^\gamma < 12$ GeV/c, with p+p data included for comparison. For trigger photon p_T of 5-9 GeV/c, the integrated away-side yield in Au+Au collisions is smaller than the p+p yield at lower ξ and starts to show enhancement as ξ increases. In the 9-12 GeV/c trigger photon p_T bin, the away-side yield in Au+Au is consistent with what is measured in p+p, given the current uncertainties, although a suppression is expected for the higher trigger p_T bin in Au+Au collisions.

A more direct way to evaluate the difference between the ξ distributions in Au+Au and p+p, is the ratio of the two.

5.4.3 Away-side I_{AA}

We define a variable called I_{AA} ($I_{AA} = Y_{AA}/Y_{pp}$) as a nuclear modification factor quantifying the difference between the measured fragmentation function in Au+Au and p+p. Fig. 5.18 shows I_{AA} for photon triggers of

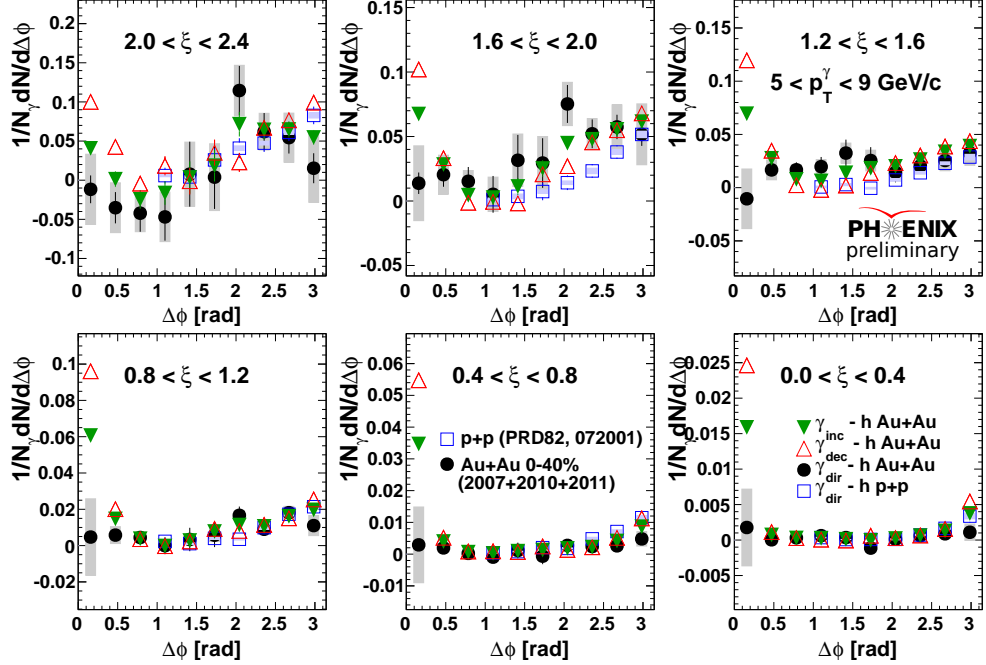


Figure 5.12: γ_{inc} -h, γ_{dec} -h and γ_{dir} -h for combined trigger photon p_T 5-9 GeV/c, using combined statistics from Run-7, Run-10 and Run-11.

$5 < p_T^\gamma < 9$ GeV/c. In the absence of medium modification, I_{AA} would equal to 1. The data instead shows a suppression at low ξ and an enhancement at higher ξ .

To better understand jet-medium interactions that can contribute to the modification observed in Au+Au collisions, finer trigger momentum ranges are needed. As discussed earlier, this would allow us to study the jet fragmentation function modification dependence on the trigger p_T . Dividing trigger p_T into finer bins would show how the enhancement for soft hadrons varies with different propagating jet energies.

Combining the statistics from the analyzed Run-11 Au+Au data with the previous Run-7 and Run-10 results allows for a differential measurement, as a function of trigger photons p_T (the jet energy). Fig. 5.19 shows I_{AA} as a function of ξ for trigger photons in three p_T bins. While the associated hadron yields are smaller than those in p+p at low ξ , the appearance of extra particles at higher ξ is observed primarily for triggers with p_T of 5-7 GeV/c. A qualitatively similar rising behavior of I_{AA} is also visible for the

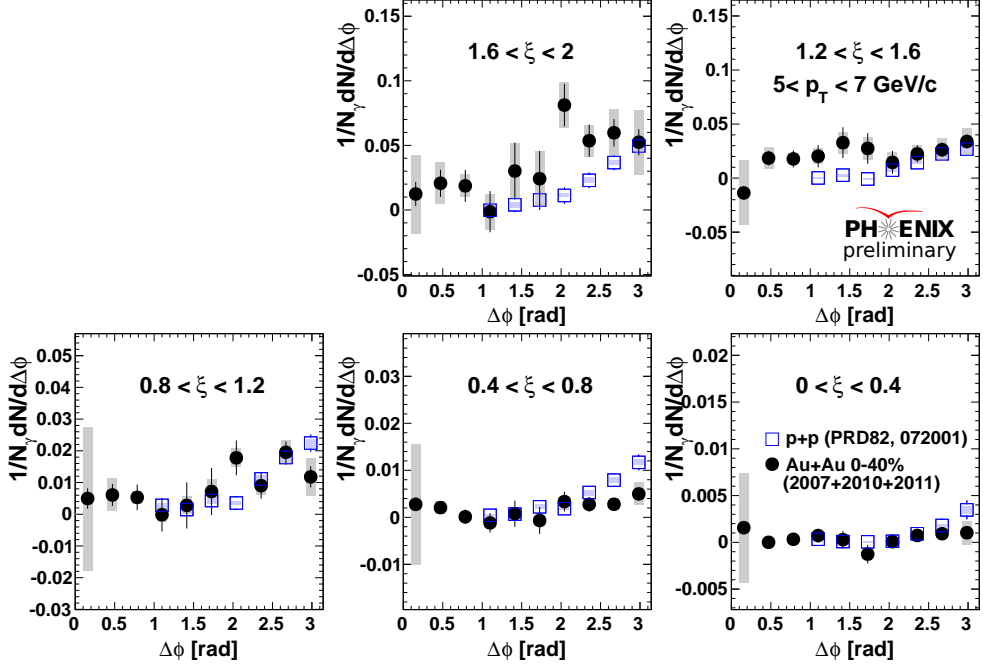


Figure 5.13: γ_{inc} -h, γ_{dec} -h and γ_{dir} -h for combined trigger photon p_T 5-7 GeV/c, using combined statistics from Run-7, Run-10 and Run-11.

7-9 GeV/c p_T bin. The improvement in statistics are sufficient to separate the 5-9 GeV/c trigger photon p_T .

Before discussing the physics interpretation of the resulting I_{AA} , I first introduce a recent development on the LBT model. Now instead using a static QGP medium, the jet propagation calculated with the LBT framework is coupled with a (3+1)D hydrodynamic model for medium evolution simulation. This coupled approach is referred to as the CoLBT-hydro model. It is a kinetic description of parton propagation combined with a hydrodynamic description of the medium evolution, by including a source term in the hydrodynamic equation. It keeps track of leading partons as well as the thermal recoil partons and their further propagation. The jet-induced medium excitation discussed in section 1.6.3 is also described by the hydrodynamics.

The jet transport and the medium evolution are simulated in concert. The jet shower partons are propagated according to the LBT embedded in a medium with a certain local temperature and evolution velocity, at a particular time τ . The "negative" partons - initial parton interacted with

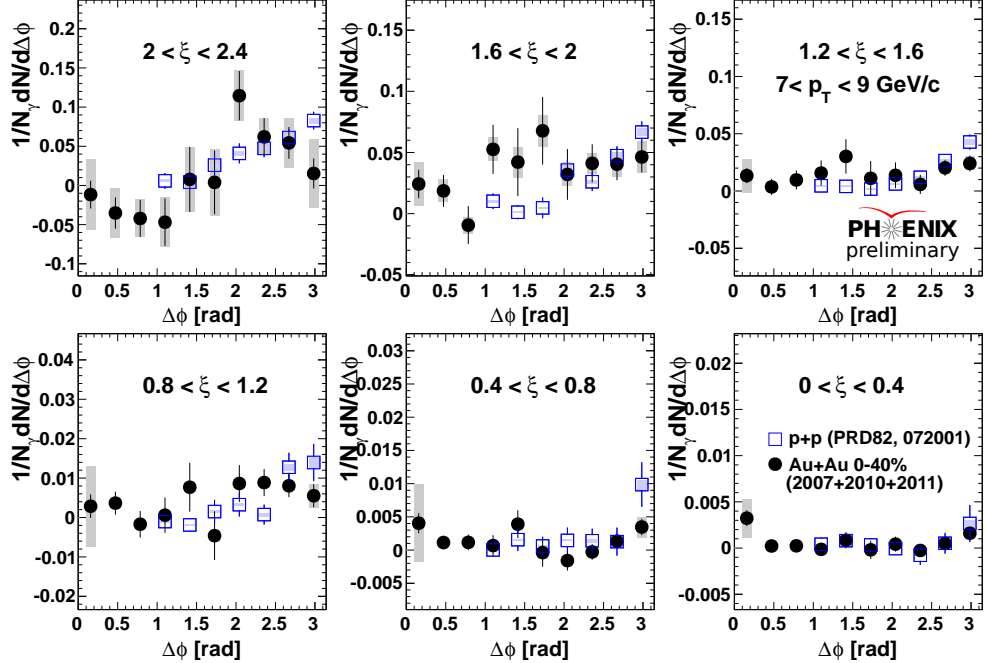


Figure 5.14: γ_{inc} -h, γ_{dec} -h and γ_{dir} -h for combined trigger photon p_T 7-9 GeV/c, using combined statistics from Run-7, Run-10 and Run-11.

the jet shower parton - are taken into account and therefore removed from the partons in LBT after each scattering, they are also not allowed to be considered as a part of the hydrodynamic evolution of the medium [22]. A Multi-Phase Transport (AMPT) model is adopted for generating the initial energy-momentum density distributions. Hadronization of the hard partons from LBT part is done using the parton recombination model from the JET Collaboration. The final associated hadron yields come from the parton recombination and Cooper-Frye freeze-out. The former is contribution from LBT and the latter corresponds to the hydrodynamical part.

The CoLBT-hydro calculation results in Fig. 5.20, which shows the energy density in the transverse x-y plane for time $\tau = 2$ and 4.8 fm/c for 0-12% most central Au+Au collisions at $\sqrt{s_{NN}} = 200$ GeV. The directions of the direct photon and the jet shower partons are shown as back-to-back. The left panels are the energy density of the γ -jet inside the medium. When subtracting out the bulk medium evolution, only the γ -jet and the jet-induced medium excitation are left. It is shown in the right panels in which a deple-

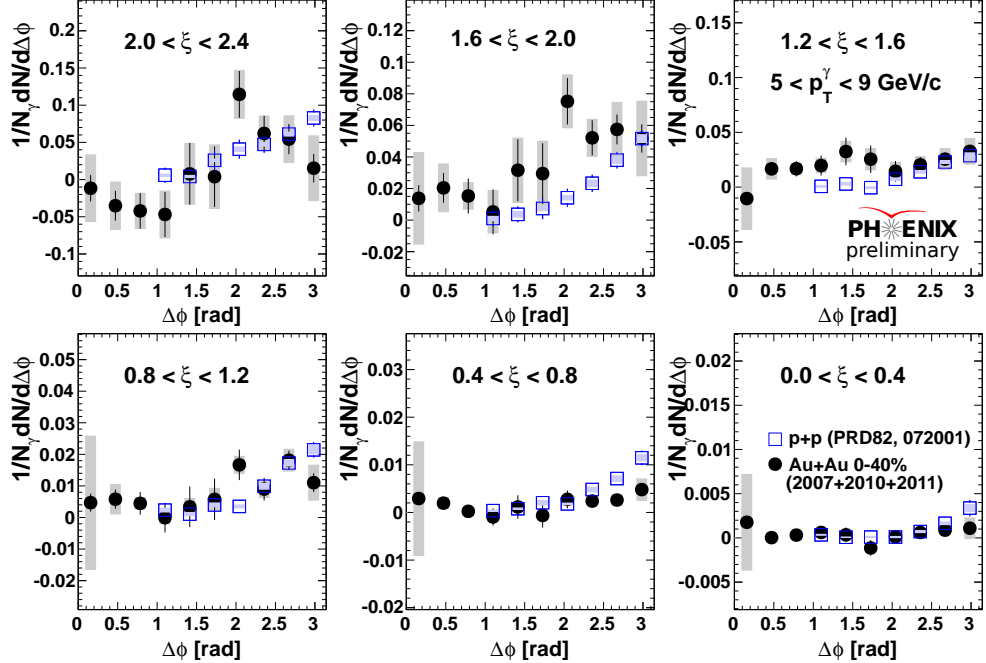


Figure 5.15: γ_{inc} -h, γ_{dec} -h and γ_{dir} -h for combined trigger photon p_T 5-9 GeV/c, using combined statistics from Run-7, Run-10 and Run-11.

tion in the energy density along the traveling photon direction. This observation coincides with the depletion in energy density Mach-cone-like response caused by the propagating jet discussed in section 1.6.3. Ref. [22] reports a first study of $\gamma_{dir} - h$ correlations using CoLBT-hydro framework. The initial jet shower partons are generated from PYTHIA8 for γ -jet events. The position of the γ -jet spacial distribution of binary hard processes from the previously mentioned AMPT event. The fragmentation function is obtained by per-trigger hadron yield as the following:

$$D(z) = \frac{dN_h}{dz} \Big|_{LBT} + \frac{dN_h}{dz} \Big|_{hydro}^{w/jet} - \frac{dN_h}{dz} \Big|_{hydro}^{no/jet} \quad (5.4)$$

where z is the momentum fraction a hadron carries from the jet: p_T^h/p_T^γ . The last term in the equation is the background from the hydro part with the same initial condition as the second term, without a $\gamma - jet$ event.

Fig. 5.21 shows a comparison of CoLBT-hydro calculations and the STAR $\gamma_{dir}-h$ results in p+p and 0-12% central Au+Au results. The calculation that

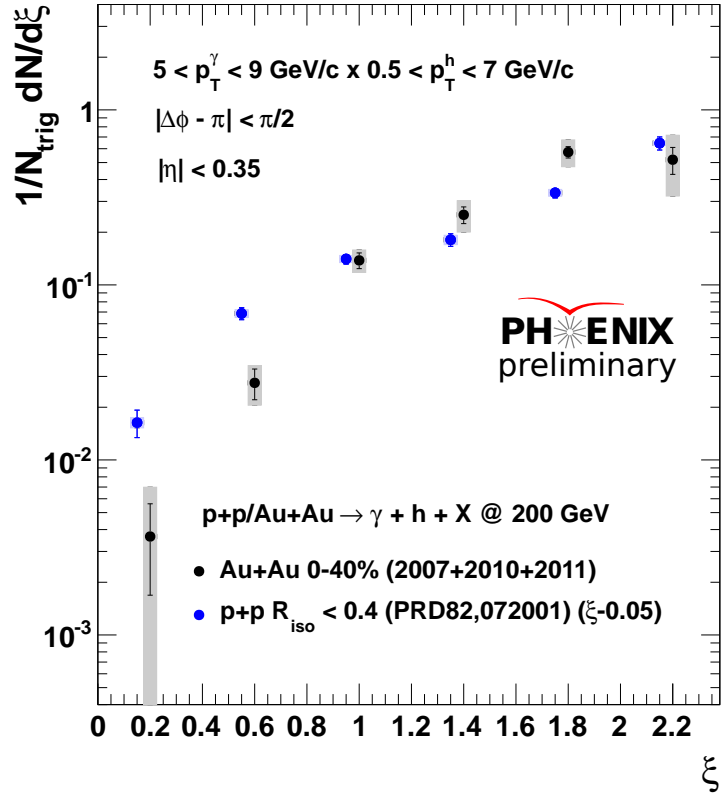


Figure 5.16: Integrated away-side ($|\Delta\phi - \pi| < \pi/2$) $\gamma_{dir} - h$ per-trigger yields as a function of ξ for trigger photons of $5 < p_T^\gamma < 9$ GeV/c (black), as compared to p+p (blue). The shaded box on each Au+Au point is the systematic uncertainty of the measurement.

includes the jet-induced medium response describes the data well, while not including this contribution results in a yield drop in the low z region. Since the STAR result is limited in the measured kinematic range, no enhancement is observed, although the model predicts such behavior down to very low z if including the medium response.

We compare our PHENIX Au+Au results to the CoLBT-hydro model shown in Fig. 5.22. Fig 5.22 shows I_{AA} as a function of ξ for the 3 trigger p_T bins; the z_T axis is exhibited on the top. The solid lines are from the CoLBT-hydro model [22] calculated specifically for the same kinematic ranges as the

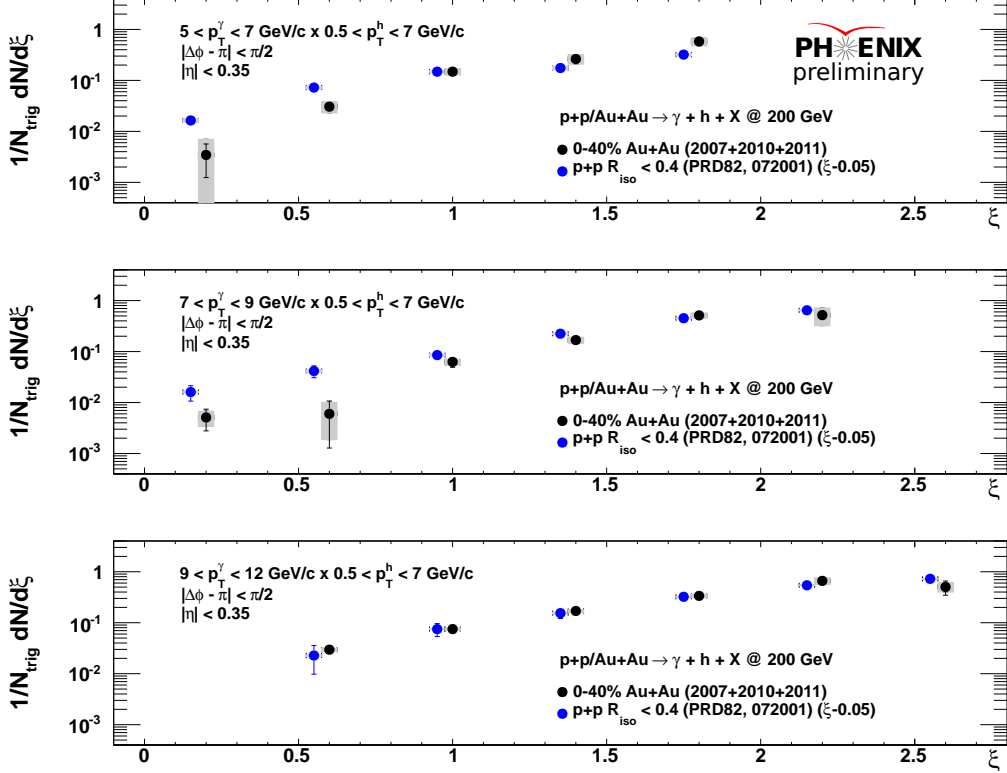


Figure 5.17: Integrated away-side ($|\Delta\phi - \pi| < \pi/2$) $\gamma_{dir} - h$ per-trigger yields vs ξ for trigger photon with p_T of 5-7 GeV/c (top panel), 7-9 GeV/c (middle panel) and 9-12 GeV/c (bottom panel). The p+p results are shown in blue circles and are shifted to the left with respect to the Au+Au data points (black) along the ξ axis for clear viewing.

data. The agreement with data is reasonably good. The model clearly shows that as the trigger photon p_T increases, the transition starts at a larger value. According to this calculation, the enhancement at large ξ is from jet-induced medium excitations, reflecting the thermal nature of the produced soft particles. Therefore a characteristic trigger p_T dependence is expected.

Also included in Fig. 5.22 is a BW-MLLA calculation in the dashed line from the same calculation shown in Fig. 5.6 but for the 7-9 GeV/c trigger p_T panel, in which the assumption is that the lost energy is redistributed and results in an enhanced production of soft particles [98]. This curve is

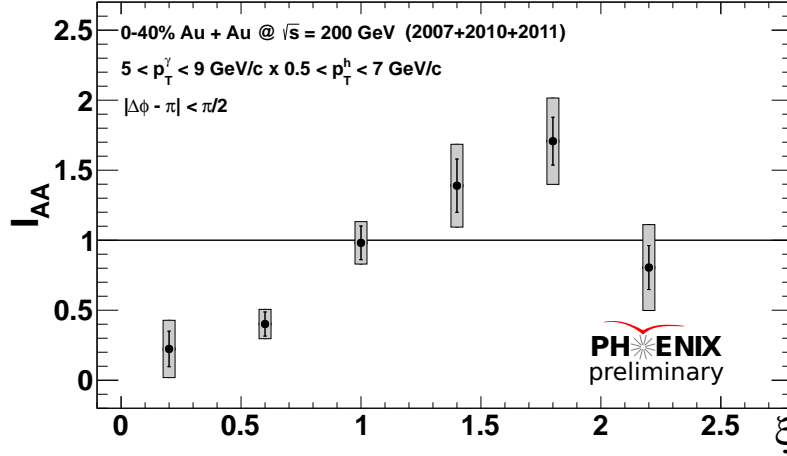


Figure 5.18: I_{AA} as a function of ξ for trigger p_T^γ of 5-9 GeV/c.

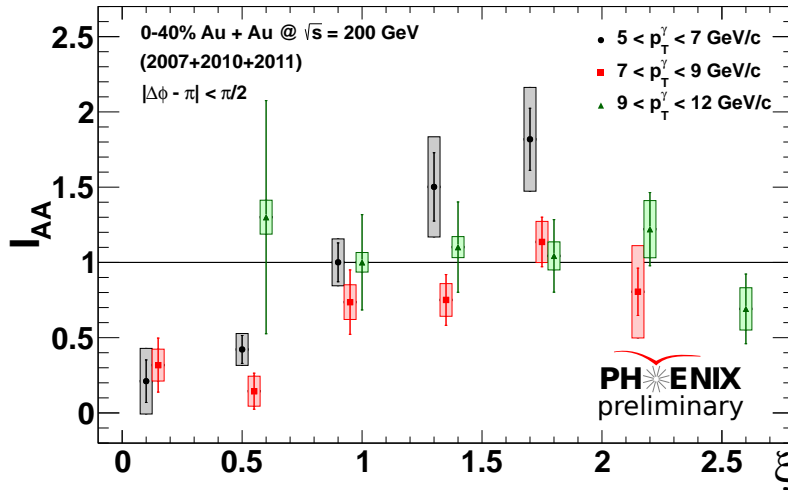


Figure 5.19: I_{AA} vs ξ for trigger p_T^γ of 5-7 GeV/c (black), 7-9 GeV/c (red) and 9-12 GeV/c (Green).

calculated for jets with energy of 7 GeV and it is in relatively good agreement with the measured results.

As a further study to investigate where the energy goes, one can look how how I_{AA} depends on the particle azimuthal angle . Two narrower away-side

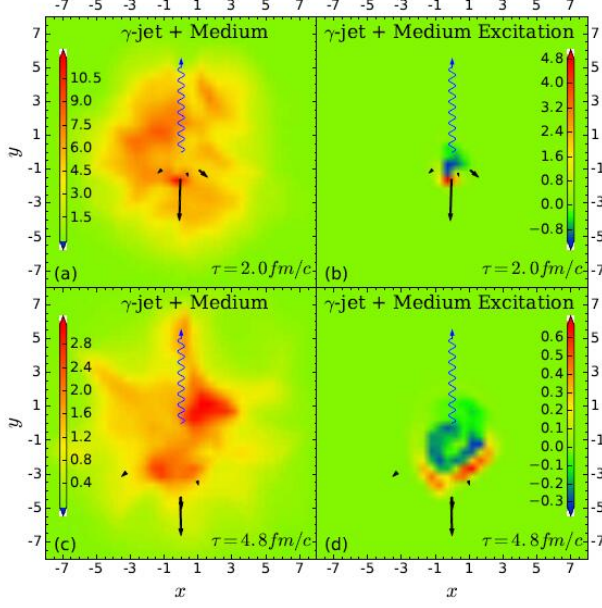


Figure 5.20: Energy density distributions demonstrating a $\gamma - jet$ event in the medium. The directions are labeled for both the trigger photon and the propagating jet in the transverse plane at $\tau = 2$ fm/c (top) and 4.8 fm/c (bottom). The two panels on the right show the scenario when not including hydrodynamic background

integration ranges - $|\Delta\phi - \pi| < \pi/3$ rad and $|\Delta\phi - \pi| < \pi/6$ rad - are selected and the integrated yields are calculated. The resulting I_{AA} are shown in Fig. 5.23. The enhancement compared to p+p is largest for 5-7 GeV/c triggers, and for the full $\pi/2$ rad integration range. This can be potentially explained by the fact that lower momentum partons go through more multiple scatterings as they traverse the medium, therefore losing a larger fraction of their energy to the medium. The enhancement comes from the jet-induced medium response. More directly one can actually see where the particles went by looking at the angular distributions for example the $1.6 < \xi < 2.0$ bin in Fig. 5.15: the particle yields are indeed enhanced at larger angle with respect to the away-side jet axis. This also coincides with the finding from CoLBT-hydro study when including medium response [22].

Regardless of whether I_{AA} is significantly larger than unity - what we have

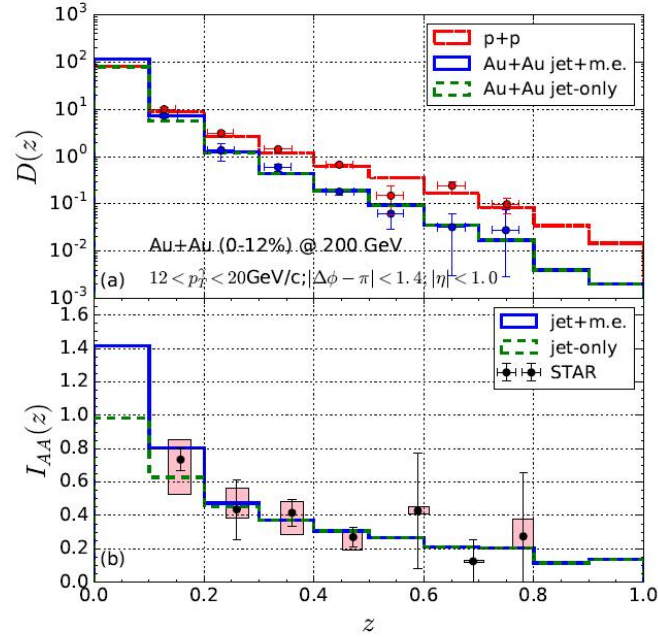


Figure 5.21: Top: the jet fragmentation function in $p+p$ and 0-12% central $Au+Au$ collisions. Bottom: I_{AA} as a function of z for CoLBT-hydro calculations with and without including jet-induced medium excitations, compared to STAR $\gamma_{dir} - h$ measurement.

been referring to as enhancement (comparing to $p+p$) - there is a tendency that I_{AA} increase as ξ increases. To quantify this "relative enhancement" at high ξ , we calculate the weighted averages of I_{AA} values above and below $\xi = 1.2$ and plot the ratio for each integration range, as a function of the trigger photon p_T in Fig. 5.24. The enhancement is largest for softer jets and for the full away-side integration range, implying that jets with lower energy get more broadened than higher energy jets.

5.4.4 A Note on the d+Au Result

Although not part of this dissertation, it is worth mentioning that a direct photon-hadron correlation analysis on 3 billions of d+Au events was carried out, using the same analysis framework as the Run-11 Au+Au analysis. The d+Au measurement is a great tool to probe potential cold nuclear matter

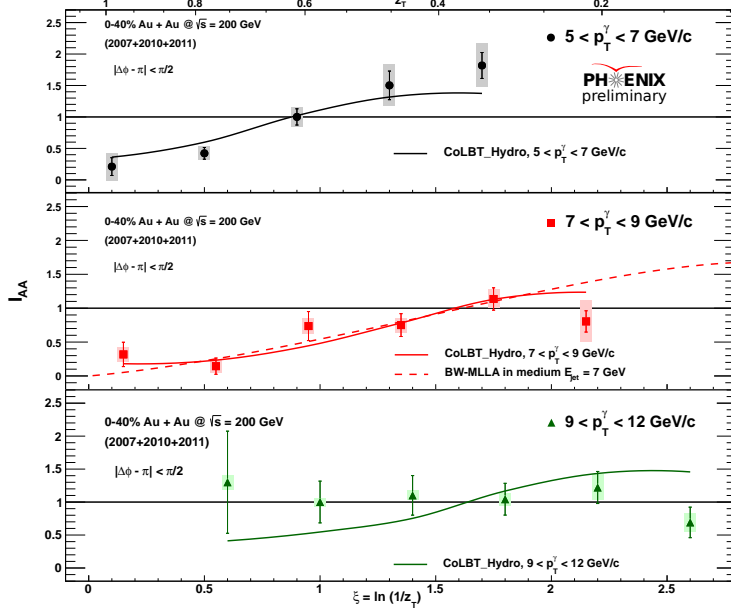


Figure 5.22: I_{AA} for trigger photon p_T of 5-7, 7-9 and 9-12 GeV/c , as a function of ξ , compared with theoretical model calculations.

effect and it serves as a test for the initial state energy loss hypothesis. The tagging and isolation method is implemented additionally to cut down on the decay contamination in the direct photon sample.

The procedure is similar to that used in the p+p analysis, which has been described in section 5.1, with some additional care taken for the larger underlying event in more central d+Au [100]. To account for the underlying event, the zero-yield-at-minimum assumption is made for each centrality class. To determine the "minimum" point when an isolation cut has been applied, which distorts the near-side yield, the minimum point is determined within the restricted range of 0.9-1.6 rad, and the zero-point yield is determined integrating in a 0.03 rad range around that minimum point. The uncertainty on the ZYAM procedure is evaluated by selecting a different range: 1.1-1.4 rad (for some p_T bins this range is varied slightly).

The ZYAM subtracted inclusive and decay yields for each centrality are combined using a weighted sum based on the number of triggers for each centrality range, to obtain the Minimum Bias (MB) yields. The final direct photon-hadron yields are determined according to Eqn. 5.1 and 5.2.

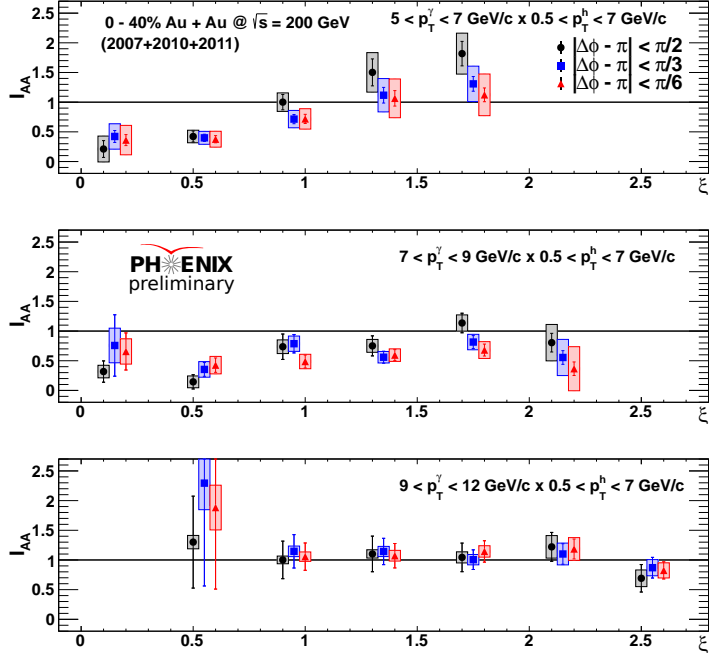


Figure 5.23: I_{AA} as a function of ξ for trigger p_T^γ of 5-7 GeV/c (top panel), 7-9 GeV/c (middle panel) and 9-12 GeV/c (bottom panel). Three away-side integration ranges are chosen to calculate the per-trigger yield and the corresponding I_{AA} : $|\Delta\phi - \pi| < \pi/2$ (black circles), $|\Delta\phi - \pi| < \pi/3$ (blue squares) and $|\Delta\phi - \pi| < \pi/6$ (red triangles). In each panel a flat line of I_{AA} is shown to guide the eye. The enhancement with respect to the p+p baseline measurement is most dominant in 5-7 GeV/c trigger bin and for the case of full away-side integration range.

Fig. 5.25 includes the d+Au $\gamma_{dir} - h$ result in purple crosses for the upper yield ξ distribution and the corresponding ratio I_{dA} defined as Y_{dA}/Y_{pp} in the bottom panel. I_{dA} is consistent with unity across all ξ ranges, indicating no significant modification on the jet fragmentation function in d+Au collisions.

Fig. 5.26 is the integrated away-side yield as a function of ξ for triggers with p_T^γ within 5 - 7, 7 - 9 and 9 - 12 GeV/c. The black and blue data points are d+Au and p+p respectively. I_{dA} is calculated for each trigger p_T bin and plotted below the yield ξ distribution. A flat line of $I_{dA} = 1$ is shown for comparison. The results of a χ^2 test under the assumption of no modification for each trigger p_T bin are listed in the plots. I_{dA} is consistent

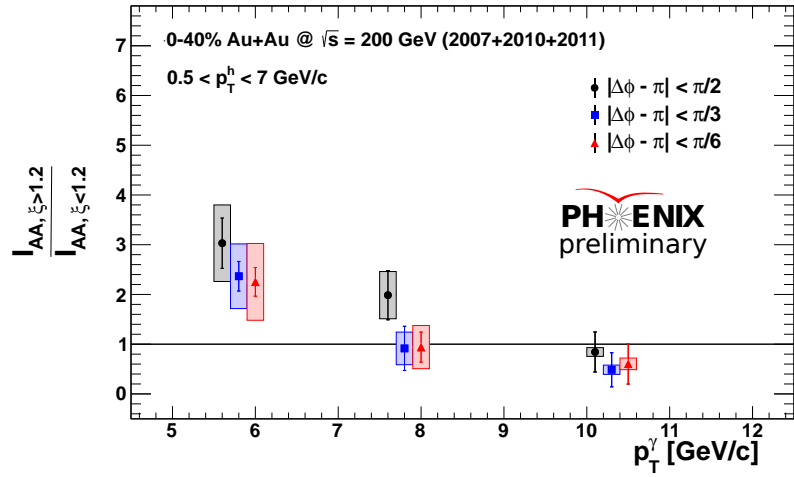


Figure 5.24: Ratios of I_{AA} as a function of trigger p_T^γ , for three different away-side integration ranges.

with unity and therefore the jet fragmentation function is not significantly modified in d+Au collisions, given the current uncertainties. This suggests that any possible cold nuclear matter effect is small.

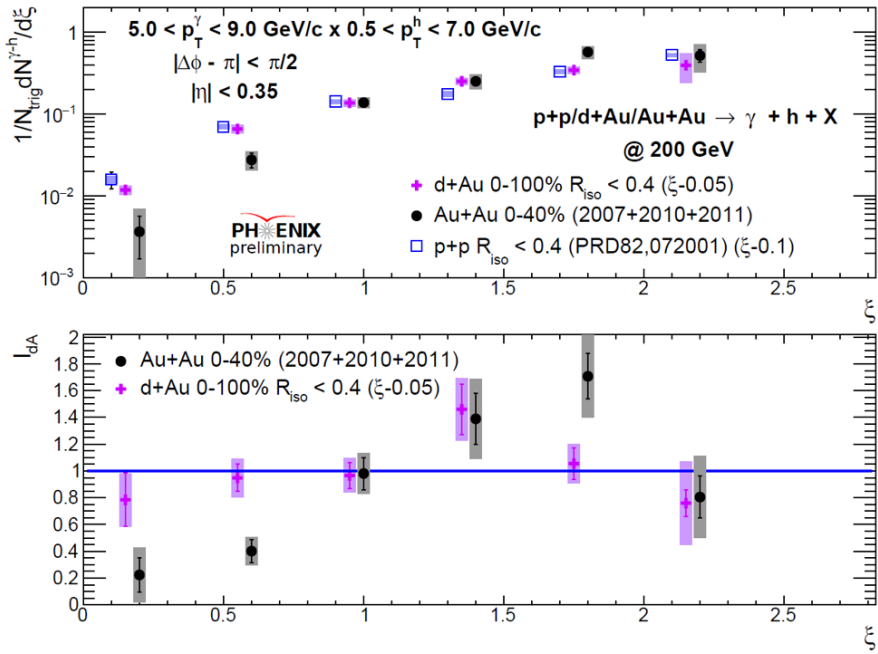


Figure 5.25: Top panel: Integrated away-side $\gamma_{dir} - h$ per-trigger yields of Au+Au (black dots), d+Au (purple crosses) and p+p (blue squares), as a function of ξ . p+p and d+Au points have been shifted to the left for clear viewing, as indicated in the legend. Bottom panel: I_{AA} (black dots) and I_{dA} (purple crosses).

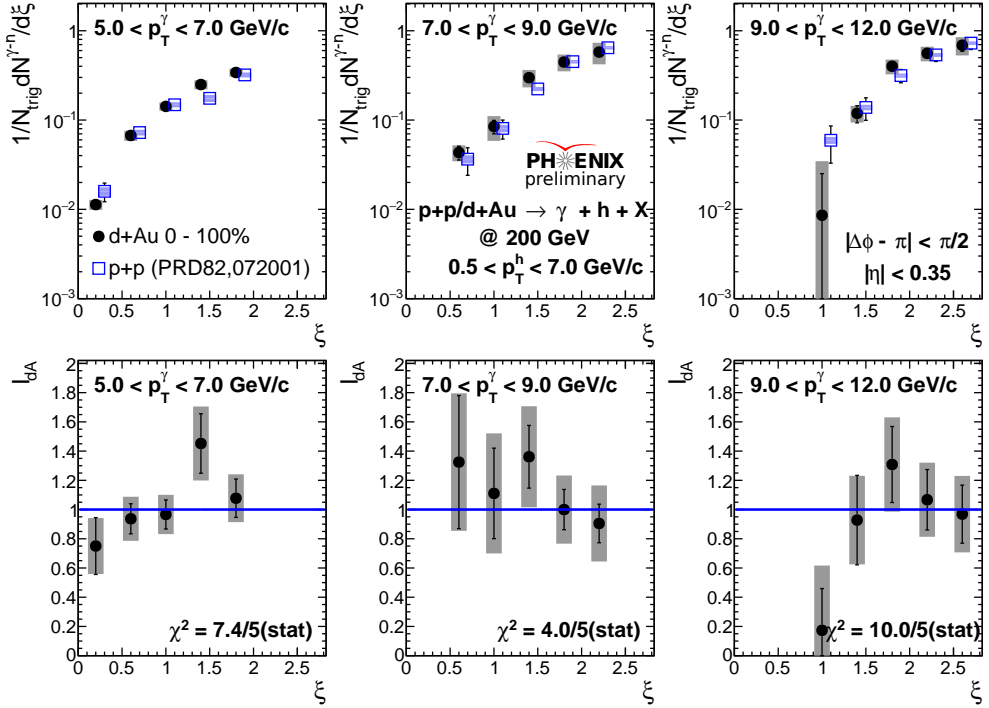


Figure 5.26: Integrated away-side ($\Delta\phi > \pi/2$) $\gamma_{\text{dir}} - h$ per-trigger yields for triggers with p_T from 5 - 7 GeV/c (top left), 7 - 9 GeV/c (top middle), and 9 - 12 GeV/c (top right). In black are the yields for the d+Au analysis, in blue are the p+p reference. The full ZYAM + R_γ + method systematic uncertainties are shown as the shaded bands around each point. The I_{dA} resulting from the ratio of the d+Au yields to the p+p yields is shown in the bottom set of Figures for each trigger p_T range.

Chapter 6

Conclusions and Outlook

6.1 Summary of the Au+Au Result

Direct photon-hadron correlations in Au+Au collisions at $\sqrt{s_{NN}} = 200\text{GeV}$ has been measured using the data collected in 2011 by the PHENIX experiment. By combining the statistics with the previous results from 2007 and 2010, we are able to study the modification on the jet fragmentation function as a function of the jet energy. This is achieved by calculating the ratio I_{AA} defined as the per-trigger yield in Au+Au to p+p, as a function of the momentum fraction the hadron carries from the trigger photon. In this analysis, the momentum fraction is expressed in an alternative variable $\xi = \ln(1/z_T)$, for the purpose of zooming on the lower momentum fraction region, as an enhancement has been observed in that region. On the other end of the ξ axis shows a suppression of I_{AA} .

One question that arises is that whether this trend of suppression to enhancement has any trigger p_T dependence and where the transition point of I_{AA} crossing unity is. We can consider two pictures: in one picture, the lost energy being fully redistributed into enhancing the production of lower momentum particles. In another picture: some of the lost energy from the jets is deposited into the medium and thermalized with the medium. In this scenario the enhancement comes mainly from jet-induced medium excitations. This all comes down to the experimental observation of whether I_{AA} crossing unity is at a fixed ξ or a fixed associated particle p_T . In that sense, a look at the I_{AA} as a function of p_T^{assoc} would be ideal.

$\gamma_{dir} - h$ calculations from the CoLBT-hydro model computed in the same

kinematic ranges as the data serve as a direct comparison. As Fig. 5.22 shows, the agreement is relatively good, that the I_{AA} shape is described and the curves suggest the transition occurs at different ξ values for different trigger photon p_T . As the jet energy increases, the crossover happens at larger ξ value. This corresponds to the picture in which the interactions between the hard partons and the thermal medium produce soft particles at larger angle with respect to the jet axis. The comparison model calculations to RHIC experiments confirms that the contribution from jet-induced medium response is significant and accounts for the jet fragmentation function modification observed in Au+Au collisions.

However due to historical reasons in PHENIX analyses, there is not yet a p+p reference available analyzed in associated hadron p_T bins, that is ready to be used for quantifying the FF modification. Efforts are being made in generating those results using the Run-5 and Run-6 p+p data using a ZYAM procedure. There is also an ongoing analysis on the Run-15 p+p $\gamma - h$ correlations, which could potentially serve as an alternative new p+p reference with better statistical precision.

6.2 Relation to Other Experimental Results

As mentioned in section 5.4, the STAR collaboration has also measured $\gamma_{dir} - h$ correlations in Au+Au collisions at $\sqrt{s_{NN}} = 200$ GeV. The trigger and partner particle selection requirements are different from the PHENIX analyses. Trigger photons are selected with transverse momentum of $12 < p_T^{trig} < 20$ GeV/c and correlated with hadrons of $p_T^{assoc} > 1.2$ GeV/c. By requiring high enough p_T of the trigger photons, STAR is able to measure fragmentation function down to low z. The basic idea for the measurement is the same as PHENIX, namely to remove the decay component from the inclusive $\gamma - h$ correlations. The excellent granularity of EMCAL in PHENIX enables good measurement of photons and π^0 s. STAR, on the other hand, uses " π^0 -rich" samples. The overall statistical uncertainties are smaller in STAR because the acceptance along η and ϕ is larger than PHENIX. Since the kinematics in STAR probes slightly different kinematic regions compared to PHENIX, there is no enhancement observed for the resulting I_{AA} for trigger photon $12 < p_T^\gamma < 20$ GeV/c. However the overall trend agrees well with the CoLBT model prediction, completing the energy loss picture due to jet-medium interaction at RHIC energies.

STAR has also measured jet-hadron correlations. Compared to dihadron correlations, using jets as triggers sample more closely the energy of the parent parton. A jet trigger is not as good as a photon trigger though in that sense. The upper panel in Fig. 6.1 shows the width of the away-side peak for jets of transverse momentum of 10-15 GeV/c and 20-40 GeV/c in 0-20% central Au+Au collisions at $\sqrt{s_{NN}} = 200$ GeV, compared to p+p points in open squares. The lower panel shows the difference in per-trigger yield between Au+Au and p+p: $D_{AA} = Y_{Au+Au}(p_T^{assoc}) - Y_{p+p}(p_T^{assoc})$. Both the Gaussian width and D_{AA} are plotted as a function of p_T^{assoc} . The Au+Au width shows consistency within uncertainties compared to that of p+p. The D_{AA} shows an enhancement below p_T^{assoc} about 2 GeV/c for jets in the two different selected energy ranges. This finding suggests that the production of extra soft particles is not dependent on the jet energy but the energy of the jet constituents, in agreement with the $\gamma_{dir} - h$ results.

As discussed in section 1.6, jet fragmentation function measurement from CMS experiment has shown that for jets larger than 100 GeV/c, there is also a similar trend of enhancement to suppression for fragmentation function ratio of Pb+Pb to p+p, as the charged particle transverse momentum gets larger. Fig. 1.21 has shown the FF ratio as a function of ξ . The same measurement has also been carried out as a function of associated track momentum p_T^{track} . As reported in Ref.[101], the enhancement is observed in the region of $p_T < 3$ GeV/c, for all jet p_T ranges analyzed ($100 < p_T^{jet} < 300$ GeV/c). Further precision measurement and investigation would be ideal to study and pinpoint the enhancement onsets along p_T^{assoc} for different jet energies at RHIC. This would help quantify possible differences in energy loss mechanism or how the jet and medium interact, when compared to the LHC scenario.

6.3 Future Prospects

Although the PHENIX experiment has taken the last year of data and finished operating in 2016, new experimental effort on improving the capabilities of jet measurement is still ongoing. A new collaboration sPHENIX has formed and the size is actively growing. Designed to have excellent momentum resolution and track pattern recognition, this new experiment is capable of measuring jet fragmentation functions as well as jet substructure with extended kinematic reach and high resolution. The MAPS detector that is

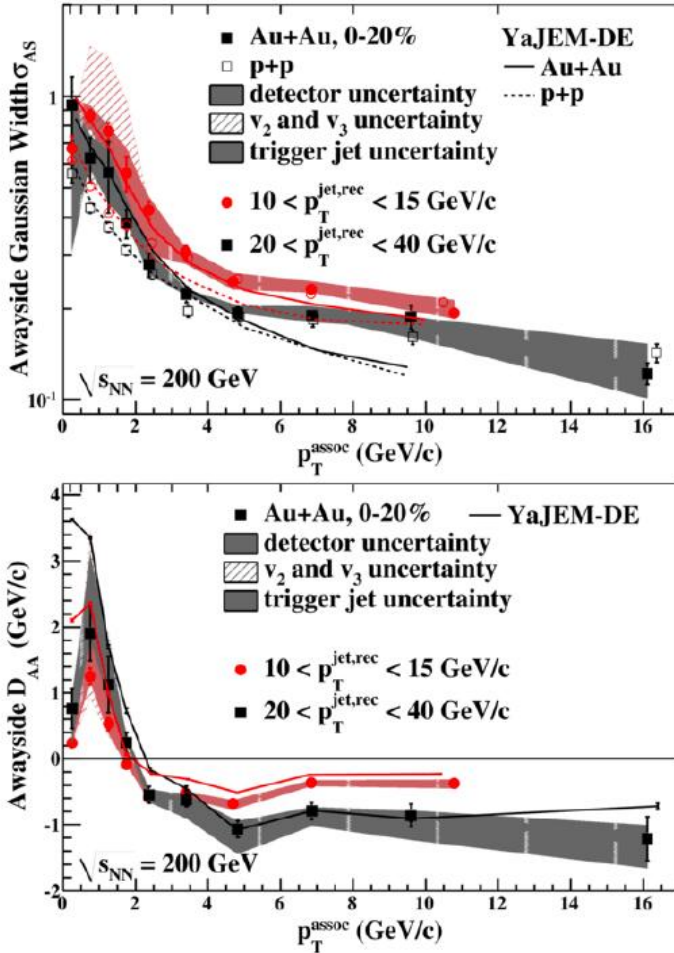


Figure 6.1: Gaussian widths and D_{AA} of the away-side peaks and momentum difference between Au+Au and p+p.

based on ALICE ITS upgrade, together with the INTT detector, will contain layers of silicon sensors. A TPC of radius 20-78 cm has a designed effective hit resolution of $250 \mu\text{s}$. The combination of these three detectors function as a tracking system, rejecting pile-ups and providing excellent high momentum resolution. Calorimetry is crucial in measuring photons, π^0 s, hadrons and reconstructing jets. The combined EMCAL and HCal system in sPHENIX can

achieve good single particle resolution. The strong capability of sPHENIX to carry out photon and jet measurements provides great opportunity to study jet-substructure in a more sophisticated and precise way.

On the theory side, there has been recent effort in collaborating among different theory groups and their models in understanding in-medium jet energy loss. The Jet Energy-loss Tomography with a Statistically and Computationally Advanced Program Envelope (JETSCAPE) collaboration has been formed, with the goal to develop the state of art theoretical model of jet energy loss by applying different models at different stages of jet evolution, as well as a statistical tool for extracting crucial physical parameters such as \hat{q} and α_s from model to data comparison. A user-friendly Monte-Carlo event generator combining these two aspects are being developed for the heavy ion community [25].

Bibliography

- [1] C. Patrignani et al. Rev. of Particle Phys. Chin. Phys. C, Vol. 40, No. 10 (2016) 100001
- [2] F Wilczek. Asymptotic freedom: From paradox to paradigm. Proceedings of the National Academy of Sciences, Jan 2005
- [3] J. D. Bjorken, Energy Loss of Energetic Partons in Quark - Gluon Plasma: Possible Extinction of High p(t) Jets in Hadron - Hadron Collisions. FERMILAB-PUB-82-059-THY.
- [4] M. Gyulassy and M. Plumer, Jet Quenching in Dense Matter, Phys.Lett. B243, 432-438, (1990). doi: 10.1016/0370-2693(90)91409-5.
- [5] X.-N. Wang and M. Gyulassy, Gluon shadowing and jet quenching in A + A collisions at $\sqrt{s} = 200$ GeV, Phys.Rev.Lett. 68, 1480-1483, (1992). doi: 10.1103/PhysRevLett.68.1480.
- [6] G.-Y. Qin, X.-N. Wang, Jet quenching in high-energy heavy-ion collisions, arXiv:1511.00790 (2015)
- [7] K. Adcox et al., Suppression of hadrons with large transverse momentum in central Au + Au collisions at $\sqrt{s_{NN}} = 130$ GeV, Phys. Rev. Lett. 88, 022301, (2002). doi: 10.1103/PhysRevLett.88.022301.
- [8] C. Adler et al., Centrality dependence of high p(T) hadron suppression in Au + Au collisions at $\sqrt{s_{NN}} = 130$ GeV, Phys. Rev. Lett. 89, 202301, (2002). doi: 10.1103/PhysRevLett.89.202301.
- [9] K. Aamodt et al., Suppression of Charged Particle Production at Large Transverse Momentum in Central Pb-Pb Collisions at $\sqrt{s_{NN}} = 2.76$ TeV, Phys.Lett. B696, 30-39, (2011). doi: 10.1016/j.physletb.2010.12.020.

- [10] C. Adler et al., Disappearance of back-to-back high p_T hadron correlations in central Au+Au collisions at $\sqrt{s_{NN}} = 200$ GeV, Phys.Rev.Lett. 90, 082302, (2003). doi: 10.1103/PhysRevLett.90.082302.
- [11] J. Adams et al., Direct observation of dijets in central Au+Au collisions at $\sqrt{s_{NN}} = 200$ GeV, Phys.Rev.Lett. 97, 162301, (2006). doi: 10.1103/PhysRevLett.97.162301.
- [12] B. Abelev et al., Studying Parton Energy Loss in Heavy-Ion Collisions via Direct-Photon and Charged-Particle Azimuthal Correlations, Phys.Rev. C82, 034909, (2010). doi: 10.1103/PhysRevC.82.034909.
- [13] R. Abir, U. Jamil, M. G. Mustafa, and D. K. Srivastava, Heavy quark energy loss and D-Mesons at RHIC and LHC energies, Phys.Lett. B715, 183-189, (2012). doi: 10.1016/j.physletb.2012.07.044.
- [14] G. Aad et al., Observation of a Centrality-Dependent Dijet Asymmetry in Lead-Lead Collisions at $\text{sqrt}(S(\text{NN})) = 2.76$ TeV with the ATLAS Detector at the LHC, Phys.Rev.Lett. 105, 252303, (2010). doi: 10.1103/PhysRevLett.105.252303.
- [15] M. Gyulassy and X. N. Wang, Multiple collisions and induced gluon bremsstrahlung in QCD, Nucl. Phys. B 420, 583 (1994)
- [16] R. Baier, Y. L. Dokshitzer, S. Peigne and D. Schiff, Induced Gluon Radiation in a QCD Medium, Phys. Lett. B 345, 277 (1995)
- [17] H. Li, F. Liu, G.-L. Ma, X.-N. Wang, and Y. Zhu, Mach cone induced by γ -triggered jets in high-energy heavy-ion collisions, Phys. Rev. Lett. 106, 012301 (2011), 1006.2893.
- [18] X.-N. Wang and Y. Zhu, Medium Modification of γ Jets in High-Energy Heavy-Ion Collisions, Phys. Rev. Lett. 111, 062301 (2013), 1302.5874.
- [19] Yayun He, Tan Luo, Xin-Nian Wang, Yan Zhu, Linear Boltzmann Transport for Jet Propagation in the Quark-Gluon Plasma: Elastic Processes and Medium Recoil, Phys.Rev. C91 (2015) 054908
- [20] S. Cao, T. Luo, G.-Y. Qin, and X.-N. Wang, Heavy and light flavor jet quenching at RHIC and LHC energies, Phys. Rev. C94, 014909 (2016), arXiv: 1605.06447.

- [21] S. Cao, T. Luo, G.-Y. Qin, and X.-N. Wang, Multistage Monte-Carlo simulation of jet modification in a static medium (2017), arXiv: 1703.00822.
- [22] W. Chen, S. Cao, T. Luo, L.-G Pang, X.-N. Wang, Evidence of jet-induced medium excitation in γ -hadron correlation in A+A collisions, arXiv: 1704.03648
- [23] X. F. Guo and X. -N. Wang, Multiple Scattering, Parton Energy Loss and Modified Fragmentation Functions in Deeply Inelastic eA Scattering, Phys. Rev. Lett. 85, 3591 (2000).
- [24] X. -N. Wang and X. -F. Guo, Multiple Parton Scattering in Nuclei: Parton Energy Loss, Nucl. Phys. A 696, 788 (2001).
- [25] S. Cao et al., Multistage Monte-Carlo simulation of jet modification in a static medium. arXiv: 1705.00050 (2017)
- [26] The CMS Collaboration, Modification of jet shapes in PbPb collisions at $\sqrt{s_{NN}} = 2.76$ TeV. Phys. Lett. B 730 (2014) 243
- [27] S. Acharya et al. First measurement of jet mass in PbPb and pPb collisions at the LHC arXiv:1702.00804 (2017)
- [28] The CMS Collaboration, Splitting function in pp and PbPb collisions at $\sqrt{s_{NN}} = 5.02$ TeV, (2016), cMS-PAS-HIN-16-006.
- [29] S. D. Ellis, C. K. Vermilion, and J. R. Walsh, Recombination Algorithms and Jet Substructure: Pruning as a Tool for Heavy Particle Searches, Phys.Rev.D 81 (2010) 094023, doi:10.1103/PhysRevD.81.094023, arXiv:0912.0033.
- [30] J. M. Butterworth, A. R. Davison, M. Rubin, and G. P. Salam, Jet substructure as a new Higgs search channel at the LHC, Phys.Rev.Lett. 100 (2008) 242001, doi:10.1103/PhysRevLett.100.242001, arXiv:0802.2470.
- [31] D. Krohn, J. Thaler, and L.-T. Wang, Jet Trimming, JHEP 02 (2010) 084, doi:10.1007/JHEP02(2010)084, arXiv:0912.1342
- [32] M. Dasgupta, A. Fregoso, S. Marzani, and G. P. Salam, Towards an understanding of jet substructure, JHEP 09 (2013) 029, doi:10.1007/JHEP09(2013)029, arXiv:1307.0007.

- [33] A. J. Larkoski, S. Marzani, G. Soyez, and J. Thaler, Soft Drop, JHEP 05 (2014) 146, doi:10.1007/JHEP05(2014)146, arXiv:1402.2657
- [34] K. K. for the STAR collaboration, Star measurements of the shared momentum fraction zg using jet reconstruction in p+p and Au+Au, (2017)
- [35] Y. Aoki, G. Endrodi, Z. Fodor, S. D. Katz, and K. K. Szabo. The Order of the quantum chromodynamics transition predicted by the standard model of particle physics. Nature, 443:675678, 2006.
- [36] A. Bazavov et al. Equation of state in (2+1)-flavor QCD. Phys. Rev. D, 90(9):094503, 2014.
- [37] A. Bazavov et al. The chiral and deconfinement aspects of the QCD transition. Phys. Rev., D85:054503, 2012.
- [38] K. Adcox et al. Formation of dense partonic matter in relativistic nucleus-nucleus collisions at RHIC: Experimental evaluation by the PHENIX Collaboration. Nucl. Phys. A, 757:184, 2005.
- [39] J. Adams et al. Experimental and theoretical challenges in the search for the quark gluon plasma: The STAR Collaborations critical assessment of the evidence from RHIC collisions. Nucl. Phys. A, 757:102, 2005.
- [40] B. B. Back et al. The PHOBOS perspective on discoveries at RHIC. Nucl. Phys., A757:28101, 2005.
- [41] I. Arsene et al. Quark gluon plasma and color glass condensate at RHIC? The Perspective from the BRAHMS experiment. Nucl. Phys., A757:127, 2005.
- [42] ALICE Collaboration, Direct photon production in Pb-Pb collisions at $\sqrt{s_{NN}} = 2.76$ TeV, Phys. Lett. B 754 (2016) 235-248
- [43] H Hahn, E Forsyth, H Foelsche, M Harrison, J Kewisch, G Parzen, S Peggs, E Raka, A Ruggiero, and A Stevens. The RHIC design overview. Nuclear Inst. and Methods in Physics Research, A, 499(2-3):245-263 (2003)
- [44] S. Ozaki and T. Roser. Relativistic Heavy Ion Collider, its construction and upgrade. PTEP, 2015(3):03A102 (2015)

- [45] http://www.phenix.bnl.gov/phenix/project_info/integration/coordinate-system/coord2.gif
- [46] S.S. Adler et al., PHENIX on-line and off-line computing, NIM A499 593-602 (2003)
- [47] S.S. Adler et al., PHENIX on-line systems, NIM A499 560-592 (2003)
- [48] K. Adcox et al., PHENIX detector overview, NIM A499 469-479 (2003)
- [49] L. Aphecetche et al., The PHENIX calorimeter, NIM A499 521-536 (2003)
- [50] C. Fabjan, F. Gianotti, Calorimetry for Particle Physics (2003)
- [51] G. David et al., IEEE Trans. Nucl. Sci. 47 (2000) 1982
- [52] K. Adcox et al., PHENIX central arm tracking detectors, NIM A499 489-507 (2003)
- [53] G. David, et al. IEEE Nuc. Sci. 47, No.6 (2000)
- [54] M. Allen et al., PHENIX inner detectors, NIM A499 549-559 (2003)
- [55] C. Adler et al., The RHIC zero degree calorimeter, Nucl. Instr. and Meth. A470 488 (2001)
- [56] M. Aizawa et al., PHENIX central arm particle I.D. detectors, NIM A499 508-520 (2003)
- [57] B. Ratcliff, J. Schwiening, Handbook of Particle Detection and Imaging, pp 453-471
- [58] R. J. Glauber and G. Matthiae, High-energy scattering of protons by nuclei, Nucl. Phys. B21, 135 (1970)
- [59] M. L. Miller, K. Reygers, S. J. Sanders, and P. Steinberg. Glauber modeling in high energy nuclear collisions. Ann. Rev. Nucl. Part. Sci., 57:205 (2007)
- [60] C-Y. Wong, Introduction to High-energy Heavy-ion Collisions (1994)
- [61] M. Allen, et al., Nucl. Instrum. Meth. A499, 549 (2003)

- [62] S. Milov, Centrality determination using BBC in Au + Au and Cu + Cu collisions at $\sqrt{s_{NN}} = 200$ GeV, PHENIX Internal Document AN461 (2005).
- [63] K. Adcox et al., PHENIX central arm tracking detectors, NIM A499 489-507 (2003)
- [64] K Adcox, J Ajitanand, J Alexander, J Barrette, R Belkin, D Borland, WL Bryan, R Du Rietz, K El Chenawi, and A Cherlin. Construction and performance of the phenix pad chambers. Nuclear Inst. and Methods in Physics Research, A, 497(2-3):263-293 (2003).
- [65] A. Chikanian, B. Kumar, N. Smirnov, and E. O'Brien. A momentum reconstruction algorithm for the phenix spectrometer at brookhaven. Nucl Instrum Meth A, 371(3):480488, Jan (1996)
- [66] J. Mitchell, et al. Event reconstruction in the phenix central arm spectrometers. Nuclear Inst. and Methods in Physics Research, A, 482(1-2):491512, (2002)
- [67] M. Baker et al. Proposal for a Silicon Vertex Tracker (VTX) for the PHENIX Experiment. BNL internal report 72204
- [68] X. Wang, M. Gyulassy, hijing: A Monte Carlo model for multiple jet production in pp, pA, and AA collisions, Phys. ReV. D 44, 3501 (1991)
- [69] A. Sickles, M. McCumber, A. Adare, Extraction of Correlated Jet Pair Signals in Relativistic Heavy Ion Collisions, arXiV:0907.4113 (2009)
- [70] K. C. Zapp, JEWEL 2.0.0: directions for use, Eur.Phys.J. C74 (2014) 2762
- [71] R. Kunnawalkam Elayavalli and K. C. Zapp, Simulating V+jet processes in heavy ion collisions with JEWEL, Eur. Phys. J. C76, 695 (2016)
- [72] K. Zapp, F. Krauss, U. Wiedemann, A perturbative framework for jet quenching, arXiv:1212.1599 (2012)
- [73] R. Elayavalli, K. Zapp, Medium response in JEWEL and its impact on jet shape observables in heavy ion collisions, arXiv:1707.01539 (2017)

- [74] A. Adare et al., Medium modification of jet fragmentation in Au+Au collisions at $\sqrt{s_{NN}} = 200$ GeV measured in direct photon-hadron correlations, Phys. Rev. Lett. 111, 032301 (2013)
- [75] A. Adare, et al., Photon-Hadron Jet Correlations in p+p and Au+Au Collisions at $\sqrt{s_{NN}} = 200$ GeV, Phys.Rev.C80:024908 (2009)
- [76] A. Adare et al., High p_T Direct Photon and pi0 Triggered Azimuthal Jet Correlations in $\sqrt{s_{NN}} = 200$ GeV p+p Collisions, Phys. Rev. D 82, 072001 (2010)
- [77] S. Afanasiev et al., Measurement of Direct Photons in Au+Au Collisions at $\sqrt{s_{NN}} = 200$ GeV, Phys.Rev.Lett. 109 (2012) 152302
- [78] A. Adare et al., Suppression pattern of neutral pions at high transverse momentum in Au+Au collisions at $\sqrt{s_{NN}} = 200$ GeV and constraints on medium transport coefficients, Phys. Rev. Lett. 101, 232301 (2008)
- [79] A. Adare, Transverse momentum evolution of neutral pion triggered di-hadron correlations in Au+Au collisions at $\sqrt{s_{NN}} = 200$ GeV, University of Colorado Ph.D. Dissertation (2009)
- [80] M. Connors, Direct Photon Tagged Jets in 200 GeV Au+Au Collisions at PHENIX, Stony Brook University Ph.D. Dissertation (2011)
- [81] H. Asano, Nuclear modification of electron yields from charm and bottom hadrons in Au+Au collisions at $\sqrt{s_{NN}} = 200$ GeV, Kyoto University Ph.D. Dissertation (2015)
- [82] M. McCumber, Measurements of Fast Parton Interactions with Hot Dense Nuclear Matter via Two Particle Correlations at PHENIX, Stony Brook University Ph.D. Dissertation (2010).
- [83] M. Nguyen, Two Particle Correlations with Direct Photon and π^0 Triggers in 200 GeV p+p and Au+Au Collisions, Stony Brook University Ph.D. Dissertation (2009)
- [84] J. A. Hanks, Properties of Fragmentation Photons in p+p Collisions at 200 GeV Center-of-Mass Energies, Columbia University Ph.D. Dissertation (2010)

- [85] A Milov. Charged particle multiplicity measurement in au-*au* collisions using the pad chambers of the phenix detector at rhic, Weizmann Institute of Science Ph.D. Dissertation (2002)
- [86] J. Frantz, M. Nguyen, J. Chen, M. Connors, Final Analysis of the Run 4 Au+Au and Run 5+6 p+p Direct Photon-Hadron Correlations (PPG090), PHENIX Analysis Note 718 (2009)
- [87] J. Jia, B. Cole, Mathematical framework on correlation function and conditional yield in d+Au and p+p, PHENIX Analysis Note 313 (2004)
- [88] A. Adare, et al., Dihadron azimuthal correlations in Au+Au collisions at $\sqrt{s_{NN}} = 200$ GeV, Phys. Rev. C 78, 014901 (2008)
- [89] K. Reygers, Glauber Monte-Carlo Calculations for Au+Au Collisions at $\sqrt{s_{NN}} = 200$ GeV, PHENIX Analysis Note 169 (2003)
- [90] H. Ge, J. Mitchell, EMCAL Calibration for the Run 12 Combined Heavy Ion Datasets, PHENIX Analysis Note 1088 (2013)
- [91] S. Yalcin, A. Hanks, H. Ge, B. Jacak, Recalibration of PC3/EMC Track Matching Variables for Run11 Au + Au Collisions at 200 GeV, PHENIX Analysis Note 1203 (2014)
- [92] C-H. Chen, M. Connors, J. Frantz, A. Hanks, M. Nguyen, M. Tannenbaum, Analysis of Run 10 Au+Au Direct Photon-Hadron correlations and combined Run 7 + Run 10 results for ppg113, PHENIX Analysis Note 1045 (2012)
- [93] A. Adare, et al., Spectra and ratios of identified particles in Au+Au and d+Au collisions at $\sqrt{s_{NN}} = 200$ GeV, Phys. Rev. C 88, 024906 (2013)
- [94] J. R. Taylor, An Introduction to Error Analysis: The Study of Uncertainties in Physical Measurements.
- [95] T. Sakaguchi, R. Vertesi, Measurement of direct photon spectra with PbSc EMCAL in $\sqrt{s_{NN}} = 200$ GeV Au+Au Collisions at Run4, G. David, H. Hamagaki, J. Imrek, T. Isobe, B. Sahlmueller, PHENIX Analysis Note 490 (2006)
- [96] W. Braunschweig et al. (TASSO Collaboration), Z. Phys. C47, 187 (1990).

- [97] T. Renk, Phys. Rev. C 84, 067902 (2011)
- [98] Borghini and Wiedemann, Distorting the Hump-backed Plateau of Jets with Dense QCD Matter, arXiv: hep-ph/0506218 (2005)
- [99] H. Ge, PHENIX Analysis Note 1272, A. Hanks, B. Jacak, Direct photon-hadron correlations in Run-11 Au+Au 200 GeV and combined results with Run7 + Run10 + Run11 for preliminary (2016)
- [100] A. Hanks, PHENIX Analysis Note 1271, Analysis of Run 8 d + Au Direct Photon-Hadron correlations (2016)
- [101] The CMS Collaboration, Measurement of jet fragmentation in PbPb and pp collisions at $\sqrt{s_{NN}} = 2.76$ TeV, Phys. Rev. C 90 (2014) 024908
- [102] G. Aad et al., Measurement of inclusive jet charged-particle fragmentation functions in Pb+Pb collisions at $\sqrt{s_{NN}} = 2.76$ TeV with the ATLAS detector. Phys.Lett. B739, 320 (2014)